KU LEUVEN

FACULTY OF SCIENCE

# Development of genetically encoded sensors for monoamines in *C. elegans*

**Su Min CHO**

Supervisor: Prof. Dr. W. Schafer
Animal Physiology and Neurobiology

Co-supervisor: Prof. Dr. I. Beets
Animal Physiology and Neurobiology

Mentor: Dr. J. Watteyne
Animal Physiology and Neurobiology

Thesis presented in
fulfillment of the requirements
for the degree of Master of Science
in Biophysics, Biochemistry and Biotechnology

Academic year 2020-2021

# Host lab information page

Master theses performed in the Beets/Schafer lab comply with following house rules:

1. *Maximal education and scientific self-empowerment of students*

   Students are encouraged to learn from their mistakes through dialogue, rather than by simply being corrected by their supervisors. All writing in this document is the result of this process.

   Students get two feedback moments with respect to their writing process. One from their daily supervisor, who will advise them on format and content (*e.g.* scientific language, proper representation of results and structure of their interpretations). For this, daily supervisors interact either in person with the student, or via comments added to the manuscript. A second feedback session includes comments from (co)supervisors and only focuses on content. This implicates additional input with regards to the student's findings and the final discussion of results. The student's interpretation of this feedback is integrated in the final version of this manuscript, as it is presented here.

2. *Authenticity in science*

   Potential plagiarism was verified using TurnItIn. This work overall scored 13% of potential plagiarism. Sections underlying this result were manually verified by the daily supervisor, as such supporting the authenticity of this work.

# Preface

I still remember myself on the first day walking into the lab, excited and nervous at the same time. Yet, two semesters have flown by and here I am about to cross the finishing line for my master program. This research project has been truly a great learning experience for me, where I could practice what I learned in the class and gain much more technical expertise in a living scientific research environment.

I would like to thank my promoters, Prof. Isabel Beets and Prof. William Schafer for offering this valuable opportunity to work in their lab. Their genuine interest in the topic and timely advices have been a core drive for this project.

My special thanks go to my daily mentor Dr. Jan Watteyne whose passion and strong belief in science have inspire me throughout the project. Without his kind guidance and skillful know-hows, I would not have been able to complete this project.

Also, I send sincere thanks to mentor Dr. Amy Courtney for the warm encouragement and support from afar. Due to pandemic situation, I have not been able to work with her in person, but I look forward to it in the near future.

Finally, I extend my thanks to all the members of *C. elegans* lab, who did not hesitate to give me a hand when I was lost and struggling in the lab. Also, I thank my family, who has got my back wherever I am, whatever I do, and Attila Budavári for unconditional love and support through all my ups and downs.

# Summary

Biogenic amines are signaling molecules that serve a wide array of functions in the nervous system. They can signal through both ionotropic and metabotropic receptors, thereby acting as neuromodulator and neurotransmitters. Yet, our understanding of their precise actions in neuronal circuits is limited. As the monoaminergic signaling system is ancient and highly conserved over species, findings in model organisms are likely to translate to more numerically complex organisms.

*C. elegans* is a widely used model organism that is exquisitely suited to study monoamine signaling owing to its well-defined nervous system of which the entire physical connectivity has been reconstructed. In addition, a rough draft of all putative monoaminergic connections is available, offering an unprecedent opportunity to unravel the complex nature of monoaminergic neurotransmission. *C. elegans* produces several monoamines including dopamine, serotonin, melatonin, octopamine and tyramine. While the biological functions of octopamine and tyramine have yet to be extensively characterized in vertebrates, they are known to govern various functions of *C. elegans* physiology and behavior, including locomotion, memory, innate immunity and decision-making.

Commonly used approaches to quantify monoaminergic neurotransmission are either indirect or lack the spatial and temporal resolution to investigate these signaling events at a cellular level. In order to overcome these limitations, various types of fluorescent biosensors have been developed recently for the visualization of monoaminergic signaling *in vivo*. One exciting class of sensors are those that allow real-time monitoring of GPCR activation. Briefly, these sensors are engineered endogenous GPCRs of which the third intracellular domain is replaced by a circularly permuted fluorescent protein. Conformational changes of the GPCR scaffold upon binding of the receptor's ligand are transduced to the fluorescent protein and alter its fluorescence emission intensity, thus providing a reliable and reversible method for visualizing monoaminergic signaling. This methodology has been used to study dopamine, serotonin, acetylcholine and norepinephrine signaling. However, it has yet to be applied to investigate the dynamics of octopamine and tyramine transmission.

This Master's thesis set out to engineer and implement real-time sensors to investigate octopaminergic and tyraminergic signaling in *C. elegans*. First, the third intracellular domain of the endogenous OCTR-1 octopamine and TYRA-2a tyramine receptor was predicted by sequence homology. Next, this intracellular region was replaced by inserting a red circularly permuted

fluorescent protein, cpmApple, into the GPCRs using Gibson assembly. In addition, a small library of 6 different linker regions previously optimized in other sensors was used to connect the red fluorescent protein to the receptor, as linkers are known to be crucial in determining proper folding and reporting performance of the biosensor. While these 6 variants of the OCTR-1 octopamine sensor were successfully constructed, recurring cloning issues prevented 6 TYRA-2a sensor variants to be generated.

Next, the performance of the OCTR-1 sensor variants was investigated in mammalian cells. First, sensor constructs were subcloned into a pcDNA3.1 expression vector using directional TOPO cloning. 4 out of 6 OCTR-1 sensor variants were successfully cloned, after which they were used to transfect mammalian HEK293 cells. Transfected cells showed basal red fluorescence for all 4 variants, indicating proper folding of red fluorescent indicator. However, no strong fluorescent changes were observed upon exogenous application of octopamine. Additional imaging experiments are required to confirm proper membrane localization of the sensors. In addition, an alternative instrumental set-up, including the use of a perfusion system and specialized cell culture plates, is needed to characterize the performance of OCTR-1 sensor variants in relaying octopaminergic signaling events.

Taken together, a lack of modularity of real-time GPCR sensors requires large-scale optimization processes, which is a challenge for the development of new sensors. Still, this type of sensor remains a powerful tool to visualize monoaminergic neurotransmission at an incomparable spatiotemporal resolution. Future work guided by the results of this project will facilitate the development of OCTR-1 octopaminergic and TYRA-2a tyraminergic sensors. Ultimately, this will provide a powerful new tool to investigate monoaminergic signaling in *C. elegans*, which promises to advance our understanding of how monoamines signal within the nervous system.

# List of abbreviation

| | |
|---|---|
| **5-HT** | 5-hydroxytryptamine |
| **5HT2A** | 5-HT2A receptor |
| **A2AR** | alpha-2 adrenergic receptor |
| **AADC** | aromatic-L-amino acid decarboxylase |
| **ADB** | agarose dissolving buffer |
| **B1AR** | beta-1 adrenergic receptor |
| **B2AR** | beta-2 adrenergic receptor |
| ***C. elegans*** | *Caenorhabditis elegans* |
| **cDNA** | complementary deoxyribonucleic acid |
| **CNiFER** | cell-based neurotransmitter fluorescent engineered reporters |
| **CO** | Clustal Omega |
| **cpFP** | circularly permuted fluorescent protein |
| **CTCF** | corrected total cellular fluorescence |
| **DA** | dopamine |
| **DAG** | diacylglycerol |
| **dATP** | deoxyadenosine triphosphate |
| **DMEM** | Dulbecco's Modified Eagle Medium |
| **DNA** | deoxyribonucleic acid |
| **DRD** | dopamine receptor |
| ***E. coli*** | *Escherichia coli* |
| **EGFP** | enhanced green fluorescent protein |
| **ER** | endoplasmic reticulum |
| **FLIPR** | Fluorescent Imaging Plate Reader |
| **FP** | fluorescent protein |
| **FRET** | Förster resonance energy transfer |
| **FSCV** | fast-scan cyclic voltammetry |
| **GECI** | genetically encoded calcium indicator |
| **GFP** | green fluorescent protein |
| **GPCR** | G protein-coupled receptor |
| **HBSS** | Hanks' Balanced Salt Solution |
| **HEK293** | human embryonic kidney 293 cells |
| **ICL3** | intracellular loop 3 |
| **$IP_3$** | Inositol 1,4,5-trisphosphate |
| **KOR** | kappa-type opioid receptor |
| **LB** | lysogeny broth |
| **LDCV** | large dense-core vesicle |

| | |
|---|---|
| **LGC** | ligand-gated ion channel |
| **LGCG** | large dense core granule |
| **LOV** | light-oxygen-voltage-sensing domain |
| **LPS** | lipopolysaccharide |
| **MAOI** | monoamine oxidase inhibitor |
| **MAT** | monoamine transporter |
| **MCS** | multiple cloning site |
| **MD** | molecular dynamics |
| **MOR** | μ-opioid receptor |
| **MT2** | melatonin receptor 1B |
| **NADPH** | nicotinamide adenine dinucleotide phosphate |
| **NE** | norepinephrine |
| **NMR** | nuclear magnetic resonance spectroscopy |
| **NpHR** | Halorhodopsin |
| **OA** | octopamine |
| ***P. aeruginosa*** | *Pseudomonas aeruginosa* |
| **PCA** | protein-fragment complementation assay |
| **PCR** | polymerase chain reaction |
| **PEA** | phenethylamine |
| **PLC-β** | phospholipase C β |
| **PPI** | protein-protein interaction |
| **ROI** | region of interest |
| **SERT** | serotonin transporter |
| **SOC** | super optimal broth with catabolites |
| **SPARK** | Specific Protein Association tool giving transcriptional Readout with rapid Kinetics |
| **SR** | sarcoplasmic reticulum |
| **SV** | synaptic vesicle |
| **TAAR** | trace amine-associated receptor |
| **TAE** | tris-acetate-EDTA |
| **TBH-1** | tyramine beta-hydroxylase |
| **TDC-1** | tyramine decarboxylase |
| **TEV** | tobacco etch virus |
| **TM** | transmembrane segment |
| **TMHMM** | transmembrane model based on hidden Markov model |
| **TPH** | tryptophan hydroxylase |
| **UPR** | unfolded protein response |
| **UV** | ultraviolet |
| **VMAT** | vesicular monoamine transporter |

# Table of Contents

# 1. Literature Study

## 1.1. Biogenic amines

### 1.1.1. Classification and biosynthesis of monoamines

Biogenic amines are important signaling molecules in the nervous system that can both serve as neurotransmitters or neuromodulators. They are involved in a wide variety of pivotal brain processes such as learning and memory (Korz and Frey, 2007). Also, dysfunctional monoaminergic transmission has been linked to psychiatric disorders including addiction (Eiden and Weihe, 2011), depression, anxiety disorders (Ressler and Nemeroff, 2000), Parkinson's disease (Catoni *et al*., 2019) and Schizophrenia (Murphy *et al*., 1974; Takano, 2018).

The classical monoamine neurotransmitters are divided into three groups: catecholamines, indolamines and histamines. The group of the catecholamines includes dopamine (DA) and norepinephrine (NE). As adrenergic receptor agonists, norepinephrine and epinephrine induce 'fight-or-flight' behaviors (Goldstein, 2010). The indolamine family includes serotonin (5-hydroxytryptamine; 5-HT) and melatonin, which are known to influence mood and sleep (Ruhé *et al*., 2007; Srinivasan *et al*., 2009). Histamine is an important immune signaling molecule that mediates inflammation responses (Branco *et al*., 2018).

Apart from these well-established classical monoamines, octopamine and tyramine represent another group of endogenous monoamines that has been extensively studied in invertebrates. As these monoamines were first discovered at relatively low physiological concentrations in the mammalian brain, they were initially named 'trace' amines. Later, however, these monoamines were also found to exist at fairly high concentrations in invertebrates, suggesting the initial nomenclature to be misleading (Roeder, 2016). Whereas tyramine (TA), octopamine (OA) and phenethylamine (PEA) are the best characterized 'trace amines', far more types of trace amines have been identified to date (Berry, 2004). Especially, octopamine and tyramine perform important functions in invertebrates, analogous to those of adrenergic signaling by norepinephrine and epinephrine in vertebrates (Sotnikova and Gainetdinov, 2009). Yet, their biological roles are not clearly elucidated in vertebrate models. In humans, research efforts are mostly directed at investigating their interactions with monoamine oxidase inhibitors (MAOIs) due to their pharmacological importance.

Generally, the synthesis of monoamines begins with aromatic amino acid precursors such as phenylalanine, tyrosine or tryptophan (Figure 1a). The biosynthesis process requires specific sets of enzymes for hydroxylation and decarboxylation. Aromatic-L-amino acid decarboxylase (AADC) is an enzyme that catalyzes the decarboxylation of the amino acid precursors into monoamines, which is essential for the synthesis of both classical and trace amines. Dopamine-β-hydroxylase further hydroxylates

tyramine and dopamine to synthesize octopamine and norepinephrine, respectively (Hochman, 2015).

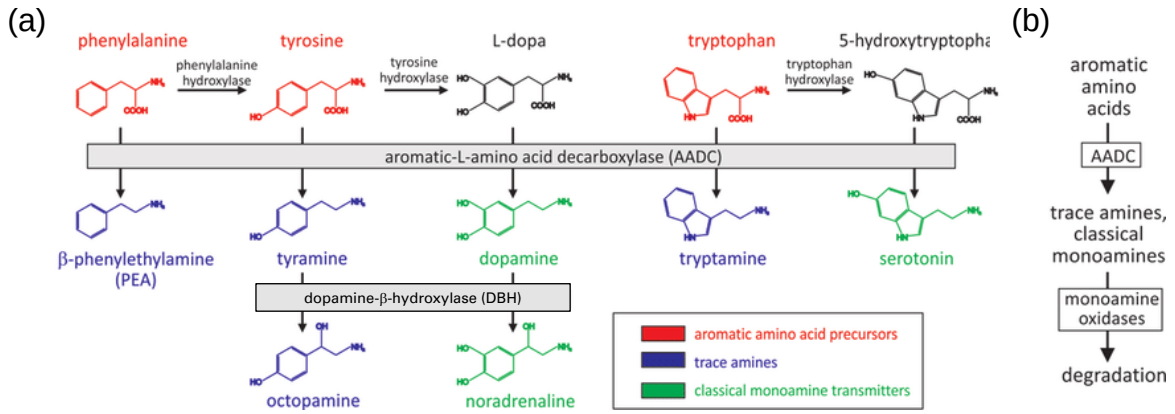


**Figure 1. (a) Biosynthesis pathways of monoamines.** Classical monoamines (green) and trace amines (blue) are synthesized from aromatic amino acid precursors (red), and aromatic-L-amino acid decarboxylase (AADC) is required for this process. **(b) Overview of synthesis and degradation of monoamine.** Monoamine oxidases degrade monoamines. (Hochman, 2015)

### 1.1.2. Monoamine mode of action and degradation

After synthesis, monoamines are packaged in synaptic vesicles (SVs) of presynaptic neurons via vesicular monoamine transporters (VMATs). VMATs use proton gradients generated by V-ATPases as a driving force for monoamine uptake (Duerr *et al*., 1999; Eiden, 2000). In addition to SVs, monoamines can also be stored in large dense core vesicles (LDCVs) and large dense core granules (LGCGs) (Torrealba and Carrasco, 2004). In general, monoamines are released from these vesicles to the extracellular milieu via regulated exocytosis. When a presynaptic neuron is electrically activated, there is a rapid increase in cytoplasmic calcium concentration. The calcium flux triggers a fusion of the monoamine-containing vesicles with the plasma membrane, and this process is mediated by various calcium-dependent proteins (Barclay *et al*., 2005).

Monoamines have a broad range of functions and can act both as neurotransmitter and neuromodulator. They bind specific receptor molecules on target cells, which are either ionotropic or metabotropic receptors. The conventional view is that monoamines primarily act as neurotransmitters when they are released into the synaptic cleft. Acting as neurotransmitter, they elicit fast and site-specific responses through the binding of ligand-gated ion channels (LGCs) on the post-synaptic cell. On the other hand, monoamines can also function as neuromodulator by targeting metabotropic G protein coupled receptor (GPCRs), of which the response is relatively slower but lasts longer in comparison to LGC-mediated signaling. Different monoamines can exert synergistic or antagonistic effects on promiscuous receptors, while conversely, a single monoamine can have varying impacts on several receptors and physiological mechanisms at multiple timescales (Nadim and Bucher, 2014).

After signaling, monoamines can be recycled and taken up again in the presynaptic vesicles by specific sodium-coupled monoamine transporters (MATs) (Torres *et al*., 2003), or they can be degraded by monoamine oxidases (MAOs) (Figure 1b). Monoamine oxidases are mitochondria-bound enzymes that catalyze the deamination of neurotransmitters, thereby regulating monoamine neurotransmitter levels. Monoamine oxidases play a prominent role in pharmacology, as monoamine oxidase inhibitors (MAOIs) have been used to treat various neurological diseases such as depression, Alzheimer's Disease and Parkinson's Disease (di Giovanni *et al*., 2016; Youdim *et al*., 2006). As these inhibitors attenuate the activity of monoamine oxidases, they boost endogenous monoamine signaling by maintaining optimal levels of these signaling molecules.

### 1.1.3. Conservation and diversification of monoaminergic signaling

Monoamines, along with various small molecule transmitters and neuropeptides, are key players in neuromodulation. Phylogenetic studies indicate that many of these signaling systems are evolutionarily ancient and may even have evolved before the emergence of nervous systems (Katz and Lillvis, 2014). The molecular components of aminergic signaling are highly conserved across the Animal Kingdom (Nichols and Nichols, 2008; Yamamoto and Vernier, 2011). For example, the serotonin pathway is present in mammals, other vertebrates and invertebrates and this conserved molecular machinery is well described in the review of Curran and Chalasani. For instance, *C. elegans* and *Drosophila* homologs of the mammalian genes encoding tryptophan hydroxylase (TPH), vesicular monoamine transporter (VMAT), 5-HT receptor, serotonin transporter (SERT), and monoamine oxidase (MAO) have been identified (Curran and Chalasani, 2012).

Monoaminergic GPCRs have evolved through gene duplication, neofunctionalization, and loss (Katz and Lillvis, 2014), but sometimes their origins and relationships remain unclear. For instance, unlike neuropeptide receptors that show considerable conservation of ligand/receptor pairs (Bauknecht and Jékely, 2017; Mirabeau and Joly, 2013), monoamine receptors are rather promiscuous (Yamamoto *et al*., 2013). Strikingly, phylogenetically related clades of monoaminergic receptors vary in terms of agonist and G protein subtype (Figure 2). Specifically, molecular phylogeny shows that dopamine receptor D1 is more closely related to other aminergic receptors than the D2 dopamine receptor (Mustard *et al*., 2005; Spielman *et al*., 2015). It is hypothesized that these two receptors have acquired the affinity toward dopamine in an independent manner after a diverging event (Callier *et al*., 2003).

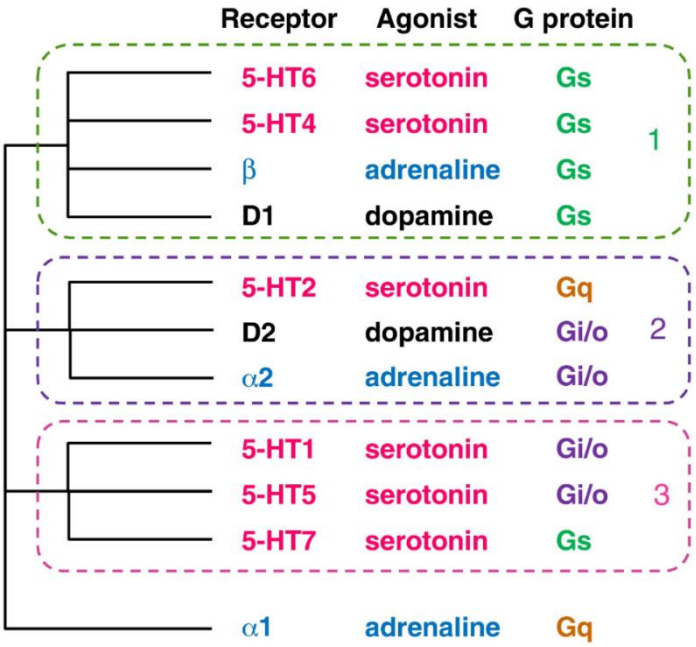


**Figure 2. Phylogenetic analysis of monoamine receptors** (Yamamoto *et al*., 2013)**.** Phylogenetic analysis of dopamine (black), serotonin (red) and adrenaline (blue) receptors show that the clades do not coincide with agonists nor G protein subtypes.

A similar phenomenon can be observed for the trace amine receptors. Biochemical studies demonstrated that octopamine and tyramine GPCRs co-exist with adrenergic receptors in some protostomian invertebrates (Bauknecht and Jékely, 2017). This finding suggests that all three monoamine signaling systems were present in a common ancestor of protostomian and deuterostomian animals, and evolved more than 700 million years ago. From these ancestral families, the octopamine and tyramine receptors seem to have been lost from most deuterostomes, including vertebrates, while in insects and nematodes, the adrenergic receptors appear to have been lost.

Nonetheless, trace amines appear to maintain a signaling function, as a family of receptors was identified in vertebrates that are activated by trace amines (Borowsky *et al*., 2001). Yet, they are distinct in both structure and function from their invertebrate counterparts (Lindemann *et al*., 2005), hence these monoaminergic-related receptors in vertebrates were named 'Trace Amine-Associated Receptors' (TAARs) to avoid confusion (Gainetdinov *et al*., 2018). This large gap in evolutionary distance between trace amine receptors of invertebrates and vertebrates should be taken into consideration in comparative research.

While some differences in the monoaminergic signaling pathways exist, discoveries made in invertebrate models are still of relevance to vertebrate monoaminergic signaling, especially considering the conserved molecular basis underpinning this process. Fundamentally, monoamines modulate neural networks by reconfiguring the intrinsic excitability of ion channels, altering synaptic strength and orchestrating signaling dynamics. This essential property of monoamine signaling remains highly

conserved, yet differences in the compartmentalization of these signaling events (such as differential expression of receptors and release of neuromodulators) played a dominant role in the evolution of behavior (Katz and Lillvis, 2014). Therefore, basic conserved properties of monoaminergic signaling can be studied in less complex invertebrate model organisms such as *C. elegans.*

## 1.2. Monoamine signaling in *C. elegans*

### 1.2.1. The model organism *C. elegans*

*C. elegans* is a small, transparent and free-living nematode. In the wild, it is normally found in compost-like organic-rich environments such as rotting fruit, garden soil and plant stems as these habitats contain bacteria on which the worms feed (Corsi *et al*., 2015). Fully-grown adult worms are about 1mm long and most of them are hermaphrodite (having both male and female genitalia).

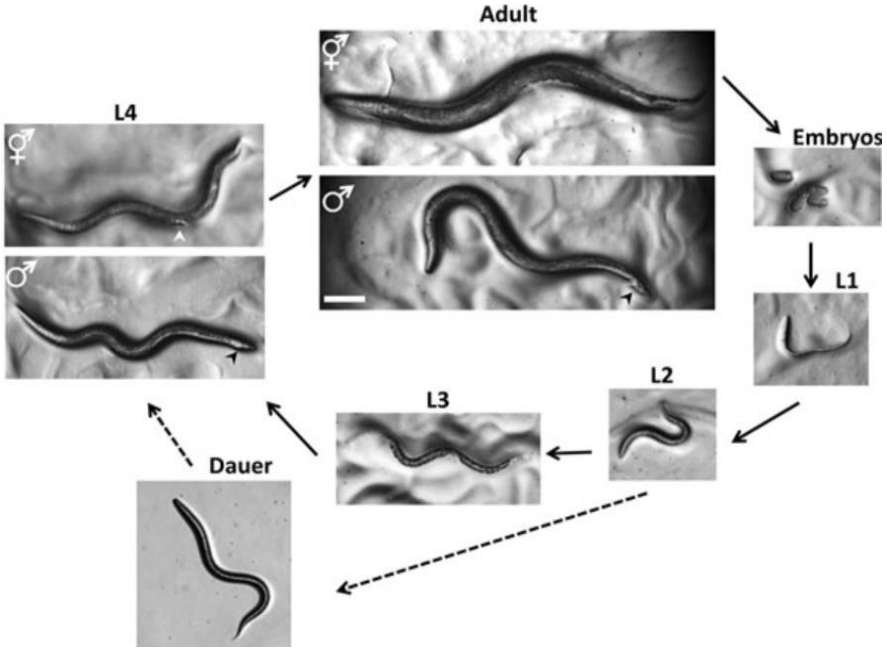


**Figure 3. Life cycle of *C. elegans*** (Corsi *et al*., 2015). *C. elegans* goes through 4 larval stages during the development until it reaches the adult stage. Alternatively, it can go through *dauer* stage under unfavorable conditions. Most of the worms are hermaphrodite and capable of self-reproducing themselves, whereas male worms can only produce progenies by mating hermaphrodites.

During their reproductive period, hermaphrodites are capable of self-fertilizing their oocytes with internally produced and stored sperm. Alternatively, hermaphrodites can also produce progeny after mating with a male, which occur naturally at very low frequencies. Embryos are laid around 24-cell stage, and after hatching, worms go through 4 larval stages (L1, L2, L3 and L4) during their development before reaching the adult stage (Figure 3). *C. elegans* can also undergo an alternative developmental stage under unfavorable conditions, which is referred to as the *dauer* stage. Dauer larvae develop a thick cuticle that offers extra protection from harsh environments, and

they can survive for months until favorable food and living conditions reappear (Corsi *et al*., 2015).

*C. elegans* is widely used as a model organism for neuroscientific research. Main advantages of *C. elegans* are its compact nervous system, the relative ease of genetic manipulation and the worm's well-quantified behavioral repertoire (Corsi *et al*., 2015; Javer *et al*., 2018). Furthermore, the *C. elegans* nervous system has been extensively characterized, and blueprints of its structure and connectivity (known as connectome) are available. Indeed, already back in 1986 Sydney Brenner and his colleagues reconstructed the entire neuronal anatomy and connectivity pattern for the hermaphrodite's 302 neurons using a serial section microscopy approach (White *et al*., 1986), the first – and for a long time only – fully mapped connectome. Later, the connectome of the adult male was drafted (Jarrell *et al*., 2012). Since then, similar serial section microscopy approaches and novel computational algorithms have further shed light on the structure and physical wiring of the *C. elegans* nervous system (Brittin *et al*., 2021; Cook *et al*., 2019; Moyle *et al*., 2021), as well as its variability over individuals and through development (Witvliet *et al*., 2020). Taken together, comprehensive whole-animal connectomes are available for both male and hermaphrodite and *C. elegans* to date (Figure 4).

Despite the small number of *C. elegans* neurons and their well-characterized physical connections, there are still many gaps that have to be filled in order to understand the organization and functioning of neuronal circuits in the *C. elegans* nervous system. As the connectome only defines physical connections, the excitatory or inhibitory nature of each chemical synapse still needs to be experimentally determined. Furthermore, the *C. elegans* nervous system employs a wide spectrum of neuropeptidergic and monoaminergic signaling systems (Chase and Koelle, 2007; Frooninckx *et al*., 2012; Li and Kim, 2008) which typically do not require synapses to signal and therefore can exchange signals between neurons that are not in physical contact. This mode of neuromodulatory signaling therefore adds additional layers of functional connectivity on top of all 302 neurons, and therefore increases the complexity of possible signaling connections (Bentley *et al*., 2016). In other words, a connectome only provides a rough road map for understanding neural interactions, but important information such as the duration and effective range of these interactions is missing (Bargmann, 2012; Bargmann and Marder, 2013). Therefore, further research on neuromodulatory signaling is required for a more accurate understanding of the *C. elegans* nervous system.

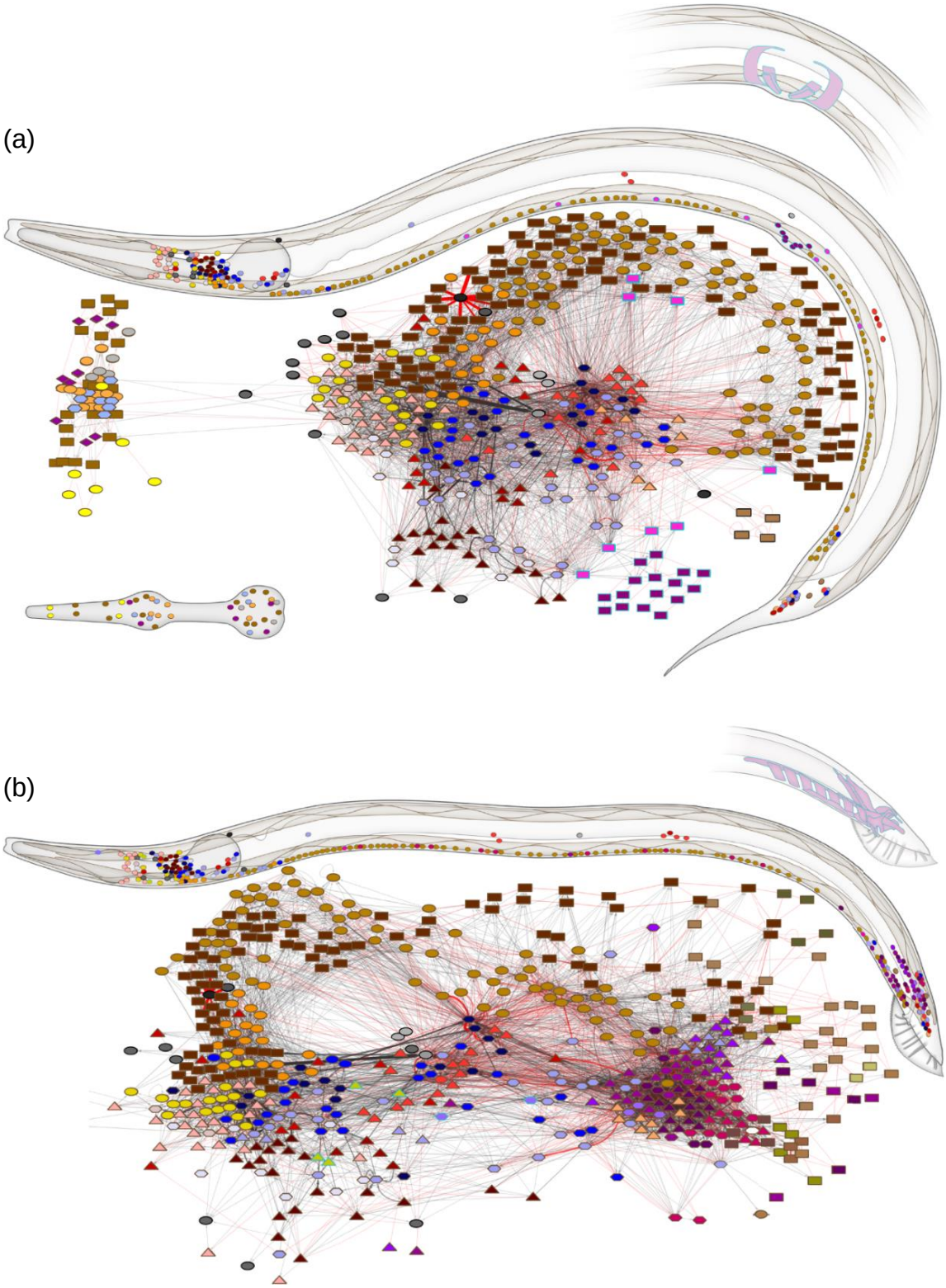


**Figure 4. *C. elegans* connectome of (a) adult hermaphrodites and (b) adult male** (Cook *et al*., 2019). Sensory neurons (triangle), interneurons (hexagon), motor neurons (oval) and muscles (rectangle) are shown in network diagrams. Different colors define modality and similarity of connectivity; sensory neurons (red), interneuron (blue), motor neurons (yellow and orange). Sex-specific neurons are purple or pink and sex muscles are shown separately in the top right corner.

### 1.2.2. Monoamine signaling in *C. elegans*

A variety of monoamines including dopamine, serotonin, melatonin (Chase and Koelle, 2007; Niu *et al*., 2020), octopamine and tyramine are found in *C. elegans*. However, histamine, epinephrine and norepinephrine have not been detected (Chase and Koelle, 2007). Biosynthetic pathways for the main biogenic amines (serotonin, dopamine and octopamine/tyramine) have also been well characterized in *C. elegans* (Figure 5). Monoamines are generated by sequential hydroxylation and decarboxylation of tryptophan and tyrosine amino acid precursors.

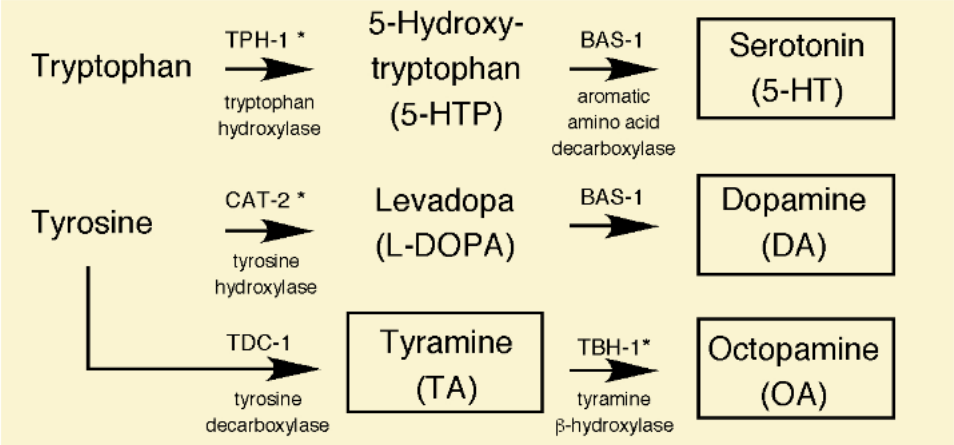


**Figure 5. Biosynthesis of monoamines in *C. elegans*** (Chase and Koelle, 2007).

As the production of monoamines requires a series of biosynthetic enzymes and the *C. elegans* specific transporter *cat-1* (Duerr *et al*., 1999), analyses of the expression patterns of the corresponding genes along with mutant phenotype studies provided important clues for identifying the monoamine expressing neurons in *C. elegans* (Table 1).

**Table 1. A list of putative monoamine synthesizing cells** (Chase and Koelle, 2007).

| **Monoamines** | **Cell type** |
|---|---|
| Dopamine | ADE, PDE, CEP, R5A, R7A, R9A |
| Serotonin | CP1-6, R1, R3, R9, NSM, HSN, VC4, VC5, ADF, RIH, AIM |
| Octopamine | RIC, Gonad sheath |
| Tyramine | RIC, RIM, Gonad sheath, UV1 |

Expression data of these biosynthetic enzymes, in addition to that for monoaminergic receptors, served as the basis for the construction of a draft monoaminergic connectome (Bentley *et al*., 2016). Analogous to the physical synaptic connectome, this network of monoaminergic signaling has been mapped by linking monoamine expressing neurons and corresponding receptor-expressing cells. The resulting

networks indicate that the majority of monoaminergic signaling occurs extrasynaptically rather than between neurons that are connected via synpases or gap junctions, which eludes to the existence of a large wireless component in the *C. elegans* connectome (Bentley *et al*., 2016).

In addition, the topology of the monoamine signaling network follows a star-shaped network structure, where a few monoamine-producing neurons signal to many peripheral neurons across the worm (Bentley *et al*., 2016). This structure is well-suited to efficiently connect many disparate parts of the nervous system, coordinating a broad range of functions from reproduction to feeding and experience-dependent plasticity. Like in mammals, serotonin and dopamine have well-established functions in *C. elegans* feeding behaviors, learning and memory (Ardiel and Rankin, 2010; Kindt *et al*., 2007).

### 1.2.3. Tyramine and octopamine signaling in *C. elegans*

Both tyramine and octopamine are decarboxylase products of tyrosine. In *C. elegans*, the tyrosine decarboxylase (TDC-1) converts tyrosine to tyramine, and tyramine β-hydroxylase (TBH-1) further converts tyramine to octopamine (Alkema *et al*., 2005). Due to this sequential biosynthetic pathway, tyramine used to be considered as a metabolic precursor of octopamine synthesis. However, differential expression of the *tbh-1* gene highlights that tyramine is an independent neurotransmitter, as TBH-1 is indispensable for hydroxylation of tyramine for octopamine synthesis (Alkema *et al*., 2005).

The production of tyramine and octopamine takes place in a small number of *C. elegans* cells as seen in Table 1. Expression analysis of the *tdc-1* gene uncovered the interneuron RIM as signature tyraminergic neurons. In addition, the RIC interneuron, gonad sheath and the neurosecretory uterine cell UV1 are known to produce tyramine as well (Alkema *et al*., 2005). Of note, the RIC interneuron pair and gonad sheath show co-expression of both *tdc-1* and *tbh-1* genes, suggesting that these cells produce and release both octopamine and tyramine (Alkema *et al*., 2005).

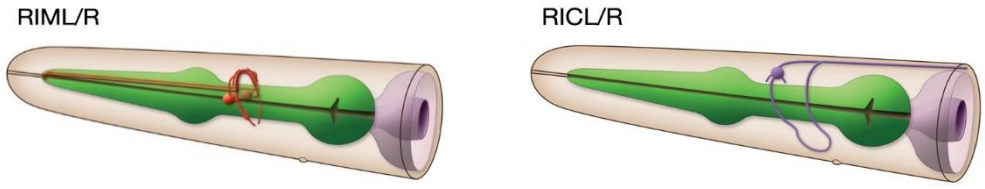


**Figure 6. Tyraminergic ring inter/motor (RIM) neuron and octopaminergic ring interneuron (RIC) (Wormatlas).** Both RIM and RIC neurons are located in the head of *C. elegans.* Especially the RIM neuron innervates muscles in the nerve ring of *C. elegans*. As interneurons, they integrate the external information and the inner state of the animal.

RIC and RIM are interneuron pairs (Figure 6) that are involved in the integration of sensory information from the environment and the physiological internal state of the animal. Processed outputs are then relayed to motor neurons or additional interneurons, eventually leading to an appropriate behavioral response. For instance, RIM neurons regulate reversal behaviors as a part of the locomotion circuit. The command interneuron AVA receives multiple sensory inputs and relays the signal directly to RIM neurons via electrical gap junctions. Tyramine released from RIM then suppresses head movements through RMD and SMD motor neurons (Pirri and Alkema, 2012). Suppression of these head movements is believed to facilitate efficient reversal behaviors to escape from noxious cues (Alkema *et al*., 2005).

While it has been shown that the ionotropic receptor LGC-55 mediates tyraminergic signaling underlying escape responses to mechanosensory cues (Donnelly et al., 2013), activation of GPCRs is thought to be the common mode of action for tyramine and octopamine signaling in *C. elegans*. Indeed, the *C. elegans* genome encodes three octopamine receptors (*octr-1*, *ser-3* and *ser-6*) and four tyramine receptors (*ser-2*, *tyra-2*, *tyra-3* and *lgc-55*) (Hapiak *et al*., 2013; Mills *et al*., 2012; Petrascheck *et al*., 2007; Pirri *et al*., 2009; Rex and Komuniecki, 2002; Rex *et al*., 2004, 2005).

Octopaminergic and tyraminergic signaling function in different neural circuits to govern diverse functions such as starvation-associated behaviors, locomotion, memory, innate immunity and decision-making. Table 2 summarizes the various target receptors and neurons in which these diverse functions are mediated. Tyramine and octopamine can orchestrate a wide range of behavioral and physiological processes by regulating the activity of a small number of target receptors. The recent review of Roeder provides valuable insights for understanding the role of tyramine and octopamine, which helps building a coherent picture from apparently random functions in the scope of energy homeostasis (Roeder, 2020).

While their profound influence on worm biology is clear, it remains elusive how these pleiotropic neuromodulators precisely function and interact in the *C. elegans* nervous system to mediate these diverse physiological and behavioral functions. Given the restricted number of octopaminergic and tyraminergic neurons as well as the limited number of target receptors, a precise spatiotemporal characterization of monoamine signaling would be required to truly understand the mode of action of octopaminergic and tyraminergic signaling.

**Table 2. Putative octopaminergic/ tyraminergic receptors in *C. elegans* and related functions.**

| Monoamine | Cell type | Receptor | Function | Reference |
|---|---|---|---|---|
| Octopamine | SIA | SER-3<br>SER-6 | Pharyngeal pumping via feedforward and feedback circuits | Liu *et al*., 2019 |
| | AWB | SER-6 | | |
| | SIA | SER-3<br>SER-6 | Hyperactive locomotive adaptation to fasting | Churgin *et al*., 2017 |
| | ASH | OCTR-1 | Regulation of innate immune responses to pathogenic infection | Sellegounder *et al*., 2018 |
| | AWB<br>SIA | SER-6 | Hunger-induced sensory valence in $CO_2$ response | Rengarajan *et al*., 2019 |
| Tyramine | ASH | TYRA-2 | Hunger-dependent multisensory decision making | Chute *et al*., 2019;<br>Ghosh *et al*., 2016 |
| | ASI | TYRA-3 | Nutritionally driven monoaminergic inhibition of nociception | Hapiak *et al*., 2013 |
| | AIY | SER-2 | Retrieval of long-lasting aversive olfactory imprinted memory | Jin *et al*., 2016 |
| | AVB<br>head motor neuron | TYRA-2 | Adult-learned olfactory aversive memory | |
| | Head sensory neuron | LGC-55 | | |
| | Intestine | SER-2 | Cell non-autonomous intestinal unfolded protein response of the endoplasmic reticulum ($UPR^{ER}$) activation | Özbey *et al*., 2020 |
| | | OCTR-1 | | |
| | RME | SER-2 | Regulation of head movement in initial phase of omega turn | Kagawa-Nagamura *et al*., 2018 |
| | VD motor neuron | SER-2 | Hypercontraction of muscles on ventral side for omega turn | Donnelly *et al*., 2013 |
| | AVB, RMD SMD, neck-muscles | LGC-55 | Inhibition of forward locomotion and suppression of head movement in the initial escape response | |

## 1.3. Fluorescent biosensors to study monoamine signaling dynamics *in vivo*

### 1.3.1. Fluorescent proteins in biosensors

The discovery of the green fluorescent protein (GFP) opened up a new chapter in optical *in vivo* imaging. Fluorescent proteins can be non-invasively visualized *in vivo* and provide precise spatial information on (sub)cellular structures, which makes them an ideal research tool for observing how protein targets are functioning within the cell. Mutagenesis approaches of GFP have yielded variants with a wide range of physicochemical properties, which provides significant benefits to the scientific community. For example, enhanced GFP (EGFP) shows higher folding efficiency at 37°C, which made it suitable for expression in mammalian models (Cormack *et al*., 1996). In addition, numerous color mutants such as blue, cyan and yellow fluorescent proteins allowed fluorescence imaging of two or more colors simultaneously (Specht *et al*., 2017). Currently, there are 774 fluorescent proteins registered on the fluorescent protein database (https://www.fpbase.org).

Fluorescent proteins are indispensable elements of myriads of genetically encoded fluorescent biosensors. Depending on the sensing mechanism of the fluorescent biosensors, one or more fluorescent proteins are incorporated. Genetically encoded fluorescent biosensors generally are fusions proteins connecting a sensing unit that is selective to a biomolecule of interest to one or more fluorescent proteins used as reporting module (Palmer *et al*., 2011). In addition, split fragments of fluorescent proteins are also used as a reporter in protein fragment complementation assays (PCAs). This entails the fluorescent signal to be detectable only when an interaction occurs between labeled proteins, which allows the fluorescent protein to become functional (Wang *et al*., 2020). Nevertheless, intact and fully functioning fluorescent proteins are more commonly used.

Irrespective of the type of biosensor, the signal from the activated sensing domain must be transformed into a detectable signal in a faithful manner. In genetically encoded fluorescent biosensors, this is mostly mediated by conformational changes of the sensor, hereby ultimately inducing change in fluorescence signal. Here, two noteworthy applications of fluorescent proteins within biosensors are introduced, in which they function as reporting modules to read out conformational changes.

The first approach is based on a physicochemical phenomenon called Förster resonance energy transfer (FRET). FRET has been established as a staple technique in the field of molecular cell biology. As the name suggests, the energy is transferred between two fluorophores, the so-called donor and acceptor molecules, in a non-radiative manner. For this, a considerable overlap between the emission and absorption spectra of both fluorophores is needed to ensure high FRET efficiency. Importantly, the efficiency of this process is also highly dependent on the physical distance between donor and acceptor. Therefore, FRET is often referred to as a “molecular ruler” as it can be used to precisely monitor the change in distance of two targets at a nanometer scale (Piston and Kremers, 2007).

However, FRET-based sensors generally suffer from low signal-to-noise ratios and a small dynamic range, which stems from the innate limitations of the FRET phenomenon itself. Also, designing FRET sensors is challenging as both donor and acceptor moieties should be correctly embedded within the target(s) so that the distance between both fluorophores robustly reflects the conformational change under study. Moreover, the use of multiple fluorescent proteins raises an additional concern as each protein could respond to changes in the environment with varying sensitivi. Potentially, this may lead to a misinterpretation of the results (Leavesley and Rich, 2016).

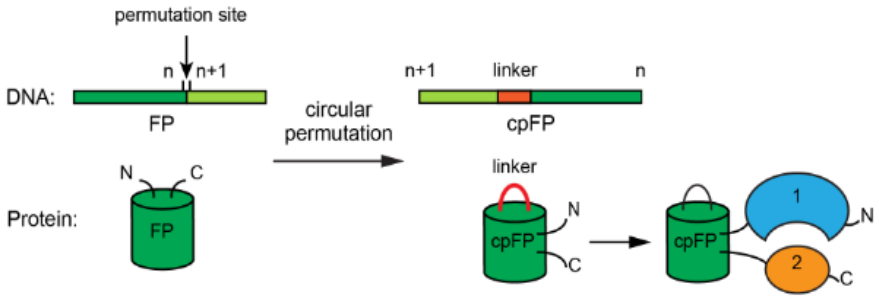


**Figure 7. Engineering of a circularly permuted fluorescent protein (cpFP)** (Kostyuk *et al*., 2019). The circular permutation of fluorescent protein is shown in DNA and protein level. The resulting new termini are fused to protein fragment 1 and 2. These two fragments can be different domains of a single protein, interacting subunits or proteins.

To circumvent these issues, a single circularly permuted fluorescent protein (cpFP) is often implemented as a reporting module. Initial structural studies of the GFP protein discovered that the rigid beta barrel structure surrounding the chromophore is the key attribute of the stability of the protein, ensuring robust fluorescence even in unfavorable conditions. Thus, by forming new termini closer to the chromophore by introducing a peptide linker to the GFP molecule (Figure 7), cpGFP was engineered to be more flexible and responsive to the conformational change it relays (Nagai *et al*., 2001).

FRET and cpFP tools are applied universally in a vast number of genetically encoded fluorescent biosensors. Specifically, within the context of this project, they are also implemented to investigate various aspects of neuromodulator signaling by measuring local concentrations of the neuromodulator, visualizing the conformational changes of of GPCRs or relaying GPCR activation by monitoring downstream events *in vivo.* In the following subchapters, currently available genetically encoded biosensors are presented in three categories according to the strategy employed to study monoaminergic signaling.

### 1.3.2. Sensors that target downstream components

GPCRs are heptameric membrane proteins that mediate various cellular responses by relaying external stimuli into the cells. While it is often portrayed that GPCRs have dichotomous on/off states depending on the presence of the agonist, this oversimplified explanation is misleading. Concerted approaches using X-ray crystallography, NMR, and molecular dynamics (MD) simulations have recently discovered the large dynamics of GPCR conformational states. In reality, the binding of agonist shifts the conformational equilibrium so that the activated conformation is more highly populated (Hilger *et al*., 2018; Latorraca *et al*., 2017; Weis and Kobilka, 2018).

As their name suggest, GPCRs are associated with G proteins that transduce GPCR activation intracellularly. The heterotrimeric G proteins consist of the $G_{\alpha}$ and tightly associated $G_{\beta\gamma}$ subunits, which all stay bound to each other when the receptor is at rest. Ligand binding causes conformational changes in the receptor protein, which induce the dissociation of the G protein from the activated GPCR. Dissociated G proteins further transduce the signal into the cell via several biochemical signaling cascades (Figure 8).

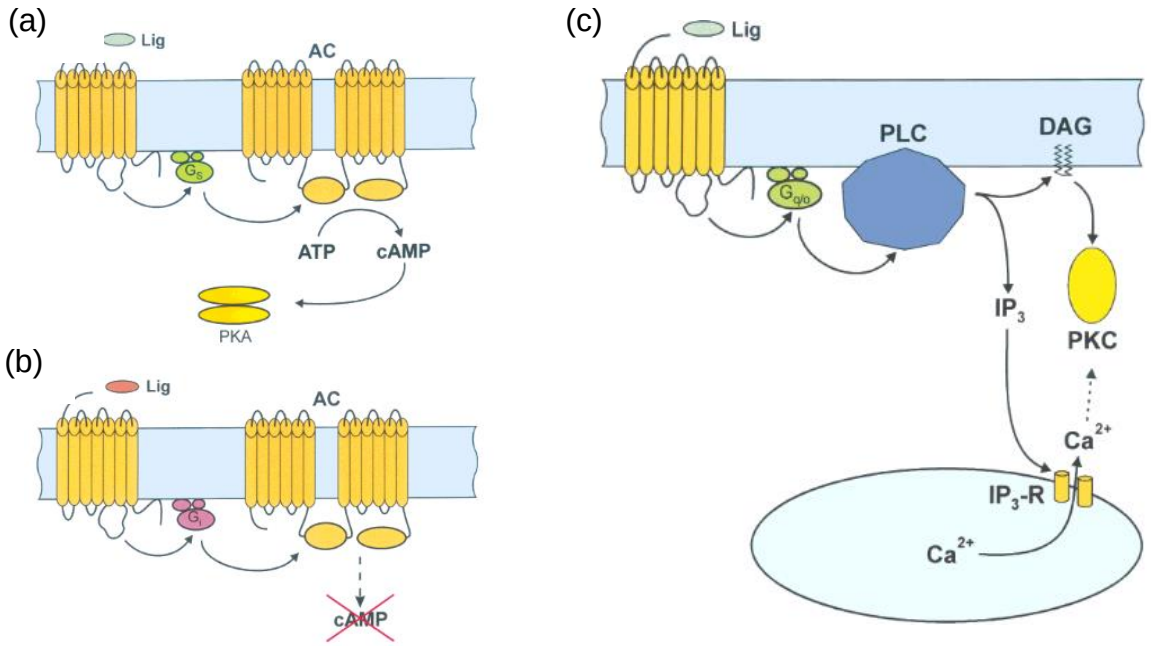


**Figure 8. GPCR signaling schemes. cAMP signaling pathways via (a) stimulatory G protein $G_s$, (b) inhibitory G protein $G_i$ and (c) intracellular $IP_3$/DAG signaling pathways via stimulatory G protein $G_{q/o}$** (Blenau and Baumann, 2001). For the cAMP-dependent pathway, the $G_{\alpha}$ subunit of the G protein dissociates from the receptor and has an effect on the activity of adenylyl cyclase (AC). As adenylyl cyclase (AC) converts ATP molecules to cAMP, the level of cAMP is either up-regulated by a stimulatory G protein ($G_s$) or conversely down-regulated by an inhibitory G protein ($G_i$), which as a result regulates the activity of protein kinase A (PKA) downstream (Figure 8a, b). The other GPCR signaling pathway is commonly known as the inositol 1,4,5-trisphosphate ($IP_3$) - diacylglycerol (DAG) pathway. Dissociated G proteins of the $G_{q/o}$ family stimulate phospholipase C β (PLC-β), which cleaves the membrane component phosphoinositol ($PIP_2$) into DAG and $IP_3$. $IP_3$ subsequently diffuses and binds ligand-gated calcium channels on either the endoplasmic or sarcoplasmic reticulum (ER or SR, respectively), resulting in calcium to be released into the intracellular domain of the cell (Figure 8c).

The intracellular signal transduction cascade entails change in the concentration of small molecules, second messengers and the activities of various enzymes. These in turn are involved in various molecular processes such as gene regulation, ultimately determining many cellular processes and various aspects of cell communication. In other words, a cellular effect is the elaborate outcome of a complex interplay among chemical messengers, membrane-bound lipid mediators and a wide variety of enzymes. Monitoring specific components within these signaling pathways can therefore provide important clues for our understanding of how and when these intracellular signaling events are manifested.

The most well-known example of a sensor relaying intracellular changes is the family of genetically encoded calcium indicators (GECIs), which are instrumental tools for studying the dynamics of calcium signaling. The regulation of intracellular calcium is important for diverse cellular functions including signal transduction within neuromodulation (Bagur and Hajnóczky, 2017).

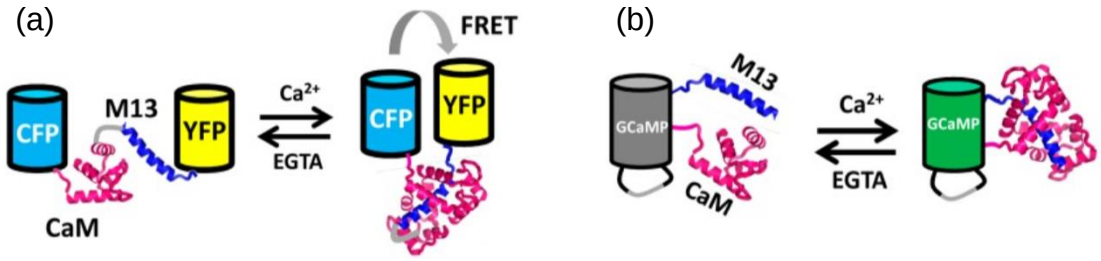


**Figure 9. Schematic overview of calcium sensors (a) FRET-based calcium indicator (b) cpGFP-based calcium indicator (GCaMP)** (Lindenburg and Merkx, 2014).

In 1997, two calcium probes, Cameleon and FIP-$CB_{SM}$, were independently developed based on the FRET principle (Bagur and Hajnóczky, 2017; Romoser *et al*., 1997). These calcium sensors consist of the calcium binding protein Calmodulin (CaM), the calmodulin binding peptide M13 and two orthogonal fluorescent proteins (Figure 9a). Upon binding of calcium, calmodulin interacts with M13 peptide, and the subsequent conformational change of the entire indicator protein results in a FRET signal. Alternatively, GCaMP indicators have adopted a single cpGFP to relay this conformational change (Figure 9b). GCaMP indicators are now frequently used tools to visualize neuronal activity, and these have also been used to study neurons of neuromodulatory networks (Nakai *et al*., 2001). For instance, GCaMP3 has been expressed in dopaminergic neurons of the mouse brain to visualize fear-evoked calcium signals (Gore *et al*., 2014). An extensive list of available variants of intracellular calcium indicators can be found in the review of Whitaker (Whitaker, 2010). In addition to intracellular calcium, second messengers such as cAMP and other effector proteins can be investigated using genetically encoded biosensors based on fluorescent proteins (Kim *et al*., 2021; Ma *et al*., 2018).

Monitoring the activity state and overall levels of pathway components downstream of the GPCR provides indirect, but robust signals that are greatly amplified during the signaling cascade. In addition, second messengers and kinases are universally shared

among many pathways, thus requiring little effort to use these indicators to probe different signaling events. At the same time, however, the readout is less straightforward due to the possible contribution of multiple different signaling pathways. It should be taken into consideration that the measurement may be skewed when the contribution of other signaling pathways is not tightly controlled or considered.

### 1.3.3. Sensors that monitor monoamine concentrations

Extracellular levels of monoamines are traditionally studied using analytical chemistry techniques such as microdialysis or fast-scan cyclic voltammetry (FSCV) (Jaquins-Gerstl and Michael, 2015). These *in vitro* techniques have greatly advanced our knowledge of monoamine signaling by providing reliable detection and quantification of monoamines. However, they are not suitable for measuring local concentrations of these molecules in an *in vivo* context.

To overcome this limitation, cell-based neurotransmitter fluorescent-engineered reporters (CNiFERs) were developed to reliably detect volume transmission of neurotransmitters in the brain *in vivo.* Briefly, CNiFERs are human embryonic kidney cells (HEK293) that are genetically engineered to express a specific target GPCR and genetically encoded calcium indicators (Figure 10). By introducing these engineered cells within the extracellular milieu of the nervous system, they can be used to study the release of neuromodulators *in vivo*. GPCRs expressed on the cell surface guarantee chemical specificity for the neurochemical under study, and corresponding signals are intracellularly transduced via the activation of $G_q$ proteins (Nguyen *et al*., 2010). As a result, the calcium level is elevated within the HEK293 cell and this change is relayed by a genetically encoded FRET-based calcium sensor located in the intracellular domain of the CNiFER. However, this method is not applicable to all GPCRs as not all couple to $G_q$. Thus, for GPCR signaling pathways that do not rely on $G_q$-mediated intracellular calcium release, promiscuous chimeric G proteins were used to redirect GPCR activation to the PLC/$IP_3$ pathway. With this approach, dopamine D2-CNiFER, which couples to the $G_{i/o}$ protein, was successfully developed to measure the dynamics of dopamine in the murine cortex (Muller *et al*., 2014).

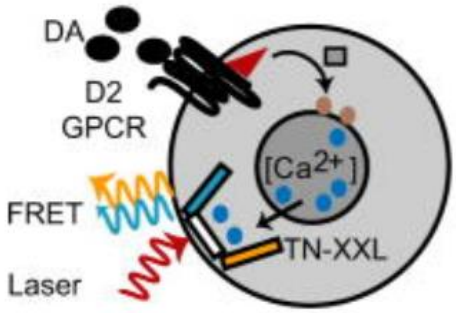


**Figure 10. A schematic overview of dopaminergic CNiFER (D2-CNiFER)** (Muller *et al*., 2014). Human embryonic kidney cells (HEK293) are engineered to express the dopaminergic D2 GPCR. Upon receptor activation, resulting fluctuations in calcium levels is monitored by a co-expressed FRET-calcium indicator (TN-XXL).

To date, CNiFERs have been implemented to monitor the release of acetylcholine (Nguyen *et al*., 2010), dopamine and norepinephrine (Muller *et al*., 2014). However, CNiFERs slightly deviate from conventional genetically encoded-sensors as they are cell-based sensors. Moreover, they require physical implantation and their application is quite limited due to their large size. In fact, they have been exclusively implemented in the murine brain. Furthermore, this method is subject to unwanted immunological reactions in different animals as it is based on cells of human origin.

### 1.3.4. Sensors that monitor GPCR activation

GPCR activation is initiated by the binding of the extracellular ligand to the receptor. This induces conformational changes in the GPCR protein that eventually transduce the activation signal into the intracellular milieu. Therefore, it is intuitive to devise an assay that detects the active conformation of the receptor upon ligand binding. In the following sections, two novel types of sensors are introduced. Both types of sensors monitor the activation of the receptor, however, the strategy by which this is reported differs. A first group of sensors consists of a modular system based on a GPCR-tethered transcription factor. When a ligand binds the GPCR, the conformational change of the receptor facilitates docking of β-arrestin on the activated receptor. This protein-protein interaction results in a release of the transcription factor and subsequent expression of a reporter gene. In contrast, the other type of sensor takes a more straightforward configuration in which a cpFP is fused to the inert GPCR protein as a reporting module. Here, conformational changes by ligand binding are directly converted to a change in fluorescence intensity.

#### 1.3.4.1 Transcription factor-based sensors

Protein-protein interactions (PPIs) between the activated receptor and other effectors can provide information about the activation of the signaling pathway. This first category of sensors utilizes GPCR-activated transcriptional factors to initiate reporter transgene expression. A Tango GPCR assay exploits the PPI of the desensitization process (Barnea *et al*., 2008). Within the context of negative feedback regulation, β-arrestin proteins are recruited from the cytoplasm to activated GPCRs in order to block receptor activity (Luttrell and Lefkowitz, 2002). Tango assays hinge on a tobacco etch virus (TEV) protease fused to β-arrestin and a transcription factor tethered to a GPCR through a TEV cleavage site. Upon docking of the β-arrestin to the activated GPCR, the transcription factor is released from the GPCR by the protease and subsequently diffuses to the nucleus. Then triggers the expression of a reporter gene (Figure 11A). In the original publication, a luciferase reporter was used to measure GPCR signaling (Barnea *et al*., 2008). However, several reporter gene variations have been reported. For instance, an EGFP reporter has been used to implement a Tango system based on the serotonin 2C receptor (5-$HT_{2C}$R) (Watanabe *et al*., 2016). A commercially available Tango assay adopts β-lactamase, which cleaves pre-loaded substrates (Frostne *et al*., 2011; Vedvik *et al*.). These substrates initially emit green fluorescence,

but after cleavage, blue fluorescence is observed. The blue to green fluorescence ratio of two FRET responses is used as readout.

Transcriptional reporter-based assays such as Tango have been a popular choice for studying PPI dynamics as they are capable of converting an otherwise transient interaction into a stable and robust signal as a product of their signal amplification scheme. Furthermore, they do not require real-time microscopy as the products of the reporter gene are generally stable once expressed. Also, their modular architecture makes them more scalable for generating multiple sensors. Using Tango sensors, sites of dopaminergic signaling have been visualized in the *Drosophila* brain (Inagaki *et al*., 2012) and high-throughput GPCR-based drug screening and deorphanization of human GPCR experiments have been conducted (Dogra *et al*., 2016; Kroeze *et al*., 2015).

However, the long lifetime of the transcriptional reporter entails that multiple signaling events at different time points cannot be effectively resolved using this type of readout. iTango2 and SPARK (specific protein association tool giving transcriptional readout with rapid kinetics) were developed to mediate this issue of low temporal resolution (Lee *et al*., 2017; Kim *et al*., 2017). In this next generation of the Tango sensor, the activation of the transcription factor not only requires the specific interaction of the GPCR and β-arrestin, but also exposure to blue-light. Blue-light illumination uncages the cleavage site that links the transcription factor to the GPCR from a light-sensitive LOV (light-oxygen-voltage-sensing) domain (Figure 11B). This additional optogenetic control offers the possibility to specify the time window for the observation of GPCR activation.

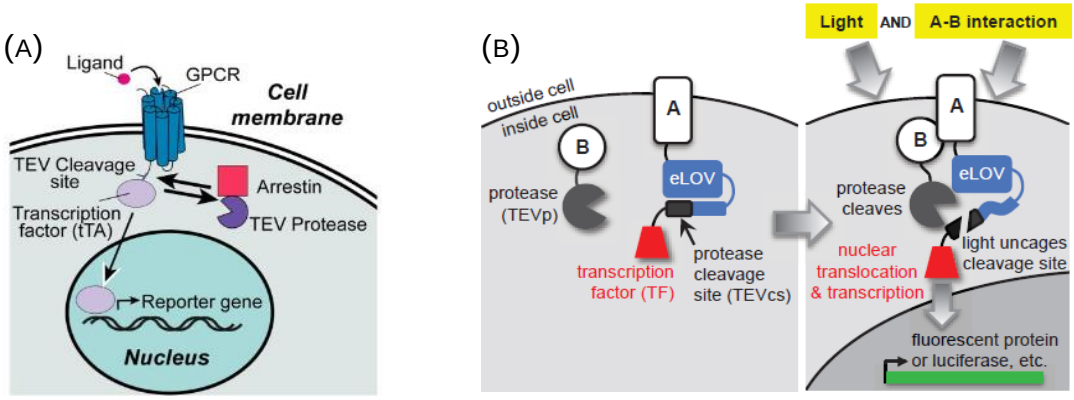


**Figure 11. Transcription factor-based sensors (A) Tango assay** (Barnea *et al*., 2008) **(B) SPARK** (Kim *et al.*, 2017). Both approaches are based on the protein-protein interaction (PPI) of arrestin and a GPCR. In case of SPARK, A is considered GPCR and B is an arrestin-TEV protease complex. Conformational changes induced by ligand binding induces the docking of arrestin onto the GPCR, and an artificial transcription factor is cleaved by TEV protease. Transcription factors then diffuse into the nucleus, where a reporter gene is expressed.

However, visualizing multiple sequential signaling events still remains difficult. Also, it takes a relatively long time for the signal to be detected (in the scale of multiple hours) due to the nature of gene expression. In other words, transcriptional assays are still not adequate for understanding real-time dynamics of receptor activation and deactivation.

#### 1.3.4.2 GPCR based real-time sensors using cpFP

GPCRs generally induce slow but long-lasting cellular changes. Also, unlike ionotropic receptors, GPCR signaling is not restricted to the synaptic cleft. Thus, the duration of receptor activity and the subcellular location of GPCR activation provide key information that is invaluable for elucidating the precise actions of neuromodulator signaling. Hence, specific experiments that require high spatiotemporal resolution can highly benefit from the cpFP-based GPCR sensors. In these sensors, conformational states of the receptor are directly relayed to a cpFP module, offering real-time detection of GPCR signaling. As these conformational changes are fast, the sensor is capable of portraying accurate and agile on-and-off dynamics of GPCR signaling with tens to hundreds of milliseconds of temporal resolution. Conceptually, the structure of both prototypical cpFP-based GRAB and dLight sensors is analogous (Patriarchi *et al*., 2018; Sun *et al*., 2018). Both can be subdivided into a sensor module, the reporter module and peptide linkers connecting the two modules.

A good reporter module should respond to the structural change of the receptor with high sensitivity. As previously mentioned in 1.3.1, cpFPs are sensitive to conformational changes and are therefore well-suited to act as a reporting unit. Initially, green fluorescent proteins such as cpGFP and cpEGFP were implemented (Patriarchi *et al*., 2018; Sun *et al*., 2018), but the successful application of a red fluorescent cpmApple within the DA-sensor RdLight1 has recently also been reported (Patriarchi *et al*., 2020). This expanded sensor color palette opens up a variety of independent multiplexing possibilities with other optogenetic actuators and reagents that typically are built on green fluorescent proteins. A list of currently available GPCR-based sensors is listed in Table 3.

**Table 3. GPCR based real-time sensors.**

| Neurotransmitter | Sensor | Indicator | Reference |
|---|---|---|---|
| Dopamine | dLight1 | cpGFP | Patriarchi *et al*., 2018 |
| | RdLight1 | cpmApple | Patriarchi *et al*., 2020 |
| | $GRAB_{DA}$ | cpEGFP | Sun *et al*., 2018 |
| | R-GenGAR-DA | cpmApple | Nakamoto *et al*., 2020 |
| Serotonin | $GRAB_{5\text{-}HT}$ | cpGFP | Wan *et al*., 2021 |
| | psychLight | cpGFP | Dong *et al*., 2021 |
| Acetylcholine | GACh | cpGFP | Jing *et al*., 2018 |
| | $GRAB_{Ach3.0}$ | cpEGFP | Jing *et al*., 2020 |
| Norepinephrine | $GRAB_{NE}$ | cpEGFP | Feng *et al*., 2019 |
| | nLight | cpGFP | Oe *et al*., 2020, Patriarchi *et al*., 2018 (Supplementary Fig.3) |

As a sensing unit, the native GPCR protein provides an exquisitely suited backbone as it shows high specificity and affinity to ligands at physiological concentrations *in vivo*. For the ideal sensor design, the conformational change of the receptor upon ligand binding should directly alter the structure of the reporter module and the intensity of fluorescence accordingly. Therefore, identifying the region with the maximum conformational mobility is an integral task of GPCR sensor design. Ideally, the crystal structure of the apo- (unbound) and ligand-bound form can be obtained by NMR and X-ray crystallography (Bostock *et al*., 2019; Casiraghi *et al*., 2019; Shimada *et al*., 2019). However, homology modeling can be used as a suitable alternative in the likely case that these data are not available. Advances in structural analysis of GPCRs, in particular of the β2 adrenergic receptor (Bang and Choi, 2015), have demonstrated that transmembrane domains 5 and 6 undergo large conformational changes upon ligand binding, therefore identifying intracellular loop 3 (ICL3) as a critical point within these extensive conformational changes (Rasmussen *et al*., 2011). Based on this knowledge, ICL3 was entirely replaced by a fluorescent indicator in the previously reported dopamine dLight sensors (Figure 12). However, GRAB sensors were designed to leave a portion of ICL3, which suggests that complete removal of ICL3 is not necessary. It is hypothesized that this remaining ICL3 region serves a function as the linker sequence.

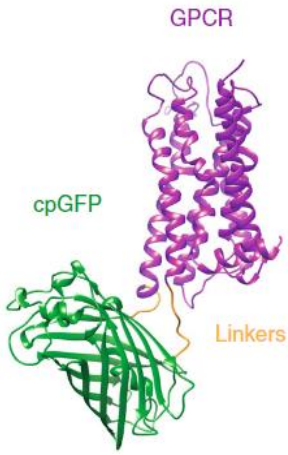


**Figure 12. Generalized structure of genetically encoded GPCR sensors based on cpFP approach** (Patriarchi *et al*., 2018). A cpGFP module is inserted in the third intracellular loop of a GPCR with the short stretches of linkers.

When the cpFP is inserted in ICL3, short peptide linkers are placed on each terminus of the permutant to reduce steric clash that could impede proper folding of each domain, ensuring the flexibility of the indicator. Yet, short linkers are recommended for the maximum coupling between the sensing domain and the reporting unit, as the conformational change can be lost during the transmission by the bond rotation of the linkers (Nasu *et al*., 2021). To date, there is no consensus sequence for these linkers. However, it is generally considered that the linker sequences are of critical importance for determining the success of sensor engineering along with the determination of the insertion site.

Once the GPCR sensor is constructed, it is typically expressed in a cellular system to be functionally characterized (Patriarchi *et al*., 2019). Ideally, the sensor should show high ligand sensitivity and specificity. Sensitivity can be interpreted as how certain a type of neurochemical of interest can be faithfully detected, which is a result of both receptor affinity and the dynamic range of the fluorescence response. High contrast of change within the fluorescence response ($\Delta F/F_0$) upon ligand binding contributes to reliable detection. Additionally, binding affinity can be fine-tuned by introducing either random or targeted mutations within the ligand-binding pockets or the G protein-coupling site (Patriarchi *et al*., 2019).

On the other hand, specificity stems from the binding selectivity of the receptor. Even though endogenous GPCRs generally respond to more than one neurochemical, they can discriminate structurally similar neurotransmitters with a considerable difference in selectivity. GPCR-based sensors retain this selectivity and it has even been demonstrated that they can respond to pharmacological agonists and antagonists with high sensitivity (Patriarchi *et al*., 2018; Sun *et al*., 2018).

Fast rise-time ($\tau_{on}$) and fluorescence decay kinetics ($\tau_{off}$) are important for a high temporal resolution. Rise-times of the GPCR-based sensors lie in the scale of milliseconds (Jing *et al*., 2019), which is outstandingly faster compared to other techniques that rely on downstream signaling cascades. While fluorescence decay kinetics generally take longer than the rise-time kinetics due to the photophysical property of fluorescence excitation and emission, they are fast enough (100-2000ms) to reliably measure the activation of the metabotropic receptor (Jing *et al*., 2019).

Furthermore, the influence of newly developed sensors on the physiology of their host cell(s) should be tested prior to *in vivo* assays. Since bulky cpFP substituents are likely to hinder proper docking of G proteins and arrestins, GPCR sensors are generally not able to properly transduce signals downstream while still competing with endogenous receptors for the ligand. Expression levels should be within tolerant levels to avoid any non-specific detrimental cellular effects of sensor expression.

While real-time sensors have enormous potential for future applications, the optimization process remains a considerable bottleneck in the development and implementation of different GPCR sensors within neuroscience. From insertion site selection to optimization of the peptide linker sequence, each sensor construct has to be designed and tested respectively. In general, there is a considerable delay in structural studies of GPCR proteins, thus unavoidably our current understanding of the structural mechanism of the sensor is insufficient for a rational design approach. Therefore, the optimization currently relies mainly on trial-and-error based engineering and screening, which requires considerable amount of effort and resources. However, a handful of optimized GPCR sensors that have been implemented to date already pinpoint to certain features of the insertion site and linker design that can facilitate the application of these sensor methodologies to new GPCRs (Feng *et al*., 2019; Patriarchi *et al*., 2018, 2020; Sun *et al*., 2018)

Nevertheless, development of a panel of GPCR sensors should continue. These sensors form a versatile tool that can decipher mechanisms of neuromodulation and enable us to answer temporal questions regarding how fast and how long monoamines bind to their receptor, as well as spatial questions regarding how far monoamines can signal and where they bind on target cells. Furthermore, understanding spatiotemporal dynamics of monoaminergic signaling can provide meaningful clues to unravel the relationship between neural circuits and behavioral effects. For example, coupled with optogenetically-controlled release of neurotransmitters from specific neuronal tissues, GPCR sensors can help identifying which neurons are involved in neuromodulation as well as how the neuromodulation affects the neural circuit.

# 2. Materials and Methods

Experiments were conducted in compliance with the internal protocols provided by the host lab. Detailed versions of the protocols can be found in the appendix.

## 2.1. Development of sensors

### 2.1.1. Resuspension of gBlock™

The cpmApple sequence was retrieved from the RdLight1 sensor sequence from the original paper (Patriarchi *et al*., 2020) and ordered as a gBlock™ gene fragment from Integrated DNA Technologies (IDT, Leuven, Belgium). As it was provided in a dry state, it was resuspended before use. To prevent the loss of the dry pellet, the tube was briefly spun down in a microcentrifuge before opening. Milli-Q was then added to a final concentration of 10 ng/μL and vortexed. Then, it was incubated at 50°C for 15-20 minutes, and the final concentration was verified before use.

### 2.1.2. TOPO TA Cloning (P0020_v1)

The resuspended gBlock gene fragment was directly inserted into the pCR™4-TOPO™ plasmid vector using a TOPO TA cloning kit (Invitrogen). The linearized pCR4™-TOPO™ vector contains thymidine overhangs with covalently attached topoisomerases, which ligate external DNA into the vector. For the attachment of the complementary adenine overhang to the 3' end of the gBlock fragment, 0.5 μL REDTaq® ReadyMix™ PCR Reaction Mix (Sigma-Aldrich), 1μL dATP (Sigma-Aldrich) and diluted 10x buffer was incubated at 72°C for 15 minutes. Then, the TOPO cloning reaction mixture was prepared by mixing 3 μL of the incubated gBlock product, 1μl salt solution and 1 μl TOPO vector into a PCR tube. The mixture was incubated for 30 minutes at room temperature.

### 2.1.3. Q5 High-fidelity PCR (P0010_v1)

Q5® High-Fidelity DNA Polymerase shows a proofreading activity and low error rates. Therefore, it is suitable for template amplification where high fidelity amplification is required. For a 25 μl reaction mixture, 1 ng of template DNA was calculated in volume. On ice, 5 μl 5X Q5 reaction buffer, 0.5 μl 10 nM dNTPs (Roche), 1.25 μl 10 μM forward primer, 1.25 μl 10 μM reverse primer, and 0.25 μl Q5 high-fidelity DNA polymerase (Bioké) was added to the template DNA and the rest of the volume was filled with Milli-Q (Merck) up to 25 μl. The mixture was gently mixed and placed on a thermal cycler according to the program as indicated in Table 4.

**Table 4. Thermocycling program for Q5 High-fidelity PCR.**

| Step | | Temperature | Time |
|---|---|---|---|
| Initial denaturation | | 98°C | 30 sec |
| Denaturation | 25-35 Cycles | 98°C | 10 sec |
| Hybridization | | 50-72°C (or gradient) | 30 sec |
| Extension | | 72°C | 30 sec/ kb |
| Final extension | | 72°C | 2 minutes |
| Hold | | 4-10°C | |

2.1.4. Q5 Site-directed mutagenesis for substitution (New England Biolabs)

Q5 site-directed mutagenesis can be used to introduce site-specific modifications in a DNA sequence using two primers and Q5 Hot Start High-Fidelity DNA Polymerase (New England Biolabs). For a site-directed substitution, the forward primer is designed to contain the desired nucleotide change in the center and a minimum of 10 complementary nucleotides at the 3' side of the mutation. The reverse primer is designed to anneal back-to-back so that the 5' end of the two primers meet each other. For the initial exponential amplification, 12.5 μL Q5 Hot Start High-Fidelity 2X Master Mix (New England Biolabs), 1.25 μL forward primer, 1.25 μL reverse primer, 1 μL template DNA and 9 μL Milli-Q were gently mixed in a PCR tube. The reaction mixture was then placed in a thermal cycler following the same program as for Q5 PCR (Table 4). When the amplification was finished, 1 μL PCR product, 5 μL 2X KLD (kinase, ligase, Dpnl) Reaction buffer, 1 μL 10X KLD Enzyme Mix and 3 μL Milli-Q were added in another PCR tube. The reaction mixture was mixed by gentle pipetting and incubated at room temperature for 5 minutes.

2.1.5. Gibson Assembly (P0077_v1)

Gibson assembly is a useful molecular cloning technique that can join multiple DNA fragments at once. DNA fragments must contain overlapping regions at opposite ends. Briefly, the assembly involves an exonuclease to catalyze the sequential removal of nucleotides at the 5' end of each sequence, after which the remaining single strands anneal to each other. Next, a DNA polymerase fills the gaps and DNA ligase joins the nicks of adjacent segments, resulting in a seamless assembly of fragments. For an optimal reaction set up, generally 1:2 vector to insert DNA molar ratio is recommended. Using the online NEBioCalculator tool (https://nebiocalculator.neb.com), optimal quantities were calculated per construct for 50 ng vector, and Milli-Q was added to reach a total volume of 10 μl. Then, 10 μl HiFi DNA assembly master mix (New England Biolabs) was added and the samples were incubated in a thermocycler at 50°C for 15 minutes to one hour.

### 2.1.6. Directional TOPO expression cloning (P0021_v1)

The pcDNA™3.1/V5-His TOPO™ vector Kit (Invitrogen) was used to clone amplified PCR products into the pcDNA3.1 vector for mammalian expression. Prior to the PCR, it is necessary to design primers that include the 4-base pair overhang sequence CACC at the 5' end of the forward primer. The overhang of the amplicons is complementary to the GTGG overhang of the expression vector (Figure 13). This not only guides a correct orientation of insertion, but also facilitates proper initiation of translation in mammalian cells within the context of a Kozak sequence.

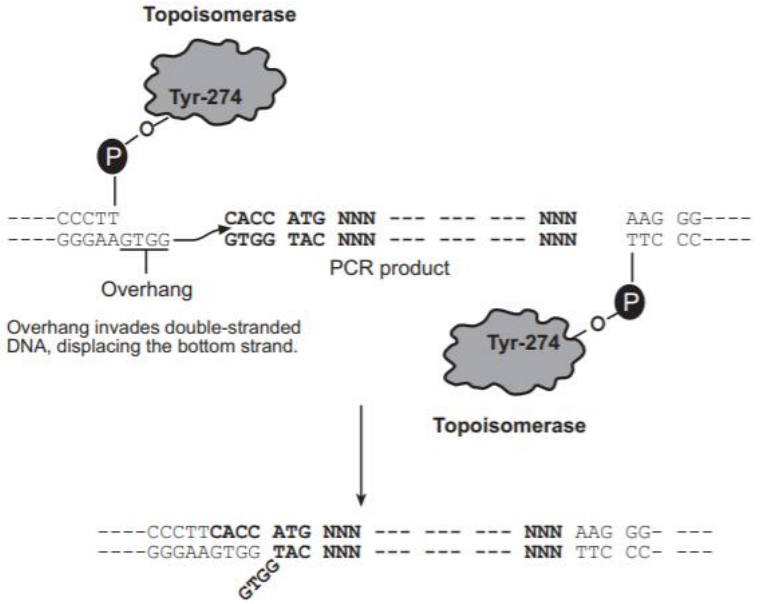


**Figure 13. Mechanism of directional TOPO expression cloning** (Thermo Fisher).

Before setting up the reaction mixture, the volume of PCR products was calculated for 1 μl TOPO vector using a 0.5:1 to 2:1 molar ratio of (PCR product): (TOPO vector) to ensure optimal results. The calculated amount of PCR product was mixed with 1 μl salt solution and 1 μl TOPO vector. Milli-Q was then added to a final volume of 5 μl. The reaction mixture was incubated at room temperature for 15 minutes, and placed on ice for subsequent transformation.

### 2.1.7. Restriction digest (P0018_v1)

The backbone of a vector can be cut with restriction enzymes for restriction-ligation or elimination of unwanted plasmid contaminants. For the total volume of 20 μl, 2 μl plasmid (up to 1 μg) was mixed gently with 15 μl Milli-Q, 2 μl 10X FastDigest® Green buffer (ThermoFischer) and 1 μl FastDigest® enzymes. The mixture was incubated at 37°C for 5 minutes. The digested products were checked by gel electrophoresis. If the enzyme successfully cuts the vector, a DNA band appears at a slightly higher position compared to the undigested vector as the original vector has a supercoiled conformation whereas the digested vector is linearized. Thus, digested products run slower.

### 2.1.8. Transformation of competent cells (P0024_v1)

Competent cells can be transformed with plasmid DNA using a brief heat shock. When competent cells take up foreign genetic material, this process is called transformation. DH5α is an *E. coli* cell line that is engineered to maximize transformation efficiency. For transformation, DH5α cells were thawed on ice and 1-5 µl of plasmid DNA was gently dispensed without pipetting up and down. The tube was then incubated on ice for 30 minutes, after which cells were heat shocked at 42°C for 30 seconds, and immediately transferred onto ice for 2 minutes. Then, 250 µl SOC medium was added to the vial, and the vial was incubated in a shaker at 37°C for 1 hour. The bacterial culture was then spread on a selective plate and incubated overnight at 37°C. Bacterial colonies were analyzed by colony PCR.

### 2.1.9. Colony PCR (P0012_v1)

Colony PCR was performed to identify colonies that have taken up the plasmid with the DNA of interest. As colony PCR can be directly performed on bacterial colonies, it provides a quick preliminary check prior to sequencing of individual plasmids. For colony PCR, poison primers were designed to amplify a region spanning the insert and its flanking sequences in the backbone. A master mix was prepared by mixing 6.75 µl REDTaq ReadyMix, 0.5 µl 10 µM forward primer, 0.5 µl 10 µM reverse primer and 2.5 µl Milli-Q per reaction, which was distributed into PCR tubes. Single colonies were picked from selective plates and added to the PCR mix. For storing colonies, 1µl of this bacteria-REDTaq mixture was then dispensed on a new ampicillin selective LB plate and incubated overnight at 37°C. PCR tubes containing the remaining volume were placed in the thermocycler according to the program in Table 5. Once the colony PCR was completed, the amplified products were analyzed using gel electrophoresis, and positive colonies were retrieved for plasmid purification from the plates on which single colonies were spotted.

**Table 5. Thermocycling program for colony PCR.**

| Step | | Temperature | Time |
|---|---|---|---|
| Initial denaturation | | 95°C | 10 minutes |
| Denaturation | 30 Cycles | 95°C | 45 sec |
| Hybridization | | 55°C (or gradient) | 45 sec |
| Extension | | 72°C | 1 minute/kb |
| Final extension | | 72°C | 2 minutes |
| Hold | | 4-10°C | |

### 2.1.10. Gel electrophoresis (P0016_v1)

Gel electrophoresis uses an electric current to separate DNA fragments based on their size, and the approximate size of the amplified PCR products can be estimated by parallel loading of DNA ladders. For the preparation of an agarose gel, 1 g agarose was added to 100 ml TAE buffer and microwaved until completely dissolved. 5 μl GelRed, which intercalates with DNA and can be visualized by UV light, was then added to the molten agarose, after which the mixture was poured into the cast with a comb. When the agarose gel was solidified, the comb was carefully removed, and the gel placed into an electrophoresis tank containing TAE buffer. Loading dye was added to the PCR products before loading, except when REDTaq was used. After loading samples onto the gel, the lid was placed back on the electrophoresis tank and cables were connected to the correct sockets. The voltage was set around 100-120V. After the run, the gel was visualized using the Proxima UV transilluminator (Isogen Life Science).

### 2.1.11. Gel extraction (P0017_v1)

After gel electrophoresis, PCR products were extracted from the gel and purified for further analysis. In this case, large wells (holding up to 50 μl PCR product) were used for higher recovery, and lower voltage was used for a clear separation of the bands. After the run, the gel was placed on the UV transilluminator and corresponding bands were excised with a clean scalpel. Excised gel strips were collected into pre-weighed 1.5 ml Eppendorf tubes and exact masses calculated. The Zymoclean Gel DNA Recovery kit (Zymo Research) was used for purification. Briefly, for each volume of agarose gel, 3 volumes of ADB solution were added to the Eppendorf tube. The tube was then incubated at 50°C until the gel piece was completely dissolved, and the melted solution transferred to the Zymo-Spin column in a collection tube. This was centrifuged at 16,000 x g for 60 seconds and the flow-through discarded. Next, 200 μl DNA wash buffer was added, and the column was centrifuged for another 30 seconds. This wash step was repeated, after which15 μl DNA elution buffer was added directly to the column matrix, and the column was centrifuged for 60 seconds in a new 1.5 ml tube for the collection of eluted DNA.

### 2.1.12. Isolation of the plasmid DNA (P0027_v1)

The Genelute Miniprep Kit (Sigma-Aldrich) was used for small-scale isolation of plasmid DNA from the transformed bacteria. The method is based on the principle of alkaline lysis of the bacterial cell and adsorption of the DNA onto silica in high concentration of salt. Freshly grown overnight culture was prepared the day before the miniprep, and the cells were harvested by centrifugation. After discarding the supernatant, pellets of cells were resuspended in 200 μl Resuspension solution and vortexed. 200 μl Lysis Solution was then added and gently inverted to mix. Without exceeding the 5 minutes of lysis, 350 μl Naturalization solution was added and the mix was centrifuged at 12,000 x g for 10 minutes to sediment the debris. In the meantime,

a binding column was prepared by adding 500 μl Column Preparation Solution. The column was spun down at 12,000 x g for 1 minute, and the resulting flow-through discarded. The clear lysate was then transferred to a binding column and spun down for 30 seconds. Flow-through was discarded, after which 500 μl Wash A Solution was added and centrifuged for 1 minute. Flow-through was again discarded and the wash step was repeated with 750 μl Wash B solution. The column was spun for 1 minute to dry with its lid open. Finally, the column was transferred to a new collection tube and 35 μl of Elution Solution was added in the center of the filter of the column. 1 minute of incubation time before the elution generally yielded higher DNA concentrations. The DNA concentration was measured using a NanoPhotometer (Implen) against the Elution Solution as a blank. Purified plasmid DNA was used to prepare the sequencing samples and the remaining volume was stored at -20°C with proper labeling.

### 2.1.13. DNA Sequencing

DNA sequencing was outsourced to LGC genomics, GmbH, Germany. Samples were prepared from the purified plasmid DNA to meet the concentration requirement of 100 ng/μl as specified in the sample guidelines. As for the volume, Ready2 Run samples were prepared to be 14 μl in total including 2 μl custom primers for sequencing (500 nM). Flexi Run required a minimum volume of 15 μl. For the Flexi Run, sequencing primers were selected from the online ordering system. LGC genomics processed the sequencing run of the samples.

Once the sequencing results were available, they were aligned using the Nucleotide BLAST feature “align two or more sequences” from the NIH website (https://blast.ncbi.nlm.nih.gov/Blast.cgi). Sequencing results were entered as a query sequence and the desired target sequence was entered as a subject sequence using the highly similar sequences (megablast) option.

### 2.1.14. Creating bacterial glycerol stocks (P0026_v1)

Bacterial glycerol stocks are created parallel to the plasmid stocks for long-term storage of plasmids. This way, plasmid DNA can be easily amplified when more plasmid DNA is needed without retransformation. Glycerol prevents damage to the cell membrane and stabilizes the frozen bacteria at -80°C. For the glycerol stock, a liquid culture was freshly inoculated and grown overnight at 37°C in a shaking incubator. 500 μL of the overnight culture was then mixed with 500 μL of 60% glycerol in a 2 mL cryovial. After 2 weeks, glycerol stocks were checked by streaking on an LB agar plate and bacterial growth was observed.

## 2.2. *In vitro* cell work

### 2.2.1. Endotoxin-free plasmid DNA purification (p0028_v1)

For transfection, plasmid DNA should be isolated and purified free of endotoxin. Also known as lipopolysaccharide (LPS), endotoxin is a component of the plasma membrane of gram-negative bacteria and the most common contaminant in plasmid purification. High levels of endotoxins are known to affect transfection efficiency, cell viability, intracellular biology and induce unwanted immune responses in cell culture. The NucleoBond EF kit (Machery-Nagel) was used to prepare endotoxin-free plasmid. Due to its larger volume, it is commonly referred to as maxiprep. 100 ml of LB medium was freshly inoculated and incubated overnight. The next day, bacterial cells were harvested by centrifuging the culture at 6,000 x g for 15 minutes at 4°C. The supernatant was discarded and the pellets resuspended in 8 ml Buffer RES-EF with RNase A. The mixture was transferred to a 50 ml plastic Falcon tube. 8 ml lysis buffer LYS-EF was added and inverted 5 times for mixing. The sample was incubated for 5 minutes at room temperature. In the meantime, a column filter was inserted into the NucleoBond Xtra Column, and 15 ml Equilibration buffer EQU-EF was applied onto the rim of the column filter to wet the entire filter. 8 ml Neutralization Buffer NEU-EF was added to the suspension of cell lysates and the tube was inverted until the blue color turn completely colorless. After 5 minutes of incubation, the suspension was homogenized by vigorous shaking in order to prevent clogging of the filter. The suspension was poured into the column filter. When the column was emptied by gravity flow, it was washed with 5 ml Filter Wash Buffer FIL-EF. The column filter was discarded and the column was washed with 35 ml Wash Buffer ENDO-EF. When the column was emptied, 15 ml Wash buffer WASH-EF was added. The plasmid DNA was eluted with 5 ml Elution Buffer ELU-EF, and the eluate was collected in a 50 ml centrifuge tube. 3.5 ml isopropanol was added to the eluate for precipitation, and the sample was centrifuged at 15,000 x g for 30 minutes at 4°C, after which the supernatant was discarded. 2 ml 70% ethanol was added to the pellet and centrifuged at 15,000 x g for 5 minutes at room temperature. The pellet was dried and 200 µL endotoxin-free Buffer TE-EF was added for reconstitution. The final concentration was checked with a NanoPhotometer (Implen).

### 2.2.2. Transfection with LTX (P0037_v1)

Plasmids can be artificially introduced into eukaryotic cells by means of transfection. Transfection with sensor constructs was based on lipofection (liposome transfection) using Lipofectamine LTX (Invitrogen). The reagent forms cationic lipid vacuoles, called liposomes, which encapsulates negatively charged genetic materials. When incubated with the cells, liposomes fuse with the cell membrane and release the vector DNA into the cell. Transfection was performed in an L2 lab by courtesy of Elke Vandewyer and all procedures followed the general guidelines for Biosafety class 2. Transfected cells were cultured in 16 well-plates (LabTek Chamber Slid with cover glass sterile, Thermo Fisher) in 5% $CO_2$ for 1 to 2 days.

## 2.3. Fluorescence imaging

### 2.3.1. Preparation of HBSS (Hank's Balanced Salt Solution)

HBSS contains inorganic salts and glucose to maintain physiological pH and osmotic balance for the cells. Therefore, HBSS was used to wash the cultured cells prior to the fluorescence imaging. 8 g NaCl, 400 mg KCl, 140 mg $CaCl_2$, 100 mg $MgSO_4$-$7H_2O$, 100 mg $MgCl_2$-$6H_2O$, 60 mg $Na_2HPO_4$-$2H_2O$, 60 mg $KH_2PO_4$, 350 mg $NaHCO_3$ and 1 g D-Glucose (Dextrose) were dissolved in 800 ml of distilled water. Once all the components were dissolved, the solution was filled up to 1 L. HBSS was also used to prepare octopamine solution.

### 2.3.2. Fluorescence Imaging

For the fluorescence imaging, an AxioObserver Z1 microscope (Zeiss) with 5X and 20X objectives, a Colibri2 LED illumination platform, and an ORCA-Flash4.0 V2 camera (Hamamatsu) was used. Image acquisition was performed using Metamorph (Molecular Devices) software. The confluency of the cultured cells was checked prior to changing the medium with HBSS buffer. For the wash, existing cell culture medium was pipetted out and discarded. 150 μl HBSS was slowly added to the wall of each well. After the wash, basal fluorescence was measured. For addition of octopamine, 50 μl 1 mM octopamine solution was slowly added to the well at the side of the well. Immediately after adding octopamine, 2 sequential images were acquired every 30 seconds using time-lapse mode. For all the acquisition, brightfield and fluorescence images were taken in parallel. The brightfield image was taken with an exposure time of 20 ms. For fluorescence imaging, the excitation wavelength was set to 588 nm and fluorescence emission was observed at 635 nm. The exposure time of fluorescence imaging was set to 200 ms.

### 2.3.3. Quantification of fluorescence intensity

ImageJ 1.53e (National Institutes of Health, USA) was used for image processing. For the quantification of fluorescence intensity, the corrected total cellular fluorescence (CTCF) was calculated as follows:

$$\text{CTCF} = \text{Integrated density} - (\text{area of selected cell} \times \text{mean fluorescence of background readings})$$

First, 8 regions of interest (ROI) were manually selected from the image based on the highest intensity. Using the analysis tool, integrated densities of each ROI were obtained. Next, for the background fluorescence measurement, three neighboring areas were selected and the average value was calculated for each ROI. The same method was applied to all the sequential images at different time points. When CTCF values of all the images were obtained, the values were normalized to the value of $t_0$, which was before the addition of octopamine. Normalized intensities were plotted against time.

# 3. Results

## 3.1. Sensor Design

### 3.1.1. Determination of insertion site

As discussed in section 1.3.4.2, successful design of GPCR-based real-time sensors hinges on the exchange of the third intracellular loop of the GPCR to a cpFP indicator. Choosing the correct insertion site for the fluorescent indicator is considered a critical factor, determining the success of the sensor engineering process (Patriarchi *et al*., 2019). Therefore, the insertion site should be carefully designed based on the identification of transmembrane helices 5 and 6 of the GPCR.

In this project, we constructed sensors for the octopamine receptor OCTR-1 octopamine (Mills *et al*., 2012) and the tyramine receptor TYRA-2a (Rex *et al*., 2005). The prediction of the third intracellular loop was based on the sequence homology of multiple experimentally validated sensors for different GPCRs. For this, the sequences of different GPCR sensors (B1AR; beta-1 adrenergic receptor, B2AR; beta-2 adrenergic receptor, DRD2; dopamine receptor, A2AR; alpha-2 adrenergic receptor, KOR; kappa-type opioid receptor, MOR; opioid receptor μ1, 5HT2A; 5-HT2A receptor, MT2; melatonin receptor type 1B) and existing DA-monitoring dLight series were used to identify the third intracellular loop (Data S1, Patriarchi *et al*., 2018). In addition, the protein sequences of 6 putative octopaminergic/tyraminergic *C. elegans* GPCRs (OCTR-1, TYRA-2a, TYRA-3b, SER-2z, SER-3, SER-6z) were added to this list, after which the homology of all protein sequences was analyzed using Clustal Omega (CO). The proteins were grouped according to their sequence similarity (Figure 14).

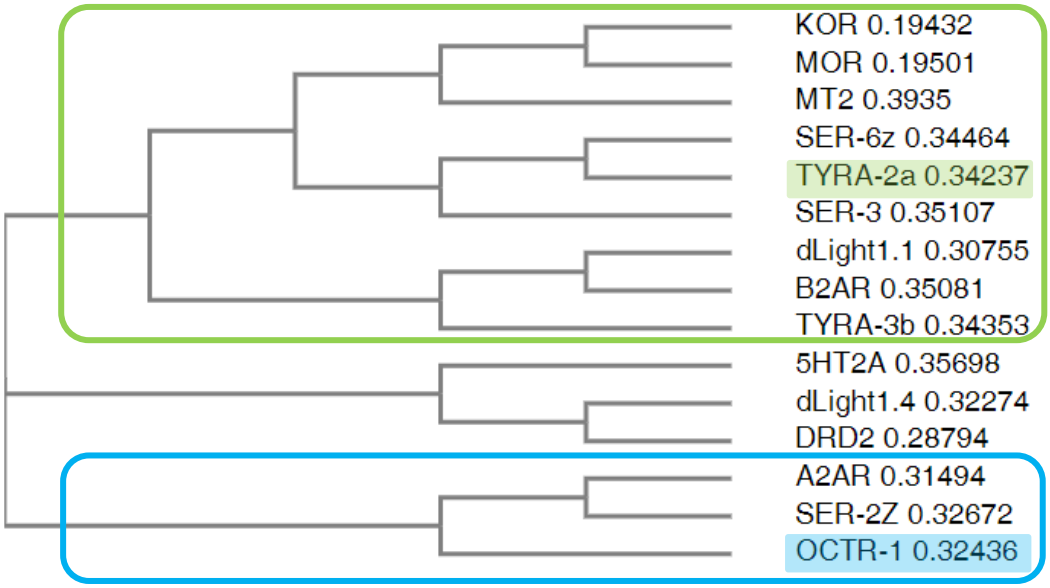


**Figure 14. Clustal Omega (CO) result.** For the identification of the third intracellular loop, amino acid sequences of 6 putative octopaminergic/tyraminergic *C. elegans* GPCRs were aligned with a list of GPCR sensors as reported in Patriarchi *et al*., 2018. A subset of proteins showing sequence homology to OCTR-1 (blue) and TYRA-2a (green) were aligned in groups.

Then, proteins in the subcategory were aligned in groups to estimate approximate location of transmembrane 5 and 6 segment of OCTR-1 and TYRA-2a. As the experimental validation of different GPCR sensors provided preferrable insertion sites, (Data S1, Patriarchi *et al*., 2018), transmembrane domain of OCTR-1 and TYRA-2a were estimated from this data. For example, OCTR-1 sequence was aligned with A2AR and SER-2z in the same subcategory, and ICL3 of OCTR-1 was estimated by comparing this alignment result with the existing transmembrane prediction data of A2AR (Figure 15). Similarly, ICL3 of TYRA-2a was estimated (Figure 16).

```
SER-2Z      MVLRAIDSIRDSVINASSAVSTTTLPPLDIPMTSMKPPSIIPTVELVLGTITYLVIIAMT    60
A2AR        -----MGSLQPDAGNASW---NGTEAPGGG--ARATPYSLQV---TLTLVCLAGLLMLLT    47
OCTR-1      ----------------MW---NLNCSESDT--K-VACLNLGE---AVLTISSMLTVMLLI    35
                                . .    .          .:      :        :: :
SER-2Z      VVGNTLVVVAVFSYRPLKKV-QNYFLVSLAASDLAVAIFVMPLHVVTFLAGGKWLLGVTV    119
A2AR        VFGNVLVIIAVFTSRALKAP-QNLFLVSLASADILVATLVIPFSLA-NEVMGYWYFGKAW    105
OCTR-1      IFGNLLVVVTVYRDRKLRMQRQNWLIVSLAVADMLVGLLVMPLTLT-YEIVGEWTMGNIL    94
            :.** **:::*:  * *:   ** ::**** :*: *. :*:*: :.     * * :*
SER-2Z      CQFFTTADILLCTSSILNLCAIALDRYWAIHNPINYAQKRTTKFVCIVIVIVWILSMLIS    179
A2AR        CEIYLALDVLFCTSSIVHLCAISLDRYWSITQAIEYNLKRTPRRIKAIIITVWVISAVIS    165
OCTR-1      CEIWLALDVLFVTASILHICAISLDRYFSVTSPLTYPATRTPLRMFIYIGVSWIVSLLIC    154
            *::: : *:*: *:**:::***:****::: . : *  .**   :   *   *::* :*.
SER-2Z      VPPIIGWNNWQ----ENMMEDSCGLSTEKAFVVFSAAGSFFLPLLVMVVVYVKIFISARQ    235
A2AR        FPPLISIEKKGGGGGPQPAEPRCEINDQKWYVISSCIGSFFAPCLIMILVYVRIYQIAKR    225
OCTR-1      LPPIFGW-------RPERAEGECSVSTDLGYVLYSSLGSFYIPVVILIIVYAKIYSITIR    207
            .**::.          :  *  * :. :  :*: *. ***: * :::::**.:*:  : :
SER-2Z      RIRTNR-----GRSALMRIQNAEGDDDYRKMSIKRASVESARTSSRVG-EKTPLVIAD--    287
A2AR        RTRVPPSRR--GPDAVA---APPGGTERRPNGLGP-----ERSAGPGGAEAEPLPTQLNG    275
OCTR-1      HSRQRLKETERRDHTLNMLTIRSSTNERYNMEYEL-----EENSDPIEDEKEKVVTN---    259
            : *           ::       .  :              ..:.    *   :
SER-2Z      --GQ--------TTVTTL-------AAHSTDGGSLPKDETTKHMKYHN----------N    319
A2AR        APGEPAPAGPRDTDALDLEESSSSDHAERPPGPRRPERGPRGKGKARASQVKPGDSLRGA    335
OCTR-1      ------------RDMINK---V--CWQLRKISEELPRQGVKIALDT-NHNSPPASDL---    298
                                  .   *.      .
SER-2Z      GSCKVKVKDVKEDEGNPNPTAVLRKREKISVAKEKRAAKTIAVIIFVFSFCWLPFFVAYV    379
A2AR        GRGRRGSGRRLQGRGRSASGLPRRRAGAGGQNREKRFTFVLAVVIGVFVVCWFPFFFTYT    395
OCTR-1      -------TRKLEEKK-----FC-EKRKRKLKAKERQATLLLGIILSAFILSWLPFFLIYV    345
                  : .       .:       :*:: :  :.::: .* ..*:***. *.
SER-2Z      IRPFCETCKLHAKVEQAFTWLGYINSSLNPFLYGILNLEFRRAFKKILCPKAVLEQRRRR    439
A2AR        LTAVG--CSVPRTLFKFFFWFGYCNSSLNPVIYTIFNHDFRRAFKKILCRGDRKRIV---    450
OCTR-1      IGAFG--HEAPPLVFKFFFWLGYCNSGINPVIYTVFNREFKRGLCKQLHKFERFIHPLME    403
            :  .    .    : : * *:** **.:**.:* ::* :*:*.: * *
SER-2Z      MSAQP         444
A2AR        -----         450
OCTR-1      FYK--         406
```

**Predicted ICL3 for OCTR-1**

MWNLNCSESDTKVACLNLGEAVLTISSMLTVMLLIIFGNLLVVVTVYRDRKLRMQRQNWLIVSLAVADMLVGLLVMPLTL
TYEIVGEWTMGNILCEIWLALDVLFVTASILHICAISLDRYFSVTSPLTYPATRTPLRMFIYIGVSWIVSLLICLPPIFG
WRPERAEGECSVSTDLGYVLYSSLGSFYIPVVILIIVYAKIYSITIRHSRQRLKETERRDHTLNMLTIRSSTNERYNMEY
ELEENSDPIEDEKEKVVTNRDMINKVCWQLRKISEELPRQGVKIALDTNHNSPPASDLTRKLEEKKFCEKRKRKLKAKER
QATLLLGIILSAFILSWLPFFLIYVIGAFGHEAPPLVFKFFFWLGYCNSGINPVIYTVFNREFKRGLCKQLHKFERFIHP
LMEFYK

**Figure 15. Prediction of OCTR-1 intracellular loop 3 (ICL3) based on sequence alignment.** The sequence of OCTR-1 was aligned with SER-2z and A2AR to estimate ICL3 of OCTR-1. Asterisk (*) indicates residues with fully conserved properties, colon (:) indicates residues with strongly similar properties, and period (.) indicates residues with weakly similar properties. The prediction data for TM 5 (orange) and TM 6 (purple) of A2AR were retrieved from the supplementary Data 1, Patriarchi *et al*., 2018, and ICL3 of OCTR-1 (highlighted) was estimated by comparing its sequence with this data.

```
KOR             VIECSLQFPDDDYSWWDLFMKICVFIFAFVIPVLIIIVCYTLMILRLK----S-------  255
MOR             SIDCTLTFSHPTW-YWENLLKICVFIFAFIMPVLIITVCYGLMILRLK----S-------  325
MT2             PRIYSCTFIQTAS----TQYTAAVVVIHFLLPIAVVSFCYLRIWVLVLQARRKAKP----  236
dLight1.1       ETIDNCDSS--LS----RTYAISSSVISFYIPVAIMIVTYTRIYRIAQKQIRRIAALER-  233
B2AR            AEETCCDFF--TN----QAYAIASSIVSFYVPLVIMVFVYSRVFQEAKRQLNIFEMLRID  239
TYRA-3b         SEDFKCAYS--PS----VAYRIYSALGSFYLPLLVMLFVYFKIFRVASEREALMR--QSV  305
SER-3           ETPCRCTPAN-AG----RVYVVFSASSSFYIPMIIVVFVYFRIYVAARAATKS-IYSGMM  258
TYRA-2a         NTVRQCTFLD-LP----S-YTVYSATGSFFIPTLLMFFVYFKIYQAFAKHRARQIYRQK-  224
SER-6z          EPTKDCQPTS-LP----SMYIIFSAMASFIVPAFVMVILNVRIFQTVLHTSRTMTVKSK-  201
                                        * :*  :: .    :

                                    (Omitted)

KOR             -------------------LS---------------------------GSREKD--RNLR  270
MOR             -------------------LS---------------------------GSKEKD--RNLR  340
MT2             -------------------LCLK-------------------------------PSDL  247
dLight1.1       PV-----------------ECSQ---P--------------------ESSFKMSFKRET  268
B2AR            --------DEAAVNLAKSRWYNQTP---NRAKRVITT-FRTG------TWDAYKFCLKEH  397
TYRA-3b         PVRKNTEVGVAPSLSKRARQCNARLQPNNLLQKAHEHYQINGPGKAVRGSKEKMVYMRER  491
SER-3           SMSNNNNNGDEKEAFDESLLSES-KKKSKSLASKFNHLMRRGQKKRTAGAYE-KRLSLEI  482
TYRA-2a         PM---------RSVMA--ISYEKVKRHKNRKERIYRKSLQRK-------PKA-ISAAKER  377
SER-6z          AI---------RSFLTHTVVFGVL---EAKKTNIINHITQKK-------CMR-RSLRTEI  303


KOR             RITRLVLVVVAVFVVCWTPIHIFILVEALGSTSHST---AALSSYYFCIALGYTNSSLNP  327
MOR             RITRMVLVVVAVFIVCWTPIHIYVIIKALVTIPETT---FQTVSWHFCIALGYTNSCLNP  397
MT2             RSFLTMFVVFVIFAICWAPLNCIGLAVAI--NPQEMAPQIPEGLFVTSYLLAYFNSCLNA  305
dLight1.1       KVLKTLSVIMGVFVCCWLPFFILNCILPFCGSGETQPFCIDSNTFDVFVWFGWANSSLNP  328
B2AR            KALKTLGIIMGTFTLCWLPFFIVNIVH---------------------------------  424
TYRA-3b         KALKTIGIVVLGFIICWMPFFIMYLVEVFISDPVAESP-IYRITSEFFLWLGYSNSVLNP  550
SER-3           KAAKTVAIVTGCFIFCWLGFALVYGLEIK----------LNDVVWSIVFWLGYLNSALNP  532
TYRA-2a         RGVKVLGIILGCFTVCWAPFFTMYVLVQFC-----KDCSPNAHIEMFITWLGYSNSAMNP  432
SER-6z          RVARTTGIVVAAFIVCWIPFTTIYVLQAYAVCTVAAGCIPAS-LFTTAFWLGYSNSAVNP  362
                :      ::   *  **  :
```

**Predicted ICL3 for TYRA-2a**

MMSSYVMSPVDETYTLFQILKGSALFLLVLWTIFANSLVFIVLYKNPRLQTVPNLLVGNLAFSDLALGLIVLPLSSVYAI
AGEWVFPDALCEVFVSADILCSTASIWNLSIVGLDRYWAITSPVAYMSKRNKRTAGIMILSVWISSALISLAPLLGWKQT
AQTPNLIYEKNNTVRQCTFLDLPSYTVYSATGSFFIPTLLMFFVYFKIYQAFAKHRARQIYRQKVIRKHIESTILHEISH
VLPTSDEFAKEEEEEEDSESSGQVENGLGNGNDAIIEEDECEDEDSDEKRDDHTSMTTVTATVTGPTEAPYMKREAKISK
SVPIEKESAIQKREAKPMRSVMAISYEKVKRHKNRKERIYRKSLQRKPKAISAAKERRGVKVLGIILGCFTVCWAPFFTM
YVLVQFCKDCSPNAHIEMFITWLGYSNSAMNPIIYTVFNRDYQIALKRLFTSEKKPSSTSRV

**Figure 16. Prediction of TYRA-2a intracellular loop 3 (ICL3) based on sequence alignment.** The sequence of TYRA-2a were aligned with KOR, MOR, MT2, dLight 1.1, SER-3b, SER-6z and TYRA-3b to estimate ICL3 of TYRA-2a. Asterisk (*) indicates residues with fully conserved properties, colon (:) indicates residues with strongly similar properties, and period (.) indicates residues with weakly similar properties. The prediction data for TM 5 (orange) and TM 6 (purple) of KOR, MOR, MT2, dLight1.1, B2AR were retrieved from the supplementary data 1 of Patriarchi *et al*., 2018, and ICL3 of TYRA-2a (highlighted) was estimated by comparing its sequence with this data. Due to page limitation, only the most relevant sequences showing the end of TM5 and the start of TM6 are presented here. The full result of sequence alignment can be found in appendix.

### 3.1.2. Linker design based on the literature

The linker regions that connect the cpFP with the GPCR protein are critical to the proper functioning of the sensor (Patriarchi *et al*., 2019). Therefore, this project set out to test different linker variants on each side of the cpFP for their performance. These linkers consist of a fixed set of residues fused to the GPCR, and a variable amino acid stretch flanking each terminal of the fluorescent indicator cpmApple. LLS- (N terminal) and -DDL (C terminal) sequences were used as fixed linker sequences as they were previously successfully implemented in the red RdLight sensor on which the sensors in this project are based (Patriarchi *et al*., 2020).

Similarly, the variable residues to connect the fixed linker stretch to the cpmApple indicator were adapted from already existing sensors (Table 6), with some modifications. While a varying number of amino acids was used for the variable linkers in the original sensors (Feng *et al*., 2019; Patriarchi *et al*., 2018, 2020; Wan *et al*., 2021), only two amino acids directly flanking the cpmApple were adopted for our variants. Also, variant 5 was designed to have a single glycine (G) residue for a variable linker, while variant 6 has the fixed LSS/DDL amino acid linkers to directly connect to the fluorescent protein. This way, the effect of the total length of the linkers on sensor performance can be examined.

**Table 6. Linker sequences for different sensor variants.**

| Variant | Original sensor motif | Sensor cassette amino acid sequence | Reference |
|---|---|---|---|
| 1 | RdLight1 | **LSS**-FH-cpmApple-RK-**DDL** | Patriarchi *et al*., 2020 |
| 2 | dLight1.1 | **LSS**-LI-cpmApple-NH-**DDL** | Patriarchi *et al*., 2018 |
| 3 | $GRAB_{5\text{-}HT}$ | **LLS**-NG-cpmApple-GF-**DDL** | Wan *et al*., 2021 |
| 4 | $GRAB_{NE}$ | **LLS**-GG-cpmApple-GG-**DDL** | Feng *et al*., 2019 |
| 5 | - | **LLS**-G-cpmApple-G-**DDL** | 1 amino acid (G) |
| 6 | - | **LLS**-cpmApple-**DDL** | No linker |

### 3.1.3. Codon-optimization

All the amino acid sequences for synthesis of the cpmApple (gBlock) and linker fragments were codon-optimized for *C. elegans* using the online ExpOptimizer tool (www.novoprolabs.com/tools/codon-optimization). Organisms are known to prefer particular codons over others for translating the same amino acids, which is referred to as ‘codon usage bias’ (Komar, 2016). While the exact mechanistic basis of this process remains unclear, this difference in the usage frequency of synonymous codons may affect gene expression efficiency. Therefore, it is necessary for efficient gene expression in *C. elegans*.

## 3.2. Molecular cloning

Using various molecular cloning techniques, each component was prepared separately and assembled together to generate a series of sensor constructs. DNA sequences encoding OCTR-1 and TYRA-2a were obtained by amplifying the cDNA sequences of these receptor-encoding genes from plasmids that were already available in the host lab. Next, the cpmApple fluorescent protein with varying linkers was attached to the receptor cDNAs to obtain 6 different sensor variants. Each sensor construct was first generated in a KSM expression backbone using Gibson Assembly. Then, sensor constructs were subcloned into a pcDNA3.1 vector for expression in mammalian HEK293 cells that allowed to further characterize the sensor response *in vitro*.

### 3.2.1. Linearization of the receptor backbone

OCTR-1 and TYRA-2a cDNA sequences were provided in the KSM vector by the Schafer lab (MRC Laboratory of Molecular Biology, Cambridge, UK). The KSM vector is an oocyte expression vector that is often used for functional analyses of foreign mRNAs and translated proteins. It contains a multiple cloning site (MCS) surrounded by 5' and 3' untranslated regions for *Xenopus* β-globin (Virkki *et al*., 2002).

As a first step, these vectors were linearized using PCR with the high-fidelity Q5 polymerase. This reaction amplified the entire sequence of the vector, excluding the putative ICL3 stretch of the GPCR. For this, the forward primer was designed to anneal at the beginning of transmembrane stretch 6 of the GPCR and contained a DDL fixed linker as overhang. Conversely, the reverse primer anneals at the end of transmembrane stretch 5 of the GPCR and contains an LLS fixed linker as overhang.

**Table 7. Primers for linearization of the *octr-1* and *tyra-2a* plasmids.** Primers include fixed linkers which are indicated in bold. Transmembrane stretches of the receptors are indicated in colors.

| GPCR | Primer | Oligonucleotide sequence | 3'Tm | 3'Ta | Amplicon |
|---|---|---|---|---|---|
| OCTR-1 | PJW194 (forward) | **gatgattta**AAAGAACGACAGGCTACTTTGTTG | 65°C | 66°C | 3980 bp |
| | PJW195 (reverse) | **gctactaag**TTCTGCCCTTTCCGGTCGCCATCCG | 78°C | | |
| TYRA-2a | PJW212 (forward) | **gatgattta**AAAGAAAGACGTGGAGTCAAAGTAC | 67°C | 68°C | 4118 bp |
| | PJW213 (reverse) | **gctactaag**TTTTGCAAACGCTTGATAGATT | 67°C | | |

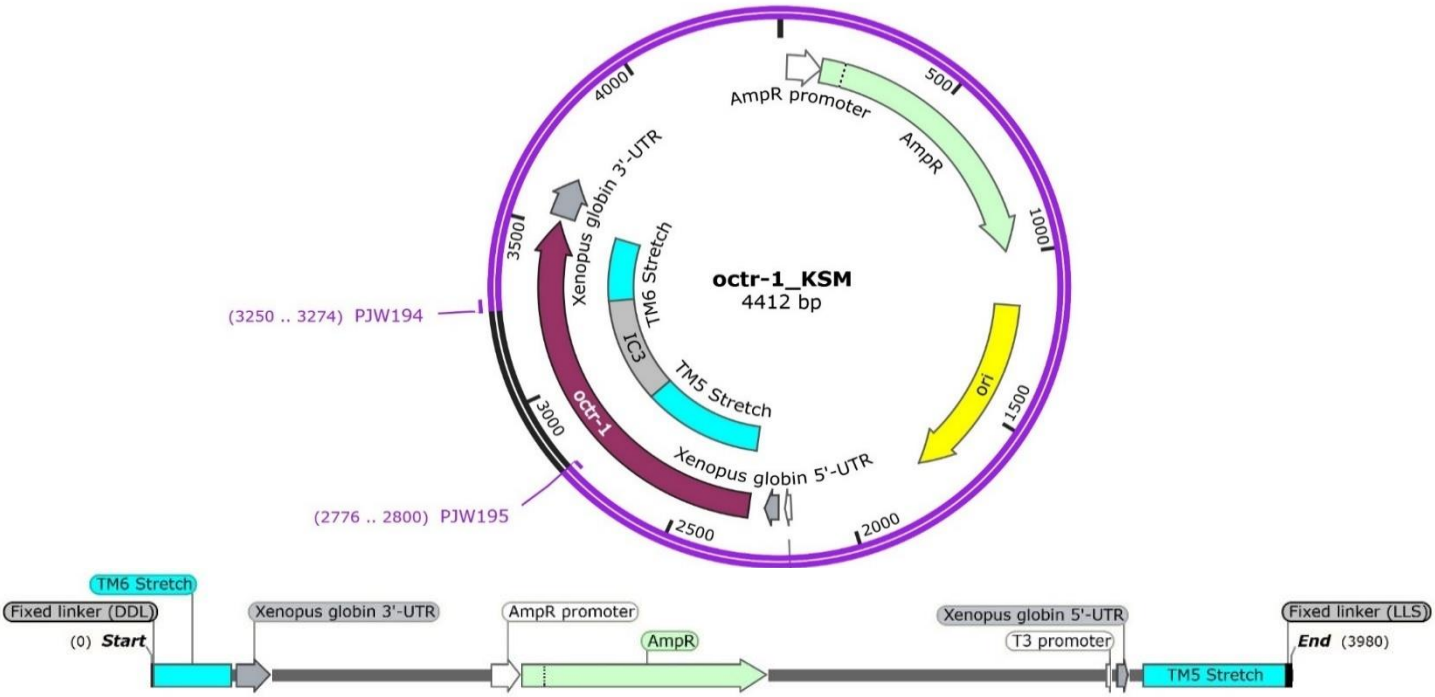


**Figure 17. Plasmid map of *octr-1* in KSM vector (top) and the amplicon for the *octr-1* sensor backbone (bottom).** Primer PJW194 and PJW195 (including fixed linker sequences) anneal next to the predicted third intracellular loop of OCTR-1 and amplify the rest of the vector as indicated in purple.

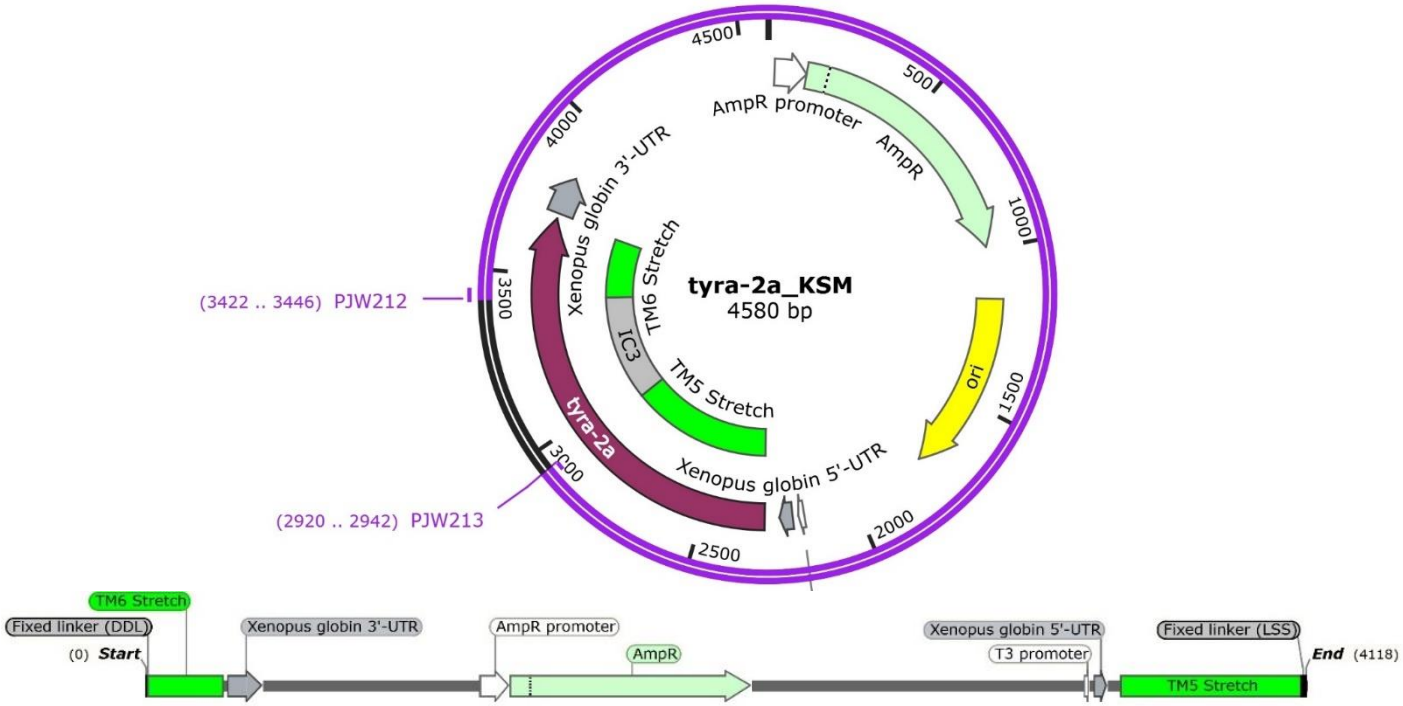


**Figure 18. Plasmid map of *tyra-2a* in KSM vector (top) and the amplicon for the *tyra-2a* sensor backbone (bottom).** Primer PJW212 and PJW213 (including fixed linker sequences) anneal next to the predicted third intracellular loop of TYRA-2a and amplify the rest of the vector as indicated in purple.

PCR amplicons were analyzed using gel electrophoresis to verify the correct size with a 1 kb plus ladder. The amplicons for the linearized *octr-1* and *tyra-2a* constructs were expected to be 3980 bp and 4118 bp, respectively. After amplification, positive bands were observed around 4000 bp (Figure 19). This confirmed the presence of the correct size of linearized *octr-1* and *tyra-2a* backbones. The corresponding bands were excised and purified for Gibson Assembly.

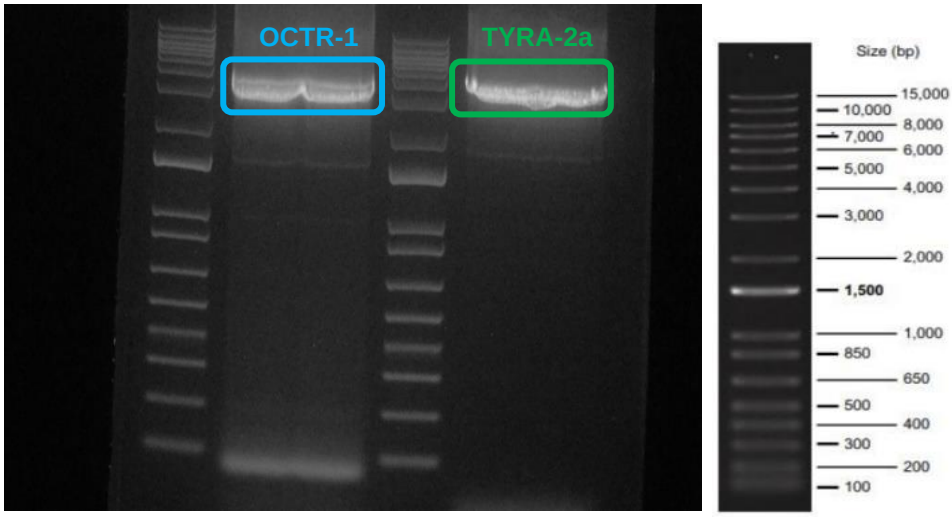


**Figure 19. Gel electrophoresis of linearized *octr-1* and *tyra-2a* backbone.** On the right, a 1 kb plus ladder is shown, and both bands are located around 4000 bp.

### 3.2.2. Preparation of cpmApple insert

#### 3.2.2.1 TOPO TA cloning and mutagenesis of cpmApple

A *C. elegans* codon-optimized DNA sequence encoding the cpmApple fluorescent protein was synthetized as gBlock at Integrated DNA Technologies (IDT, Leuven, Belgium). This synthetic fragment also included random nucleotides flanking both ends of the cpmApple sequence for efficient insertion into a pCR™4-TOPO™ backbone, and – if necessary – efficient PCR amplification of the linear synthesized fragment. Insertion into a backbone is necessary for the convenient amplification of cpmApple with overlap primers to attach different linkers, and for long-term storage as bacterial freeze stock. After direct insertion of the gBlock into the pCR™4-TOPO™ backbone, transformed bacterial colonies were lysed and sequenced to confirm the correct insertion. Unexpectedly, a single T to C mutation was identified within the gBlock sequence (Figure 20), which appeared to be a mutation in the gBlock fragment itself. When translated, this single nucleotide substitution within the open reading frame resulted in a leucin (L) to phenylalanine (F) missense mutation. As the biochemical properties of aromatic phenylalanine significantly differ from aliphatic leucin, it is likely to affect the fluorescent properties of cpmApple. Therefore, site-directed mutagenesis was conducted to correct this mutation. Subsequently, the C to T nucleotide substitution was successfully verified by sequencing with the PJW241 primer, spanning the mutagenesis target region.

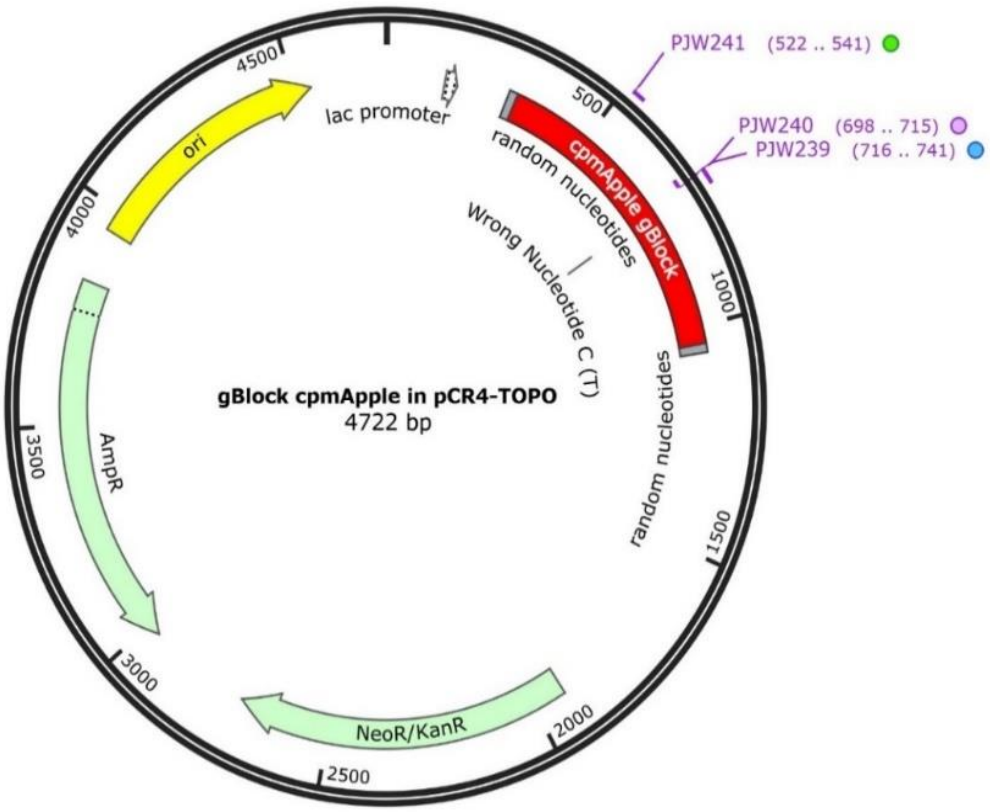


**Figure 20. Insertion and site-directed mutagenesis of a codon-optimized cpmApple gBlock fragment into the pCR™4-TOPO™ backbone.** An unexpected single T to C nucleotide mutation was observed in the gBlock sequence synthesized for cpmApple. Therefore, site-directed mutagenesis was conducted using PJW239 and PJW240. PJW241 was used to validate the successful substitution.

**Table 8. Primers for site-directed mutagenesis.** The annealing sites of each primer can be found on the plasmid map above using the color code.

| Primer | Oligonucleotide sequence | 3'Tm | 3'Ta | Amplicon |
|---|---|---|---|---|
| PJW239 (forward) | ATACGAGGCATTTCAGACTGCTAAGC | 67°C | 68°C | 4722 kb |
| PJW240 (reverse) | GGACGACCCTCGCCTTCA | 70°C | | |
| PJW241 | GAAAGAGCGGAAGGACGACA | | | |

### 3.2.2.2 Annealing variable linkers to cpmApple

Once a correct cpmApple-coding sequence was cloned, the fragment was amplified and appropriate linkers annealed using Q5 PCR. Primers were designed to anneal at both ends of the cpmApple sequence (Figure 21), and included an overhang sequence of variable linker residues, fixed linker residues and also the region spanning each end of the linearized GPCR construct (Table 9). For Gibson assembly, inserts and backbones must overlap around 20-40 bp in sequence. Therefore, short stretches of the GPCR sequence need to be added along with the fixed linkers to obtain this overlap. The sensor variants differ only in the variable linker region, as is shown in Table 9.

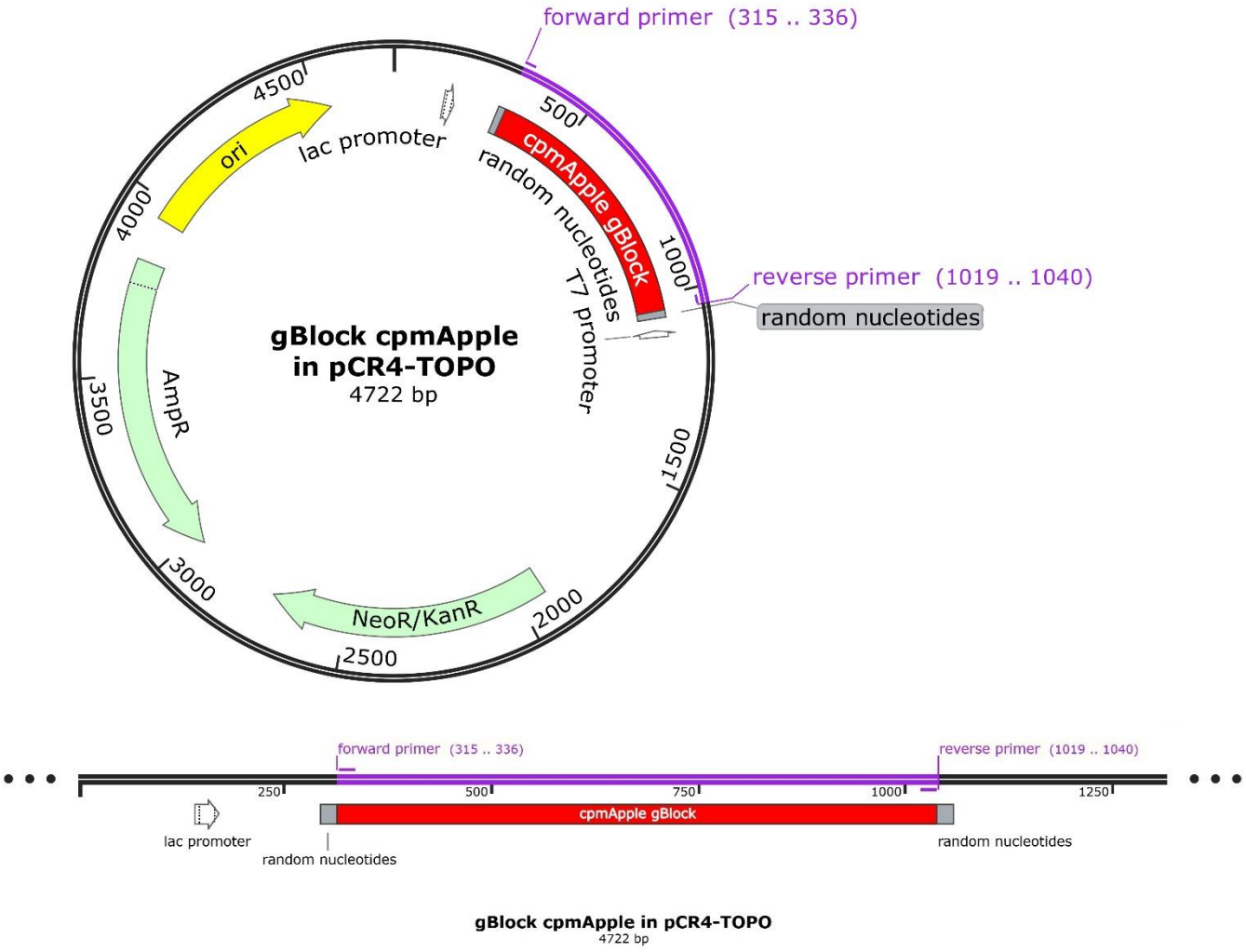


**Figure 21. A plasmid map showing primer annealing sites for linker annealing to cpmApple (top) and close-up view (bottom).** For 6 sensor variants, each insert is prepared by using a different forward/ reverse primer pair with overhangs that generate different variable linker sequences. Primers anneal at both ends of cpmApple, and amplify the region indicated in purple. A detailed amplicon construct is shown in Figure 22.

**Table 9. Primers for annealing linkers to cpmApple.** Each primer anneals to the cpmApple seqeuence (red) and contains an overhang sequence of variable linker residues (gray), fixed linker residues (bold) and the region spanning each end of the linearized GPCR construct (OCTR-1: green/ TYRA-2a: blue).

| Insert | | Primer | Oligonucleotide Sequence | Amplicon |
|---|---|---|---|---|
| OCTR-1 | 1 | PJW196 (forward) | aaagggcagaa**cttagtagc**tttcacGTGAGTGAACGTATGTATCCGG | 778bp |
| | | PJW197 (reverse) | tgtcgttctttt**aaatcatc**ttttcgTGCCTCCCATCCCATTGTTTTC | |
| | 2 | PJW198 (forward) | aaagggcagaa**cttagtagc**ctcattGTGAGTGAACGTATGTATCCGG | |
| | | PJW199 (reverse) | tgtcgttctt**ttaaatcatc**atgattTGCCTCCCATCCCATTGTTTTC | |
| | 3 | PJW200 (forward) | aaagggcagaa**cttagtagc**aatggtGTGAGTGAACGTATGTATCCGG | |
| | | PJW201 (reverse) | tgtcgttctttt**aaatcatc**aaaaccTGCCTCCCATCCCATTGTTTTC | |
| | 4 | PJW202 (forward) | aaagggcagaa**cttagtagc**ggcggtGTGAGTGAACGTATGTATCCGG | |
| | | PJW203 (reverse) | tgtcgttctttt**aaatcatc**gccaccTGCCTCCCATCCCATTGTTTTC | |
| | 5 | PJW204 (forward) | aaagggcagaa**cttagtagc**ggcGTGAGTGAACGTATGTATCCGG | 772bp |
| | | PJW205 (reverse) | tgtcgttctttt**aaatcatc**accTGCCTCCCATCCCATTGTTTTC | |
| | 6 | PJW206 (forward) | aaagggcagaa**cttagtagc**GTGAGTGAACGTATGTATCCGG | 766bp |
| | | PJW207 (reverse) | tgtcgttctttt**aaatcatc**TGCCTCCCATCCCATTGTTTTC | |
| TYRA-2a | 1 | PJW214 (forward) | cgtttgcaaaa**cttagtagc**tttcacGTGAGTGAACGTATGTATCCGG | 778bp |
| | | PJW215 (reverse) | cgtctttctttt**aaatcatc**ttttcgTGCCTCCCATCCCATTGTTTTC | |
| | 2 | PJW216 (forward) | cgtttgcaaaa**cttagtagc**ctcattGTGAGTGAACGTATGTATCCGG | |
| | | PJW217 (reverse) | cgtctttctttt**aaatcatc**atgattTGCCTCCCATCCCATTGTTTTC | |
| | 3 | PJW218 (forward) | cgtttgcaaaa**cttagtagc**aatggtGTGAGTGAACGTATGTATCCGG | |
| | | PJW219 (reverse) | cgtctttctttt**aaatcatc**aaaaccTGCCTCCCATCCCATTGTTTTC | |
| | 4 | PJW220 (forward) | cgtttgcaaaa**cttagtagc**ggcggtGTGAGTGAACGTATGTATCCGG | |
| | | PJW221 (reverse) | cgtctttctttt**aaatcatc**gccaccTGCCTCCCATCCCATTGTTTTC | |
| | 5 | PJW222 (forward) | cgtttgcaaaa**cttagtagc**ggcGTGAGTGAACGTATGTATCCGG | 772bp |
| | | PJW223 (reverse) | cgtctttctttt**aaatcatc**accTGCCTCCCATCCCATTGTTTTC | |
| | 6 | PJW224 (forward) | cgtttgcaaaa**cttagtagc**GTGAGTGAACGTATGTATCCGG | 766bp |
| | | PJW226 (reverse) | cgtctttctttt**aaatcatc**TGCCTCCCATCCCATTGTTTTC | |

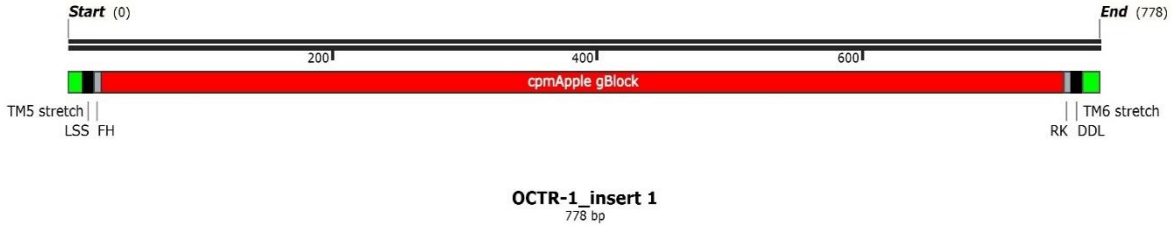


**Figure 22. Overview of insert 1 for the OCTR-1 sensor, containing an LSS-FH-cpmApple-RK-DDL cassette flanked by sequences overlapping with the *octr-1* cDNA sequence.**

A schematic image of variant 1 of the OCTR-1 sensor is shown above (Figure 22). Upon successful amplification, the fragment to be inserted into the *octr-1* cDNA sequence consists of the cpmApple coding sequence, fixed and variable linker residues spanning the fluorescent protein sequence, and a short stretch of 11 bp overlapping with *the octr-1* cDNA sequence. After the PCR, gel electrophoresis was conducted to confirm the amplification of the inserts. All the amplicons showed a positive band around 800 bp, which matched the expected size of the amplicons (Figure 23).

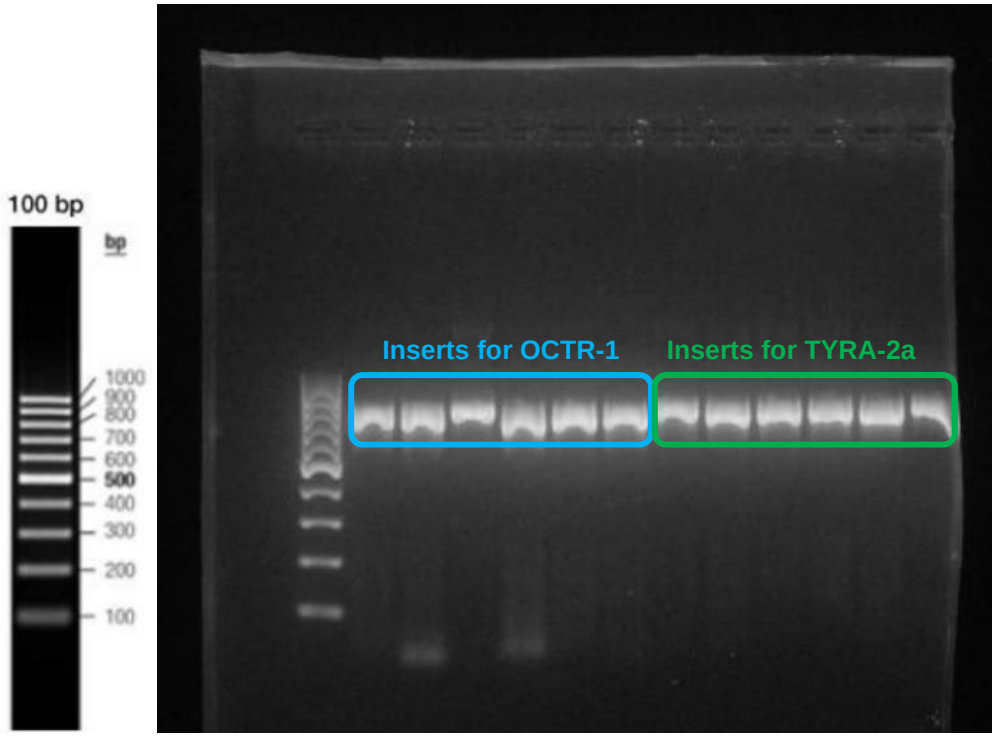


**Figure 23. Gel electrophoresis of cpmApple inserts for OCTR-1 (left) and TYRA-2a (right) sensors.** On the left, a 100 bp DNA ladder is shown, confirming the correct amplification of all the inserts with a size around 800 bp.

### 3.2.3. Gibson assembly into KSM backbone

When all inserts and the linearized GPCR backbones were prepared, Gibson Assembly was set up to assemble the two linear components into a circular plasmid by joining overlapping sequences at both ends (Figure 24).

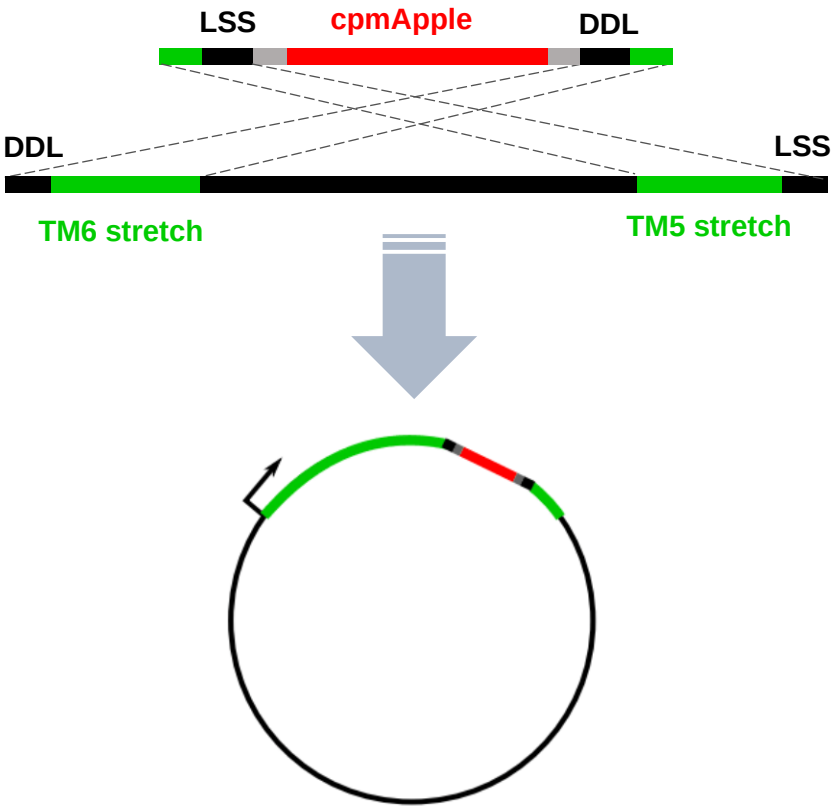


**Figure 24. Gibson Assembly of receptor and cpmApple DNA fragments.** Prepared inserts and GPCR backbones are joined by overlapping sequences at both ends, as guided by dashed lines. As a result, two linear fragments are assembled into a complete sensor construct in a circular plasmid.

Gibson Assembly products were transformed into DH5α cells, after which colony PCR was conducted to identify colonies with the correct plasmid. For this, a PCR was done using poison primers, which facilitate detection of insertion events in the correct orientation, as one primer anneals to the insert while the other binds to the backbone. Traditionally, poison primers are used to screen small deletions in *C. elegans*, where they are named poison due to their interference on the production of a full-length wild-type fragment (Edgley, 2002).

In our experiments, poison primers were used to easily identify the correct assembly of different sensor variants. They were designed to amplify a region spanning cpmApple and transmembrane sequences so that a correct size of amplicons indicates a proper assembly of the construct. Also, the poison primers could be universally used regardless of different inserts as they were non-specific to the variable linker residues. For each receptor types, two sets of poison primers were designed targeting different parts of the sensor construct in case one fails (Figure 25, Figure 27).

### 3.2.3.1 OCTR-1 sensor

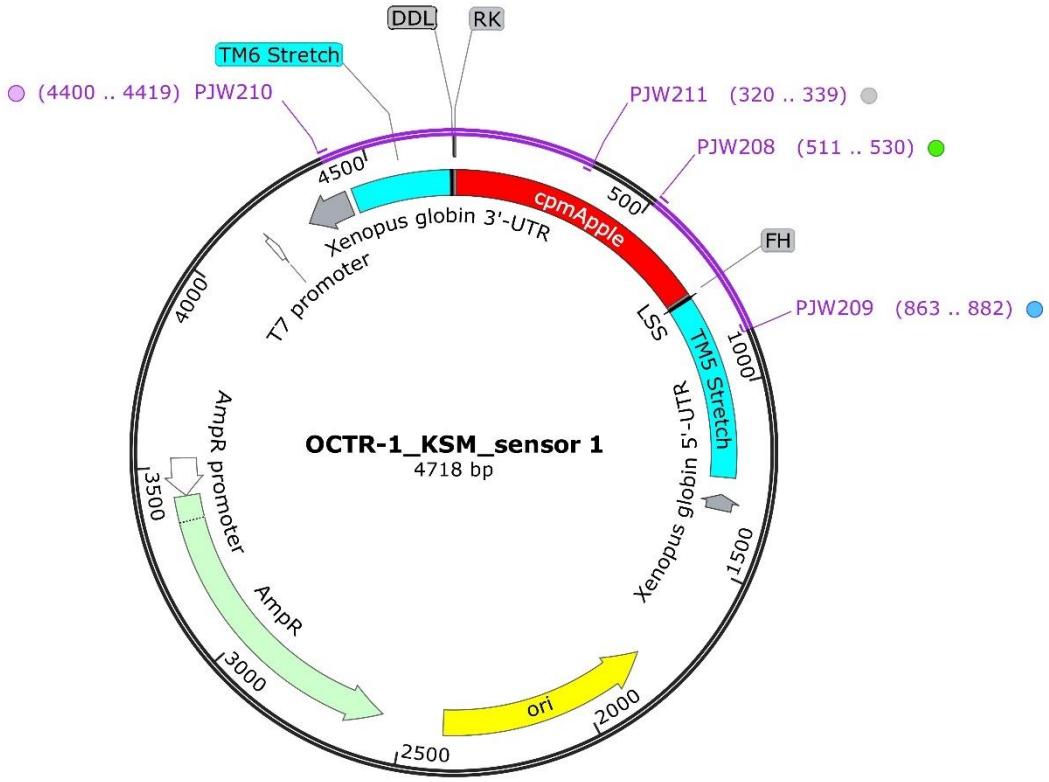


**Figure 25. Plasmid map of OCTR-1 sensor variant 1 in KSM backbone.** Completed sensor constructs were checked by colony PCR. This figure shows the primer binding sites for colony PCR. Poison set 1 was designed to amplify the region spanning cpmApple toward TM5 using PJW208 and PJW 209, whereas poison set 2 was designed toward TM6 using PJW210 and PJW211. Corresponding amplicons are indicated in purple.

**Table 10. Poison primers for colony PCR of OCTR-1 sensor variants.** The annealing sites of each primer can be found on the plasmid map above using the color code.

| Poison Set | Primer | Oligonucleotide sequence | 3'Tm | 3'Ta | Amplicon |
|---|---|---|---|---|---|
| 1 | PJW208 (forward) | TCCTTCCGCTCTTTCGCATT | 60°C | 55°C | 372 bp |
| | PJW209 (reverse) | TCGGTAACTTCGCCACTCAC | 60°C | | |
| 2 | PJW210 (forward) | TTCGGGTGTTCTTGAGGCTG | 60°C | 55°C | 658 bp |
| | PJW211 (reverse) | GGTCGTCCATACGAGGCATT | 60°C | | |

For the 6 OCTR-1 sensor variants, PJW208 and PJW209 primers that amplify a portion of cpmApple and the TM5-encoding sequence of OCTR-1 were used (Figure 25). The resultant amplicons were of the correct size after running them on an agarose gel, preliminarily confirming successful Gibson Assembly (Figure 26). After several rounds of colony PCR, at least one colony with positive bands was harvested for each sensor. Plasmids of corresponding single colonies were purified and sequenced. From the sequencing results, all 6 OCTR-1 KSM sensor constructs were confirmed to be correct and completed sensors in KSM backbones were stored as plasmid stocks and bacterial glycerol stocks.

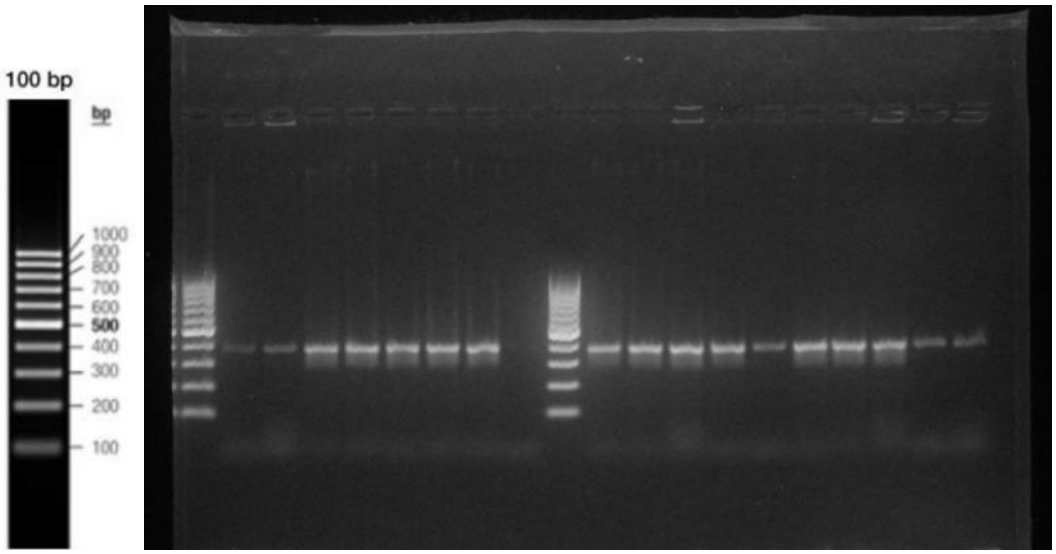


**Figure 26. Gel electrophoresis for colony PCR of OCTR-1 sensors in KSM backbone.** On the left, a 100 bp DNA ladder is shown, confirming the correct size of amplicons around 400 bp.

### 3.2.3.2. TYRA-2a sensor

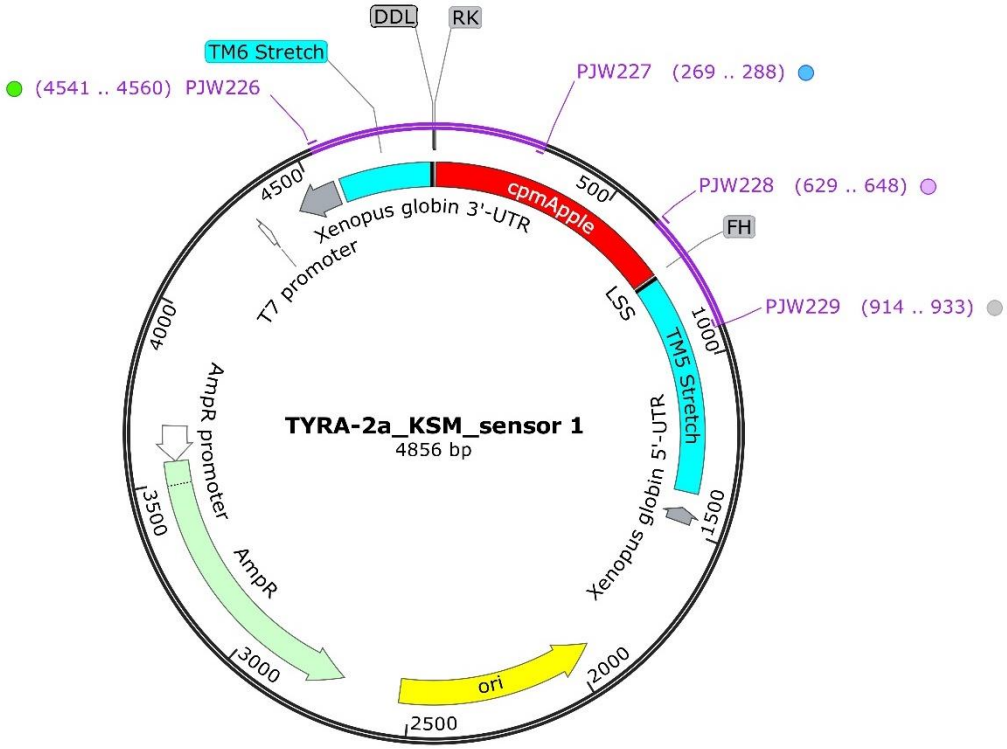


**Figure 27. Plasmid map of TYRA-2a sensor variant 1 in KSM backbone.** Completed sensor constructs were checked by colony PCR. This figure shows the primer binding sites for colony PCR. Poison set 1 was designed to amplify the region spanning cpmApple toward TM6 using PJW226 and PJW 227, whereas poison set 2 was designed toward TM5 using PJW228 and PJW229. Corresponding amplicons are indicated in purple.

**Table 11. Primers for colony PCR of TYRA-2a sensor variants.** The annealing sites of each primer can be found on the plasmid map above using the color code.

| Poison Set | Primer | Oligonucleotide sequence | 3'Tm | 3'Ta | Amplicon |
|---|---|---|---|---|---|
| 1 | PJW226 (forward) | TTCGGGTGTTCTTGAGGCTG | 60°C | 55°C | 604 bp |
| | PJW227 (reverse) | GGTCCATTGCCTTTCGCTTG | 60°C | | |
| 2 | PJW228 (forward) | GTTGTCTTAACTTCCGCCGC | 59°C | 55°C | 305 bp |
| | PJW229 (reverse) | CCACTTCTCGGCTGGAAACA | 60°C | | |

Gibson Assembly of TYRA-2a sensors was carried out in parallel with the construction of OCTR-1 sensor variants. After transformation, many single colonies were observed and colony PCR was conducted with PJW226 and PJW227 (poison primer set 1). However, there was no positive band identified from the gel electrophoresis for any of the TYRA-2a sensors. Therefore, PJW228 and PJW229 (poison primer set 2) were used as an alternative.

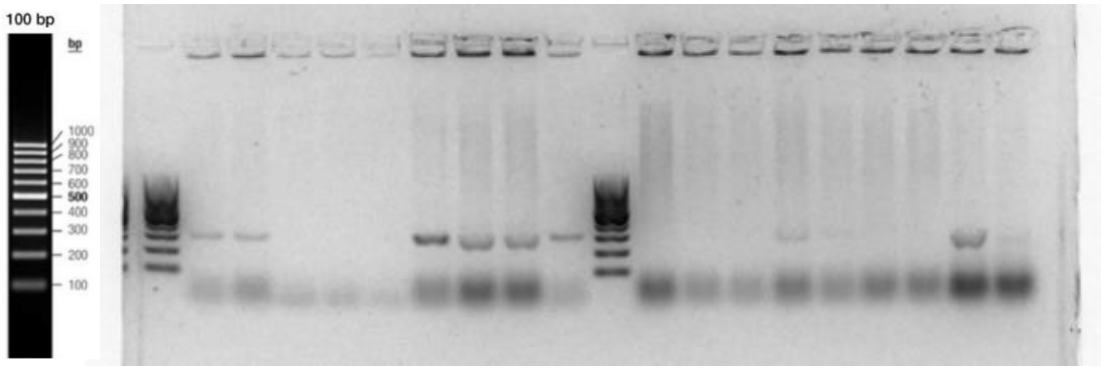


**Figure 28. Gel electrophoresis of colony PCR for TYRA-2a sensors.** The image was obtained in inversed mode for higher contrast as the bands were too weak to be imaged in normal setting. On the left, a 100 bp DNA ladder is shown, confirming the correct size of amplicons around 300 bp.

With the new set of primers, amplicons of around 300 bp in length were observed. However, the corresponding colonies failed to grow when inoculated in the liquid LB medium containing the identical amount of ampicilin as the LB plates. The experiments were repeated under the same condition, but resulted in fewer and weaker positive bands in the course of a dozen repeated colony PCRs (Figure 28). When sequenced with the PJW229 primer, none of the samples yielded good quality sequencing data, even though the concentration of the DNA was verified to be sufficiently high for Sanger sequencing. Next, the samples were sequenced with a T7 promoter primer, which anneals after the TYRA-2a TM6 region and reads toward the cpmApple sequence. This time, the sequencing itself was successful. However, the result revealed that cpmApple was still flanked by random nucleotides that were added to both termini of the coding sequence for the insertion into the pCR™4-TOPO™ Vector as discussed in 3.2.2.1. This suggests that the vector template for amplification of the different sensor variant inserts may have contaminated the Gibson Assembly reaction.

In order to remove the cpmApple-pCR™4-TOPO™ Vector, Gibson Assembly products were digested with the restriction enzyme PaeI (SphI). As the digestion site of PaeI only exists in the pCR™4-TOPO™ Vector, this is intended to selectively remove contaminating TOPO vectors. Digested products were again transformed, and resultant colonies screened with colony PCR, but no suitable poison products were detected. Eventually, the generation of 6 different TYRA-2a sensor variants was aborted at the Gibson Assembly stage due to the strict time constraints of this project.

### 3.2.4. Directional TOPO cloning into pcDNA3.1

The OCTR-1 sensors were subcloned from the KSM vector into a pcDNA3.1 backbone for HEK293 mammalian cell expression. For directional TOPO cloning, a pair of primers were designed to amplify the entire sensor construct (Figure 29). To note, a forward primer was designed to contain the CACC sequence at its 5'end to ensure the directionality of the insertion and an enhanced expression in mammalian cells (see 2.1.6).

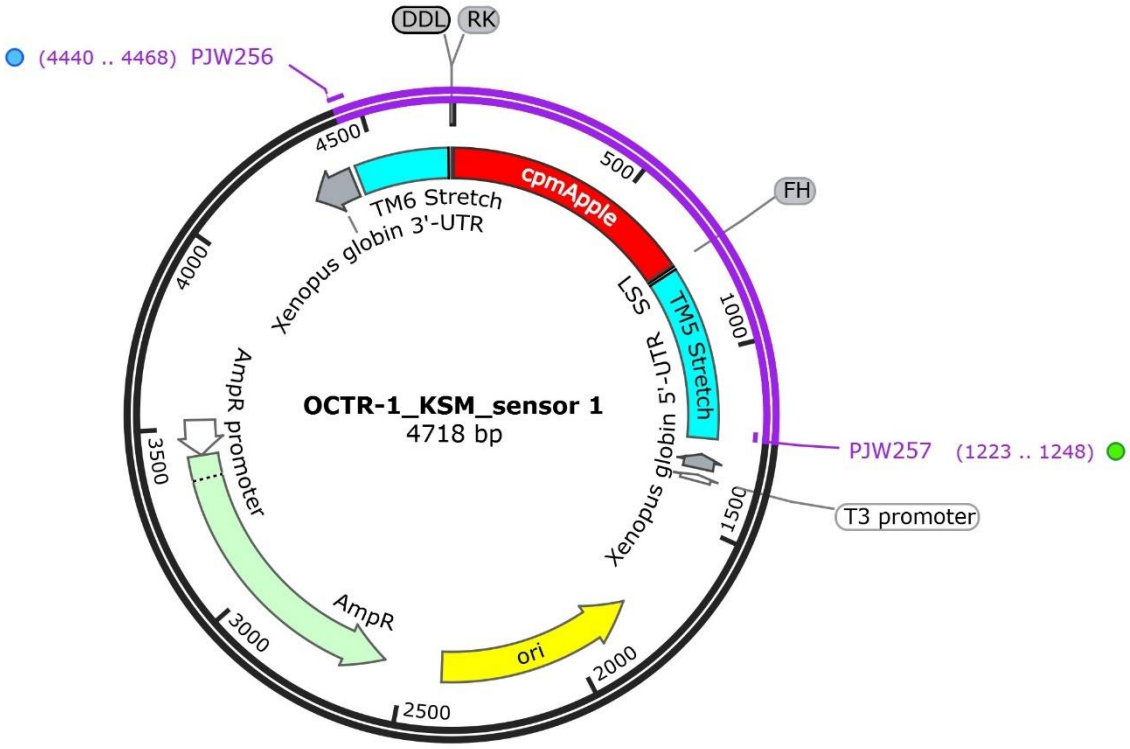


**Figure 29. Plasmid map of OCTR-1 KSM sensor variant 1 with primer annealing sites for directional TOPO cloning.** A pair of primers anneals at both ends of all sensor constructs, and amplifies the entire region indicated in purple. Amplicons are used for directional TOPO cloning into a pcDNA3.1 vector for expression in mammalian HEK293 cells.

**Table 12. Primers used for directional cloning into pcDNA3.1.** The annealing sites of each primer can be found on the plasmid map above using the color code.

| Primer | Oligonucleotide Sequence | 3'Tm | 3'Ta | Amplicon |
|---|---|---|---|---|
| PJW257 (forward) | **CACC**ATGTGGAACCTTAACTGCAGTGAAAG | 71°C | 68°C | 1531 bp |
| PJW256 (reverse) | TCATTTGTAGAACTCCATGAGTGGATGAA | 67°C | | |

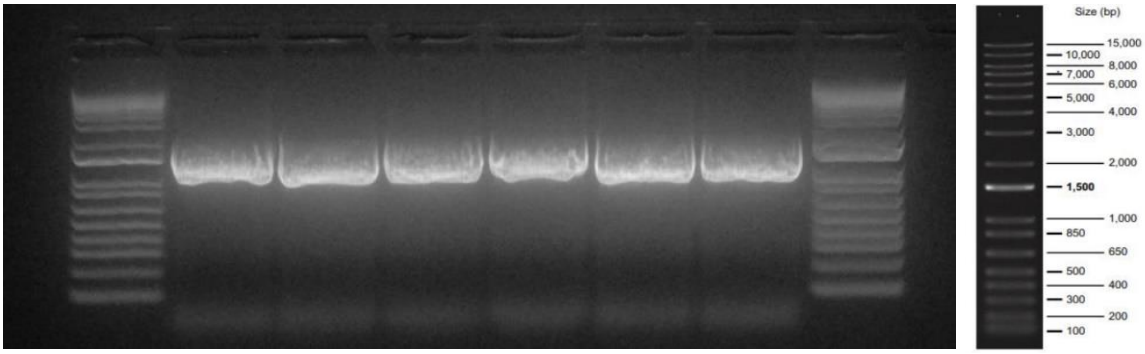


**Figure 30. Gel electrophoresis confirming a correct size of amplicons of all OCTR-1 sensor variants (1 to 6, left to right).** On the left, a 1 kb plus ladder is shown. Positive bands are located around 1500 bp.

The length of PCR products was checked by gel electrophoresis (Figure 30) and bands of the correct size were excised for purification and subsequent directional TOPO cloning. Correct insertion into the pcDNA3.1 backbone was examined by colony PCR with PJW248 and PJW247 (BGH reverse primer). The primers for colony PCR were designed to amplify the 3' end of the sensor including the TM6 stretch and the linkers (Figure 31).

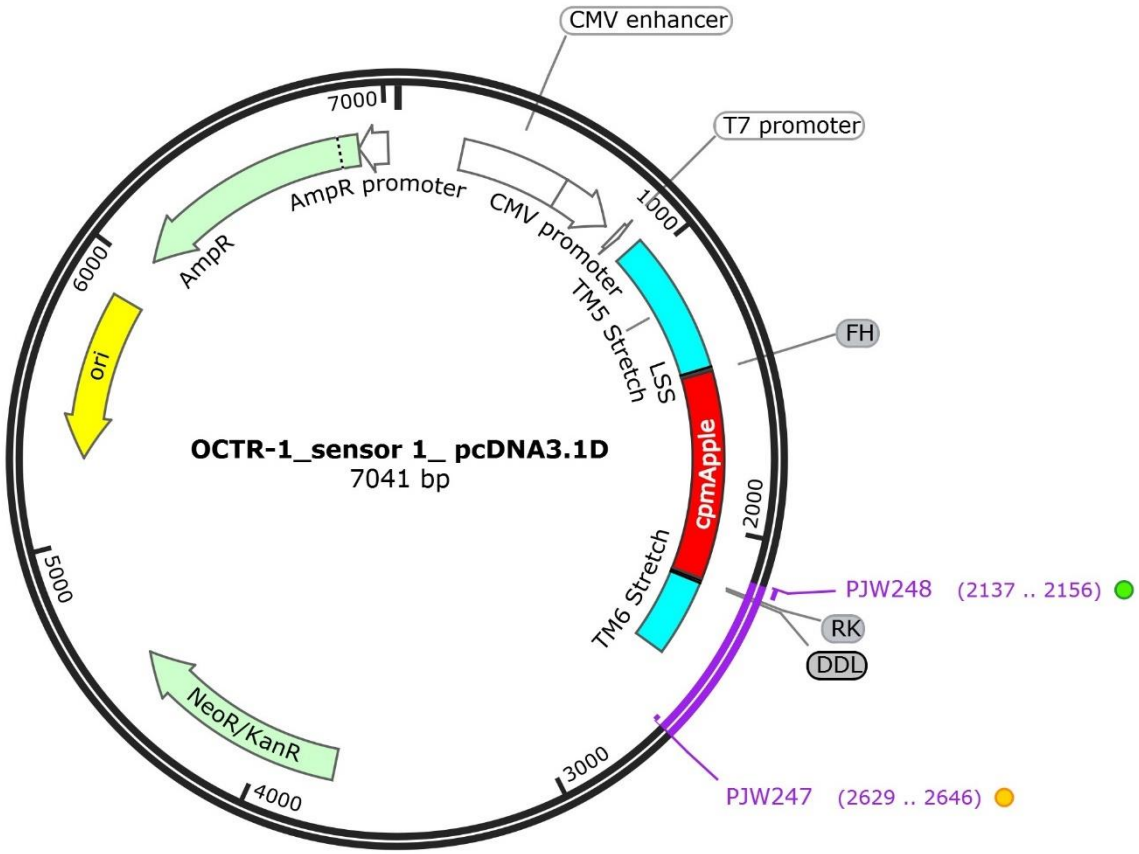


**Figure 31. Plasmid map of OCTR-1 sensor variant 1 in pcDNA3.1 vector after directional TOPO cloning.** To confirm the correct insertion, colony PCR is conducted using PJW247 and PJW248. The amplified regions are indicated in purple.

**Table 13. Primers for colony PCR of OCTR-1 sensors cloned into pcDNA3.1.** The annealing sites of each primer can be found on the plasmid map above using the color code.

| Primer | Oligonucleotide Sequence | 3'Tm | 3'Ta | Amplicon |
|---|---|---|---|---|
| PJW248 (forward) | CAGACGGACCAGTTATGCAG | 58°C | 55°C | 503 bp |
| PJW247 (BGH reverse) | TAGAAGGCACAGTCGAGG | 56°C | | |
| PJW246 (T7 promoter) | TAATACGACTCACTATAGGG | | | |

After gel electrophoresis (Figure 32), the colonies with positive bands were further sequenced. To ensure the complete insertion of the sensor construct, the samples were sequenced with multiple primers, PJW247 and PJW246 (T7 promoter primer) (Table 13), respectively. This way, the entire sequence of the construct could be checked from both ends. Also, regions with questionable sequencing results were individually cross-examined on both sequence chromatograms.

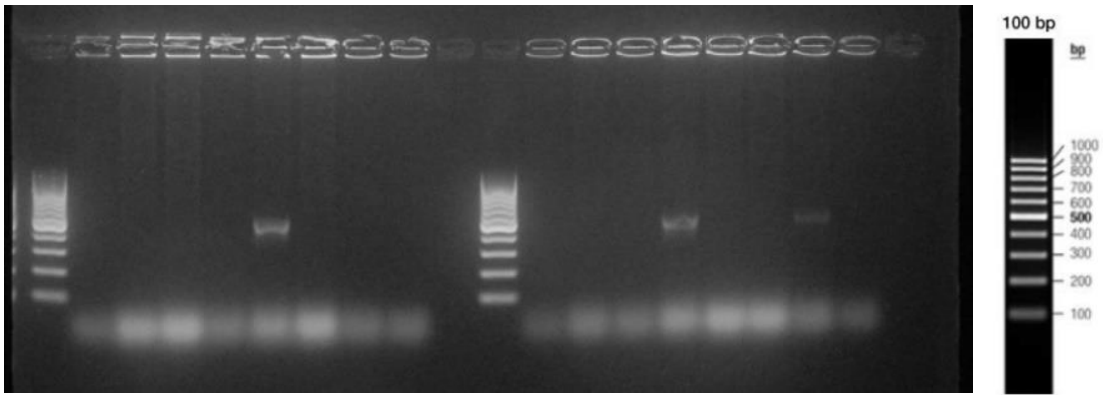


**Figure 32. Gel electrophoresis confirming a correct insertion of the OCTR-1 sensor (variant 3) into pcDNA3.1.** On the right, a 100 bp DNA ladder is shown and positive bands are located around 500 bp.

Ultimately, we successfully obtained pcDNA3.1 constructs for OCTR-1 sensor variants 1, 2, 3 and 4. However, no positive band was observed for variant 5 and variant 6 even after several attempts. Thus, only 4 variants were further characterized *in vitro* after transfection of HEK293 cells.

## 3.3. *in vitro* HEK293 cell assay for sensor characterization

### 3.3.1. Basal fluorescence

To characterize the performance of the 6 OCTR-1 sensor variants, GPCR sensors were expressed in mammalian HEK293 cells, which are the preferred cell line for this application owing to the availability of well-established culture and transfection techniques, as well as their long-established use for the study of GPCR signaling (Thomas and Smart, 2005). HEK293 cells were transfected with the sensor-containing plasmids at varying plasmid to cell ratios. As different transfection conditions did not seem to affect the cells, the condition yielding the highest confluency was selected for further transfection.

Initially, transfected cells were incubated at 28°C, instead of 37°C, overnight prior to testing the GPCR sensor, because the lower cultivation temperature facilitates the functional expression of *C. elegans* proteins and it is often required for heterologous expression *of C. elegans* GPCRs (Kubiak *et al*., 2003). However, as this seemed to affect cell viability, cells were incubated at 37°C for the remaining experiments, which is the optimal temperature for mammalian cell growth.

First, basal red fluorescence emanating from the cpmApple protein intracellularly fused to the OCTR-1 TM5 and TM6 was visualized using fluorescence microscopy. Prior to basal fluorescence imaging, cell culture medium containing phenol red was manually exchanged with the colorless HBSS buffer to reduce fluorescence quenching. Unfortunately, this process disturbed the cell layer and caused cells to detach from the bottom of well. Especially, adding medium rather than removing it was more invasive based on observation (Figure 33a-c). Despite this major drawback, it was a necessary step for reducing background fluorescence, as is illustrated in the following figure (Figure 33d-f).

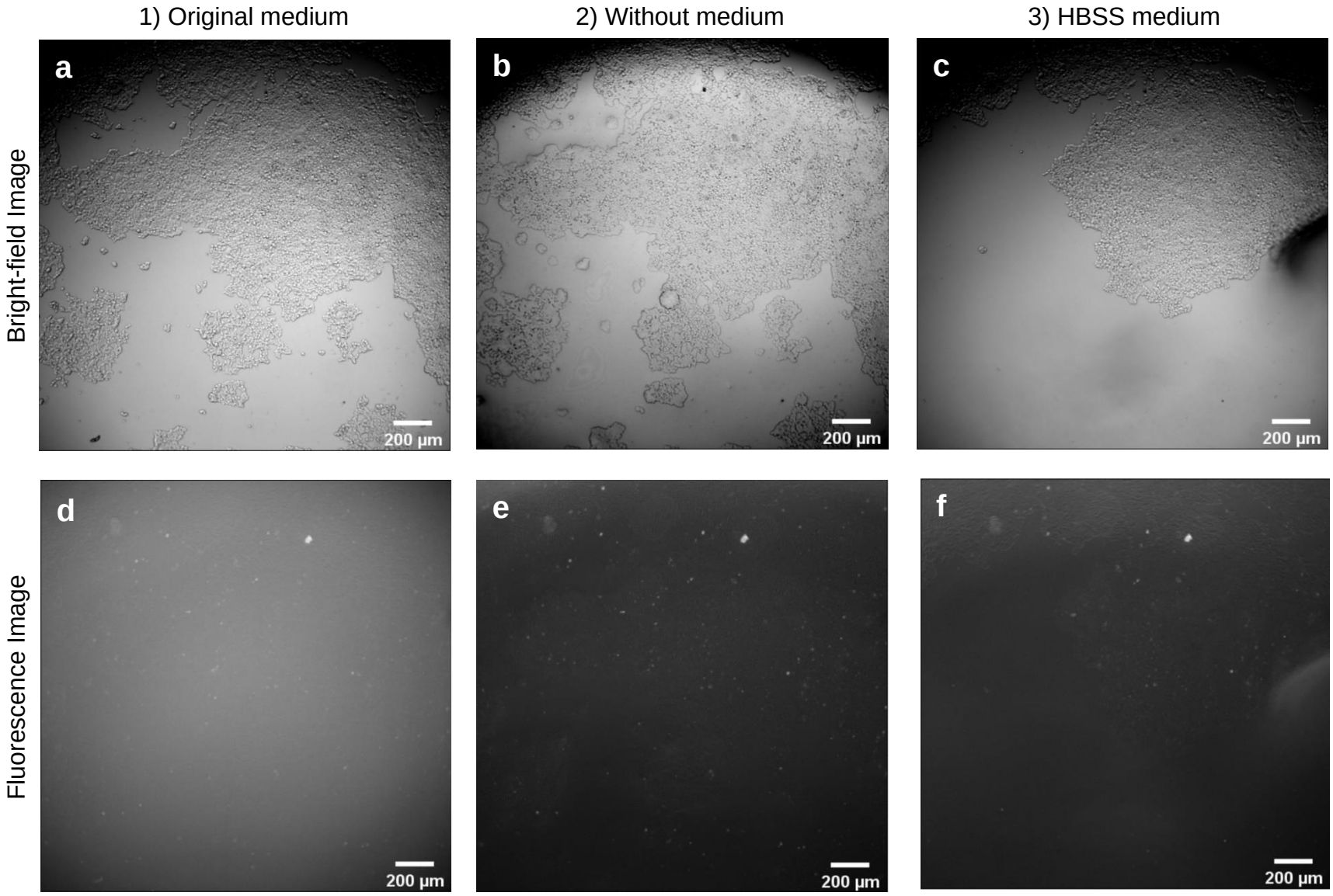


**Figure 33. Microscopic images of HEK293 cells transfected with OCTR-1 sensor variant 4 in the process of medium exchange (5X).** Images were acquired to observe cell disturbance caused by the medium exchange 1) in original medium (a) bright-field (d) fluorescence, 2) after removing the original medium (b) bright-field (e) fluorescence, and 3) after adding HBSS medium (c) bright-field (d) fluorescence image setting. The process of adding medium caused detachment of the cell layer, however, effectively reduced background fluorescence.

Basal red fluorescence could be visualized in HEK293 cells transfected with each of the four OCTR-1 sensor variants. An illustrative overlay composite image of the brightfield and fluorescence image of HEK293 cells transfected with OCTR-1 sensor variant 2 is shown in the figure below (Figure 34). Altogether, the presence of red fluorescence after transfection indicates that the cpmApple indicator is properly inserted into the *octr-1* gene and the fusion protein – or the cpmApple component at least - is properly expressed and folded in HEK293 cells.

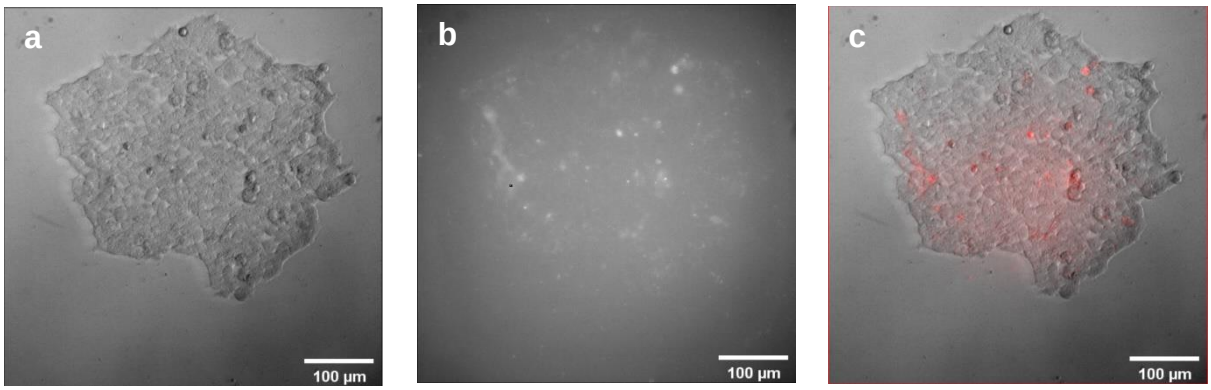


**Figure 34. Microscopic images of HEK293 cells transfected with OCTR-1 variant 2 in (a) bright-field, (b) fluorescence and (c) an overlayed image (20X).** Red fluorescence is localized on the patch of cells indicating proper folding and expression of cpmApple in the sensor construct.

### 3.3.2. Addition of octopamine

To characterize whether any of the OCTR-1 sensor variants faithfully relays octopamine signaling *in vitro*, fluorescent changes were monitored upon exogenous challenge with the natural ligand. Initially, we attempted to acquire videos of the sensor activity upon manual addition of octopamine to the imaged well, as it would be a straightforward way of assessing the crude performance of the different sensor variants. However, the movement of the pipette tip caused too much fluctuation in the background during the manual application of octopamine into the wells. Also, the exposure time needed to visualize basal red fluorescence was too long to render a good quality video. Thus, we reached a conclusion that it was unfeasible to acquire a video for proper analyses and quantification under the current imaging conditions. Instead, three consecutive static images were obtained to investigate the response of the sensor to the octopamine. A first image ($t_0$) was obtained before octopamine was applied, indicating basal fluorescence. A second image was acquired immediately after octopamine was applied, and a third image was obtained 30 seconds after the application. Based on visual inspection, no obvious change in fluorescence signal was observed (Figure 35).

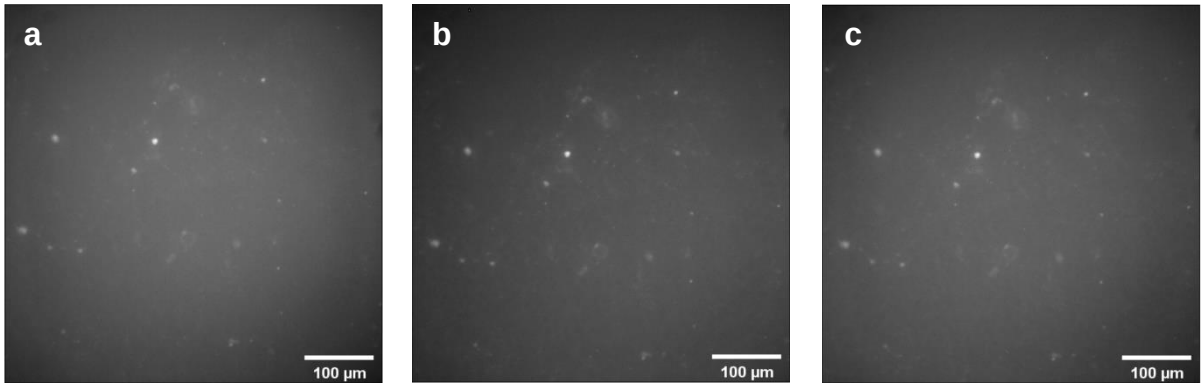


**Figure 35. Microscopic images of HEK293 cells transfected with OCTR-1 sensor variant 2 in (a) before adding octopamine (b) right after adding octopamine (c) 30 seconds after adding octopamine (20X).** Fluorescent signals are localized on the patch of cells indicating proper folding and expression of cpmApple in the sensor construct.

### 3.3.3. Quantification of fluorescence intensity

Generally, the performance of a sensor is measured by the fold-change in fluorescence (*ΔF/F*). It is defined by the ratio of a change of fluorescence (*ΔF*) to a basal fluorescence (*F*), where the change of fluorescence (*ΔF)* is calculated as the difference between the average fluorescence intensity of 10 frames after and before addition of the ligand (Patriarchi *et al*., 2019). Reported peak responses range from 90% to as high as 230% (Feng *et al*., 2019; Jing *et al*., 2019; Patriarchi *et al*., 2018, 2020; Sun *et al*., 2018, 2020).

However, this quantification method was not strictly applicable to our experiments as we could not acquire time-lapse images during perfusion of the ligand in our setup (Patriarchi *et al*., 2019). Thus, for objective quantification, 8 single areas – corresponding to single cells within a single well - were designated manually. For each area, the corrected total cellular fluorescence (CTCF) was computed in order to eliminate background fluorescence (see 2.3.3).

To note, while all 4 variants of OCTR-1 sensors were successfully cloned in pcDNA3.1, only variant 2 and 4 could be analyzed using this quantification method. For the initial batch of analysis (variant 1 and 3), the images were acquired using 5X magnification, however, manually assigning such small areas in the scale of a single cell was nearly impossible on 5X images. Hence, the rest of the images of variant 2 and 4 were acquired in higher magnification (20X), and they were subjected to the quantification of their fluorescence intensity.

For both variants, resultant CTCF values of each area vary greatly in magnitudes, therefore, CTCF values after addition of the ligand ($t_1$ and $t_2$) were normalized to the basal fluorescence ($t_0$) and plotted to estimate the trend of sensor responses (Figure 36, Figure 37). However, no consistent change was observed across different time points, and no trend was observed across the wells.

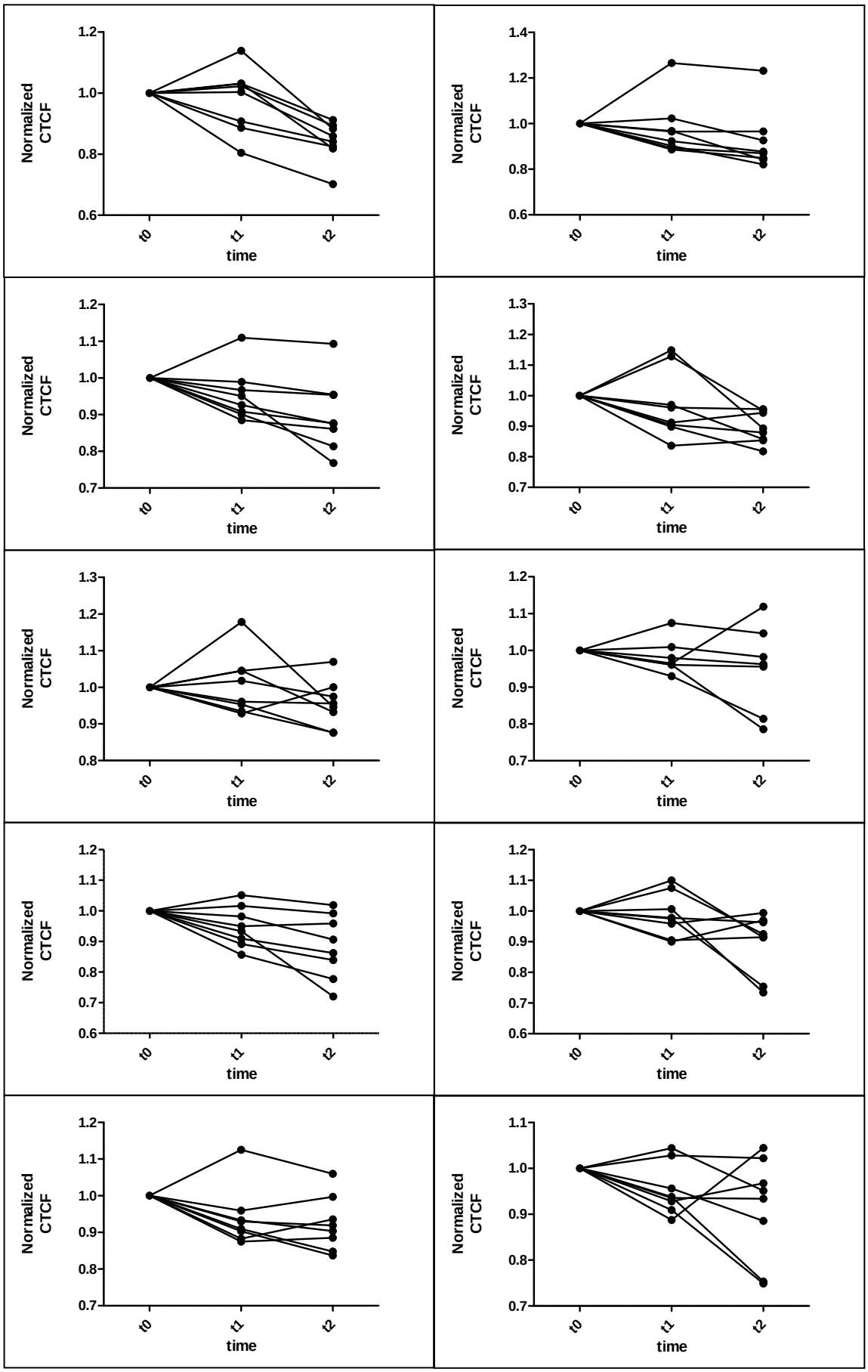


**Figure 36. Normalized corrected total cellular fluorescence (CTCF) of OCTR-1 sensor variant 2 upon addition of octopamine.** Each panel represents a single well containing biological replicates of variant 2, and the quantification results of 10 wells are shown. For the quantification, 8 ROI were selected from each well, and their CTCF was computed across 3 different time points ($t_0$: before adding octopamine, $t_1$: right after adding octopamine, $t_2$: 30 seconds after adding octopamine) indicated by single points. CTCF values after addition of the ligand ($t_1$ and $t_2$) were normalized to the basal fluorescence ($t_0$), and the normalized values were plotted against time.

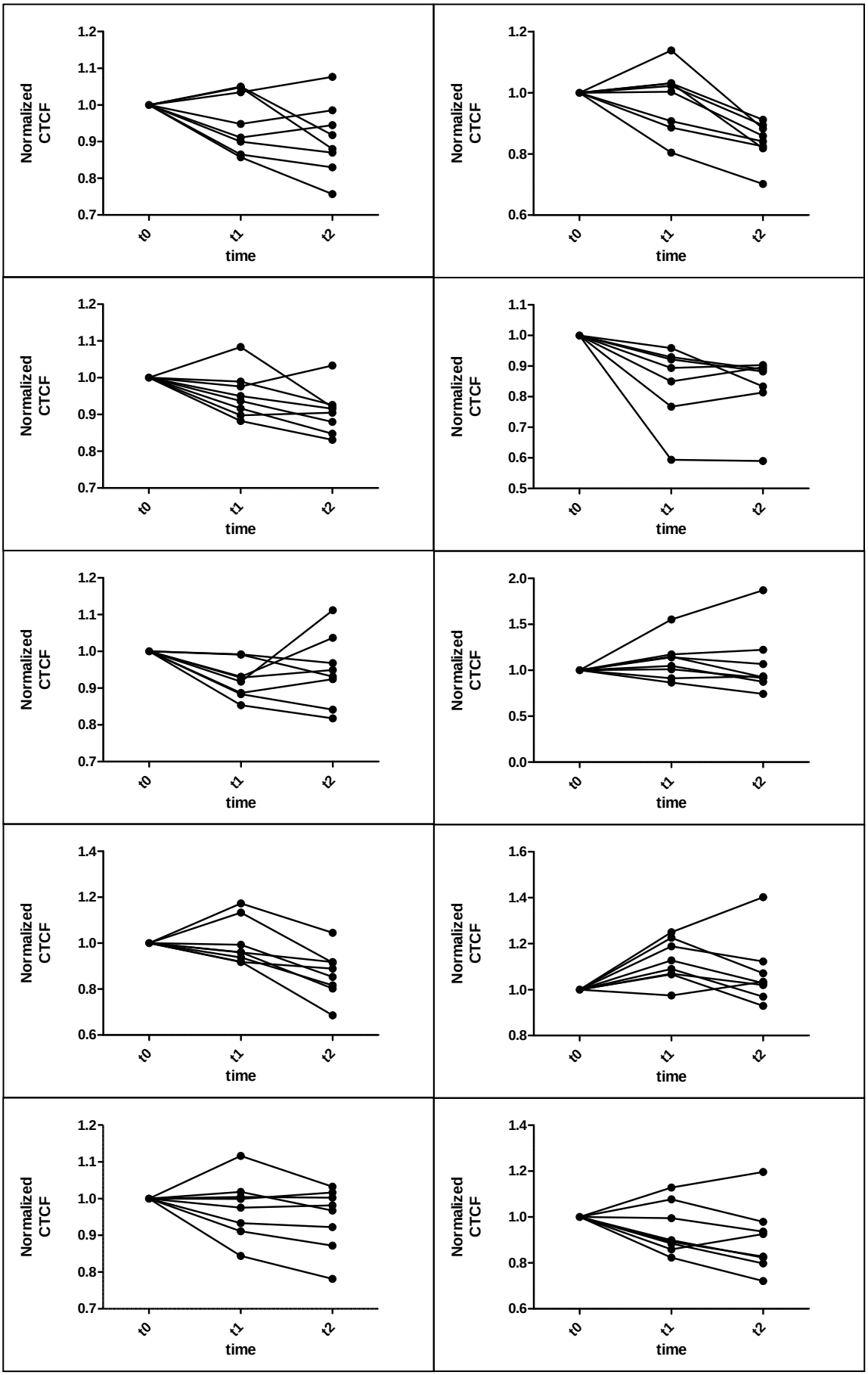


**Figure 37. Normalized corrected total cellular fluorescence (CTCF) of OCTR-1 sensor variant 4 upon addition of octopamine.** Each panel represents a single well containing biological replicates of variant 4, and the quantification results of 10 wells are shown. For the quantification, 8 ROI were selected from each well, and their CTCF was computed across 3 different time points ($t_0$: before adding octopamine, $t_1$: right after adding octopamine, $t_2$: 30 seconds after adding octopamine) indicated by single points. CTCF values after addition of the ligand ($t_1$ and $t_2$) were normalized to the basal fluorescence ($t_0$), and the normalized values were plotted against time.

# 4. Discussion

Lately, different methodologies have been described that allow neuromodulator signaling events to be visualized at high spatiotemporal resolution in living animals (Dong *et al*., 2021; Patriarchi *et al*., 2018, 2020; Sun *et al*., 2018, 2020; Wan *et al*., 2021; Zeng *et al*., 2019). Yet, this methodology is yet to be implemented in the nematode *C. elegans*. Monoaminergic neuromodulators are known to govern various aspects of *C. elegans* biology, such as learning, feeding behaviors, locomotion, memory, innate immunity and decision-making (Chute *et al*., 2019; Kindt *et al*., 2007; Sawin *et al*., 2000; Sellegounder *et al*., 2018; Srinivasan *et al*., 2008). While a growing body of work details the profound influence of monoaminergic signaling in *C. elegans* behavior and physiology, the lack of precise information on the timing and cellular focus of these signaling events precludes a proper understanding of these processes.

Therefore, this project set out to implement real-time GPCR activity sensors for octopamine (OCTR-1) and tyramine (TYRA-2a) receptors in *C. elegans*. In a first step, different sensor variants were designed and constructed using varying linker sequences. These sequences were acquired from previously engineered sensors (Feng *et al*., 2019; Patriarchi *et al*., 2018, 2020; Wan *et al*., 2021). Then, sensor variants were expressed in mammalian HEK293 cells to examine their properties. Basal fluorescence confirmed the expression of the sensors and octopamine was added to observe sensor responses. However, the sensors did not yield any significant change in fluorescence.

Ultimately, implementing these real-time GPCR sensors will allow us to visualize octopaminergic signaling *in vivo* with unprecedented spatiotemporal resolution, which can address many unsolved questions which could not be tackled with existing approaches. Here, several aspects of sensor development and suggestions for future experiments are discussed.

## 4.1 Sensor engineering design

The optimization of linker sequences and insertion sites remains as one of the biggest challenges in GPCR sensor engineering. While several sensors have been already developed, there is no clear guideline for designing linker sequences. Also, little is known about how conformational changes in the GPCR are transduced to the cpFP via the linkers upon ligand binding. Hence, linker sequences are almost exclusively the final product of laborious optimization processes which entail random mutagenesis and large screening efforts. For instance, 273 variants were screened for the development of the $GRAB_{NE}$ sensor (Feng *et al*., 2019) and 585 variants for dLight1.1 (Patriarchi *et al*., 2018) in order to yield the highest performing variant. As a result, linkers vary in terms of the length and amino acid sequence and across different – sometimes very similar – sensors.

In contrast, only 6 different candidates were tested in our project, which only differ in variable linker sequence. Our reasoning was that we might be able to simplify the extensive optimization process by adopting the linker sequences from sensors that were proven to function. Indeed, the insertion of already-optimized cpFP-linker cassettes into other neuromodulator GPCRs was shown to be a versatile engineering approach to generate intensity-based sensors for other neuromodulators (Patriarchi *et al*., 2018). Nonetheless, no robust fluorescence responses of the 4 tested OCTR-1 sensor variants to exogenously applied octopamine have been observed in this project, which will be discussed below.

In this project, sequence alignment with experimentally validated GPCR-sensors was used to identify the putative ICL3 region of the OCTR-1 and TYRA-2a receptors (section 3.1.1). However, transmembrane prediction based on the physicochemical properties of the protein sequence itself - obtained by other bioinformatics tools such as JalView and TMHMM (TMHMM Server v. 2.0) – resulted in ICL3 predictions that slightly differ from each other (Appendix II), suggesting that our current prediction of the OCTR-1 and TYRA-2a transmembrane domains may be inaccurate. Still, it is worth mentioning that the majority of proteins used for the alignment are vertebrate receptors, whereas OCTR-1 and TYRA-2a are invertebrate proteins. The large evolutionary distance between vertebrate and invertebrate GPCRs (Bauknecht and Jékely, 2017) may cloud a precise identification of the ICL3 using sequence alignment. Furthermore, unlike vertebrate DRD dopamine receptors used for the development of dLight and $GRAB_{DA}$ sensors (Patriarchi *et al*., 2018; Sun *et al*., 2018), OCTR-1 and TYRA-2a are comparatively less studied proteins. Therefore, there is less information available such as structural features for precise prediction. Given that our sensor design can be based on an inaccurate prediction of ICL3, the fluorescent indicator could have been fused to a wrong place in the receptor protein. Therefore, prediction data from different sources should be consulted for better estimation of the transmembrane domains in future experiments.

Taken together, GPCR sensor engineering requires several optimization steps, both in terms of the cpFP insertion site and the linker regions to connect the indicator to the receptor. This laborious procedure remains a major bottleneck in the implementation of real-time intensiometric GPCR sensors. Thus, it may be advisable to explore a rational design approach. As previously mentioned, current sensor engineering approaches inevitably rely on random engineering due to a lack of our understanding of the GPCR conformational changes upon ligand binding and the precise transduction of these structural changes to the cpFP over the linker sequences. But as more and more sensors – for different GPCRs - are being reported, the meta-analysis of these different sensors begins to provide a platform for the rational design of this type of sensor. In a recent review paper, the authors elaborated on the intricate interaction of the linker sequence and the beta barrel structure of the fluorescent indicator (Nasu *et al*., 2021). Along with proliferating advanced structural studies of different monoaminergic receptors, this is likely to facilitate the development of a wide variety of GPCR-based sensors in the scientific community.

## 4.2 Plasma membrane localization of the sensors

Prior to *in vivo* application, newly designed GPCR sensors are commonly tested for their performance upon heterologous expression in a cellular system (Patriarchi *et al*., 2019). Similarly, OCTR-1 sensor variants were transfected into mammalian HEK293 cells in this project. Upon successful transfection with the sensor construct, we observed basal cpmApple fluorescence. Thus, sensor proteins should have been correctly folded and expressed. Although red fluorescence hinted at correct translation of the cpmApple indicator imbedded within the OCTR-1 protein, it was difficult to confirm the plasma membrane localization of the sensor protein – which is essential for the interaction with octopamine – using the Zeiss AxioObserver Z1 fluorescent microscope. Confocal microscopy at higher magnifications will allow high-resolution optical signaling of the transfected HEK293 cells, and further address the subcellular localization of the OCTR-1 sensor variants.

The *C. elegans* native protein, OCTR-1, is expected to mature and fold ideally at around 15 to 25 degrees, which is the normal temperature range of cultivation for *C. elegans* (Stiernagle, 2006). Mammalian cells, however, thrive at around 37°C. Our initial visual observation of transfected HEK293 cells cultured at 28°C suggested the cells to be unhealthy at this temperature. Thus, in subsequent experiments the incubation temperature was kept at 37°C to maintain cell viability. Nonetheless, this could have affected the folding and trafficking of the sensor protein, leading to a failure in membrane localization. Importantly, temperature-dependent surface expression of GPCRs in mammalian cells has previously been reported (Kubiak *et al*., 2003). Similarly, a shift from 37°C to 28°C 24h before the assay is thought to be essential for OCTR-1 expression in different mammalian cells, including HEK293 (Wragg *et al*., 2007).

In addition to the temperature, the incubation time after transfection is an essential factor in cellular expression. For our experiments, the cells were cultured for maximum two days and there was no visual difference in one-day incubated cells and two-day incubated cells. Also, in the original methods described in different reports by Patriarchi and colleagues, two days were enough for the sensors to be functional (Patriarchi *et al*., 2018, 2019, 2020). Still, it cannot be ruled out that maturation and expression of OCTR-1 sensors may require additional time.

Also, it should be noted that there may be a compatibility issue with the *C. elegans* endoplasmic reticulum (ER) export motif for HEK293 cell expression. In (Husson *et al*., 2012), the use of an appropriate ER exit promoting motif was required to obtain efficient cell surface expression of the optogenetic protein halorhodopsin (NpHR) - of bacterial origin - in *C. elegans*. Taking this into account, it is possible that the use of *C. elegans* optimized signaling motifs may induce an analogous problem in a mammalian cell, eventually hindering proper insertion of the sensors into the plasma membrane.

In summary, it would be necessary to optimize the incubation temperature and duration of cell culture to ensure functional expression of the sensor proteins. As

suggested, cells should be incubated at 28°C for 24h prior to the fluorescence imaging and membrane localization of the sensors should be confirmed using confocal microscopy. If the sensors still fail to locate to the plasma membrane, optimization of an ER export motif may be required.

## 4.3 Image analysis and quantification

In this project, the fluorescence quantification was based on the manual selection of different regions of interest (ROIs). Eight different regions of high intensity were chosen from each fluorescence image to easily verify the fluorescence that emanates from HEK293 cells and not from fluorescent contaminants, which were often found in the sample. This process, however, is prone to errors as manually selecting the exact same area for three serial images required high precision, not to mention that it is a laborious task. In addition, selecting ROIs based on fluorescence intensity is innately biased. From the observation of the acquired images, it appeared that the cells of highest fluorescence intensity tend to be smaller in size and show a spherical morphology as if they were going through apoptosis. Cell shrinkage and condensed apoptotic body formation are common phenotypical changes that take place in the course of a programmed cell death (Elmore, 2007). Still, it would require further examinations to confirm if they are truly apoptotic cells. Given the possibility that apoptotic cells were preferentially selected for quantification, this might have led to an inaccurate interpretation, since they are not likely to respond to octopamine as normal healthy cells.

For a more objective quantification scheme, global analysis of the fluorescent images would be a better approach. In other studies, only a couple of cells are observed in full frame with high-resolution confocal microscopy (Dong *et al*., 2021; Patriarchi *et al*., 2018, 2020; Sun *et al*., 2018, 2020; Wan *et al*., 2021; Zeng *et al*., 2019). In that case, the entire image can be processed using a binary approach, which sets the threshold of fluorescence and allows intensities to be quantified in consistent manner.

## 4.4 Autofluorescence

Autofluorescence is naturally occurring fluorescence emission in biological structures. In cells, mitochondria and lysosomes contribute to the majority of the auto-fluorescence, along with molecules containing aromatic rings such as NADPH and flavin (Monici, 2005). Additionally, the commonly used complete cell culture medium solution contains autofluorescence nutrients that are necessary for the cells. In addition, phenol red is supplemented to the medium as a convenient colorimetric pH indicator for monitoring of $CO_2$ levels. However, phenol red is known to quench fluorescence, and furthermore can accumulate in the cell. There are several commercially available cell culture media that are optimized for live-cell fluorescence imaging to mediate this problem, for instance BrightCell™ Photostable Media (Sigma-aldrich) and FluoroBrite™ DMEM (Thermo Fischer). Washing cells with a similar

colorless buffer can be an alternative solution for reducing phenol red in the background when the special imaging medium is not available. Still, it should be taken into account that it may be not possible to completely remove phenol red accumulated in the cell. Moreover, in this project the rinsing step itself caused cells to detach from the surface. Methods to fix mammalian cells to their carrier before imaging exist but can introduce artifacts in the sample that could occlude GPCR-sensor fluorescence changes (Li *et al*., 2017).

Taken together, autofluorescence should ideally be distinguished from the signal of the sensor. Otherwise, it may lead to a skewed interpretation of the results as all the aforementioned factors can affect the final fluorescence intensity in different ways. Given that basal fluorescence in the absence of the sensor's ligand is – per definition – low in intensity (Patriarchi *et al*., 2020), it might be occluded by autofluorescence. To measure background autofluorescence, cells transfected with the empty pcDNA3.1 vector can be used as a convenient negative control. Void of any production of the sensor, this negative control can provide a good benchmark to estimate the contribution of background intensity from autofluorescence. In our experiments, weak fluorescent signals were often observed along the rim of the cell patches (Figure 34b, Figure 35). Although there is clear heterogeneity in the red fluorescence signal emanating from the transfected HEK293 cells, incorporating an empty pcDNA3.1-transfected control will help in resolving basal fluorescence of the OCTR-1 sensor variants from non-specific autofluorescence.

## 4.5 Instrumental setup

Using a common fluorescence microscope (Zeiss AxioObserver Z1), we uncovered red fluorescence in transfected HEK293 cells, suggesting the correct expression and folding of OCTR-1 sensors. However, this instrumental setup is limited in terms of axial and lateral resolution of the fluorescence patterns that can be visualized. A confocal microscope would be a more desirable choice for future experiments. Even though the acquisition rate may have to be compromised due to the slow nature of point-scanning confocal microscopy, it can provide better resolution images with higher magnification which is fundamentally more important to monitor the activation of the sensors. Visualizing HEK293 cells with a confocal microscope also requires alternative cell culture plates such as glass-bottom dishes (Mattek, cat. no. P35G-1.5-14-C) that can accommodate the use of higher magnification lenses (Patriarchi *et al*., 2019). In this project, 16-well plates fixed on a glass slide were used for efficient culture and imaging, but the thickness of the glass slide has proven to be incompatible with magnification lenses above 20X, which do not reach the desired focal point.

In addition to confocal imaging of HEK293 fluorescence, the use of a perfusion system would be highly recommended for future experiments. Perfusion systems allow continuous flow of the medium for cell culture without disturbance (Patriarchi *et al*., 2019). As previously mentioned, the process of changing medium and adding compound directly to the well plate using a pipette often causes invasive damage to

the cell layer, no matter how gently it was conducted. In fact, this was one of the main reasons why a global analysis of fluorescence images over different conditions was not possible. Automated perfusion systems can handle reagents in a more precise and controlled manner, which would enable careful application of the compound and exchange of the medium without significant loss or detachment of cells.

In the future, high-throughput screening systems such as the FLIPR® Penta (Molecular Devices, LLC - USA) could be implemented to efficiently monitor sensor activity in parallel and increase experimental throughput (Schroeder and Neagle, 1996; Sullivan *et al*., 1999). The FLIPR® system is a real-time cell-based screening system that is commonly used for pharmacological analysis of GPCRs and ion channels. It is equipped with automated pipettors and a high-speed camera, which makes it suitable for large-scale screening. When optics are configurated to measure red fluorescence, it can be used to automatically screen the response of sensor variants to specific compounds in 96-well plates in parallel.

## 4.6 *in vivo* implementation of sensors

Given that the aforementioned suggestions for further work are adopted, we expect functional OCTR-1 and TYRA-2a sensors to be obtained in the near future. Then, important properties of the sensors should be examined, including their dynamic range, sensitivity and binding kinetics by generating dose-response curves in addition to agonist-antagonist experiments prior to the *in vivo* implementation. Employing real-time GPCR sensors promises to shed important new light on neuromodulator signaling within living worms.

As mentioned in Table 1, OCTR-1 is known to play an important role in innate immunity of *C. elegans*. Since *C. elegans* lacks adaptive immunity, innate immunity is tightly regulated for survival as the first line of defense against pathogenic bacteria (Liu and Sun, 2021). Under normal circumstances, OCTR-1 in the sensory neurons ASI and ASH is involved in tonic activation of an immunoinhibitory pathway (Sun *et al*., 2011). However, in the presence of pathogenic bacteria such as *Pseudomonas aeruginosa*, the unfolded protein response (UPR) and expression of immune genes are triggered by downregulating the activation of OCTR-1 in ASH (Sun *et al*., 2012), whereas the ASI sensory neurons induce pathogen avoidance behavior (Cao *et al*., 2017). By selectively implementing OCTR-1 sensors in ASH and ASI, cell-specific activity patterns of octopaminergic signaling could be non-invasively observed optically *in vivo*. This has the potential to distinguish spatiotemporal effects of octopaminergic transmission, for instance by addressing whether ASI and ASH OCTR-1-mediated responses are triggered by temporally distinct octopaminergic signaling events.

Recently, it was discovered that tyramine seems to act on intestinal cells via OCTR-1 activating the unfolded protein response in endoplasmic reticulum Özbey *et al*., 2020. Tyraminergic activation of OCTR-1 can be visualized by implementing OCTR-1 sensors in intestinal cells of *C. elegans* preceded by the knockout of *tbh-1* in RIC to ensure that sensor activation is not mediated by octopamine (Alkema *et al*., 2005).

This way, many unanswered questions can be tackled such as whether tyramine functions in a hormone-like manner.

Optimistically, a properly engineered OCTR-1 sensor may be able to differentiate the activation pattern generated by the main agonist octopamine from that of tyramine. As a proof of concept, it was recently shown that serotonergic hallucinogenic drugs could be screened among other agonists by using their GPCR sensor, PsyLight (Dong *et al*., 2021). Based on the 5-HT2A receptor, this sensor could detect the specific hallucinogenic conformation of the receptor by analyzing the agonist-antagonist activation pattern of each candidate.

Taken together, real-time intensiometric GPCR sensors have clear advantages over other activity sensors such as those relying on transcriptional reporters, as they can provide a more detailed picture on monoaminergic signaling *in vivo.* However, it should not be overlooked that developing this type of sensor may require investment on the instrumentation side and requires considerable time for optimization of each sensor. It mainly stems from the lack of modularity, as every sensor should be designed and optimized respectively on each receptor of interest. Therefore, from our experience, it may be quite unfeasible to generate a library of real-time sensors. Rather, it would be advisable to generate a GPCR sensor based on a receptor of highest interest, then explore multiplexing possibilities with other existing sensors to maximize its potential. For instance, $GRAB_{DA}$ and GCaMP6s have been co-expressed in *Drosophila* for tracking of the dopaminergic signaling pathway and corresponding neuronal activity (Sun *et al*., 2020). As our sensors are designed with the red fluorescent indicator cpmApple, they can be readily co-expressed with green fluorescent sensors.

# 5. Conclusion

This research project set out to develop genetically encoded sensors to monitor endogenous neuromodulatory signaling events of octopamine and tyramine in *C. elegans.* These sensors were designed by replacing the entire third intracellular loop of *C. elegans* G protein-coupled receptors OCTR-1 and TYRA-2a with a circularly permuted cpmApple indicator. Then, clones were expressed in HEK293 mammalian cells to be characterized. We successfully generated different sensor variants for the OCTR-1 receptor. However, no significant change in fluorescence emission was observed upon external application of octopamine.

Our sensor engineering scheme was based on the development of RdLight, a GPCR sensor that monitors dopamine dynamics using the red fluorescence indicator, cpmApple (Patriarchi *et al*., 2020). This approach can be referred to as “semi-rational”, due to its versatile applicability as seen in the development of preliminary sensors for norepinephrine, serotonin, melatonin and opioid, among other neuropeptides (Ravotto *et al*., 2020). However, engineering GPCR sensors following this strategy may not be as straightforward and simple as it has been described. This is illustrated by the work in this project, which shows that an optimization process, including variant generation and large-scale screening, is still indispensable for developing well-functioning sensors.

Currently, the development of GPCR sensors inevitably relies on screening approaches as there is little information available regarding the conformational changes of the receptor upon ligand binding and how these changes are transduced to a fluorescent indicator on a molecular level. Therefore, structural studies should be paralleled to provide valuable insights on the intricate interactions of each GPCR component with the sensor module to facilitate a rational design in the engineering of additional sensors.

Despite all the challenges in engineering, GPCR sensors have an incomparable edge over neurogenetic interventions that are commonly used to study neuromodulatory signaling. Spatially and temporally resolved neuromodulatory signals can provide more direct clues for understanding the complex nature of monoamine signaling. Furthermore, GPCR sensors can unfold their potential when coupled to other fluorescent sensors that are spectrally orthogonal. Therefore, it is unquestionable that OCTR-1 sensors could provide an elegant solution for investigating octopamine dynamics in *C. elegans*.

# Bibliography


Alkema, M.J., Hunter-Ensor, M., Ringstad, N., and Horvitz, H.R. (2005). Tyramine functions independently of octopamine in the *Caenorhabditis elegans* nervous system. Neuron *46*, 247–260.

Ardiel, E.L., and Rankin, C.H. (2010). An elegant mind: Learning and memory in *Caenorhabditis elegans*. Learning & Memory *17*.

Bagur, R., and Hajnóczky, G. (2017). Intracellular $Ca^{2+}$ Sensing: Its Role in Calcium Homeostasis and Signaling. Molecular Cell *66*.

Bang, I., and Choi, H.-J. (2015). Structural Features of β2 Adrenergic Receptor: Crystal Structures and Beyond. Molecules and Cells *38*.

Barclay, J.W., Morgan, A., and Burgoyne, R.D. (2005). Calcium-dependent regulation of exocytosis. Cell Calcium *38*, 343–353.

Bargmann, C.I. (2012). Beyond the connectome: How neuromodulators shape neural circuits. BioEssays *34*.

Bargmann, C.I., and Marder, E. (2013). From the connectome to brain function. Nature Methods *10*.

Barnea, G., Strapps, W., Herrada, G., Berman, Y., Ong, J., Kloss, B., Axel, R., and Lee, K.J. (2008). The genetic design of signaling cascades to record receptor activation. Proceedings of the National Academy of Sciences *105*, 64.

Bauknecht, P., and Jékely, G. (2017). Ancient coexistence of norepinephrine, tyramine, and octopamine signaling in bilaterians. BMC Biology *15*.

Bentley, B., Branicky, R., Barnes, C.L., Chew, Y.L., Yemini, E., Bullmore, E.T., Vértes, P.E., and Schafer, W.R. (2016). The Multilayer Connectome of *Caenorhabditis elegans*. PLOS Computational Biology *12*.

Berry, M.D. (2004). Mammalian central nervous system trace amines. Pharmacologic amphetamines, physiologic neuromodulators. Journal of Neurochemistry *90*, 257–271.

Blenau, W., and Baumann, A. (2001). Molecular and pharmacological properties of insect biogenic amine receptors: Lessons from *Drosophila melanogaster and Apis mellifera*. Archives of Insect Biochemistry and Physiology *48*.

Borowsky, B., Adham, N., Jones, K.A., Raddatz, R., Artymyshyn, R., Ogozalek, K.L., Durkin, M.M., Lakhlani, P.P., Bonini, J.A., Pathirana, S., et al. (2001). Trace amines: Identification of a family of mammalian G protein-coupled receptors. Proceedings of the National Academy of Sciences *98*, 8966.

Bostock, M.J., Solt, A.S., and Nietlispach, D. (2019). The role of NMR spectroscopy in mapping the conformational landscape of GPCRs. Current Opinion in Structural Biology *57*.

Branco, A.C.C.C., Yoshikawa, F.S.Y., Pietrobon, A.J., and Sato, M.N. (2018). Role of Histamine in Modulating the Immune Response and Inflammation. Mediators of Inflammation *2018*.

Brittin, C.A., Cook, S.J., Hall, D.H., Emmons, S.W., and Cohen, N. (2021). A multi-scale brain map derived from whole-brain volumetric reconstructions. Nature *591*.

Callier, S., Snapyan, M., Crom, S., Prou, D., Vincent, J.-D., and Vernier, P. (2003). Evolution and cell biology of dopamine receptors in vertebrates. Biology of the Cell *95*.

Cao, X., Kajino-Sakamoto, R., Doss, A., and Aballay, A. (2017). Distinct Roles of Sensory Neurons in Mediating Pathogen Avoidance and Neuropeptide-Dependent Immune Regulation. Cell Reports *21*.

Casiraghi, M., Point, E., Pozza, A., Moncoq, K., Banères, J.-L., and Catoire, L.J. (2019). NMR analysis of GPCR conformational landscapes and dynamics. Molecular and Cellular Endocrinology *484*.

Catoni, C., Calì, T., and Brini, M. (2019). Calcium, dopamine and neuronal calcium sensor 1: Their contribution to Parkinson's disease. Frontiers in Molecular Neuroscience *12*.

Chase, D.L., and Koelle, M.R. (2007). Biogenic amine neurotransmitters in *C. elegans*. WormBook : The Online Review of *C. elegans* Biology 1–15.

Churgin, M.A., McCloskey, R.J., Peters, E., and Fang-Yen, C. (2017). Antagonistic serotonergic and octopaminergic neural circuits mediate food-dependent locomotory behavior in *Caenorhabditis elegans*. Journal of Neuroscience *37*, 7811–7823.

Chute, C.D., DiLoreto, E.M., Zhang, Y.K., Reilly, D.K., Rayes, D., Coyle, V.L., Choi, H.J., Alkema, M.J., Schroeder, F.C., and Srinivasan, J. (2019). Co-option of neurotransmitter signaling for inter-organismal communication in *C. elegans*. Nature Communications *10*.

Cook, S.J., Jarrell, T.A., Brittin, C.A., Wang, Y., Bloniarz, A.E., Yakovlev, M.A., Nguyen, K.C.Q., Tang, L.T.H., Bayer, E.A., Duerr, J.S., *et al*. (2019). Whole-animal connectomes of both *Caenorhabditis elegans* sexes. Nature *571*, 63–71.

Cormack, B.P., Valdivia, R.H., and Falkow, S. (1996). FACS-optimized mutants of the green fluorescent protein (GFP). Gene *173*.

Corsi, A.K., Wightman, B., and Chalfie, M. (2015). A transparent window into biology: A primer on *Caenorhabditis elegans*. Genetics *200*, 387–407.

Curran, K.P., and Chalasani, S.H. (2012). Serotonin circuits and anxiety: what can invertebrates teach us? Invertebrate Neuroscience: IN *12*, 81–92.

Dogra, S., Sona, C., Kumar, A., and Yadav, P.N. (2016). Chapter 12 - Tango assay for ligand-induced GPCR–β-arrestin2 interaction: Application in drug discovery. In Methods in Cell Biology, A. K. Shukla, ed. (Academic Press), pp. 233–254.

Dong, C., Ly, C., Dunlap, L.E., Vargas, M. v., Sun, J., Hwang, I.-W., Azinfar, A., Oh, W.C., Wetsel, W.C., Olson, D.E., *et al*. (2021). Psychedelic-inspired drug discovery using an engineered biosensor. Cell *184*.

Donnelly, J.L., Clark, C.M., Leifer, A.M., Pirri, J.K., Haburcak, M., Francis, M.M., Samuel, A.D.T., and Alkema, M.J. (2013). Monoaminergic Orchestration of Motor Programs in a Complex *C. elegans* Behavior. PLoS Biology *11*.

Duerr, J.S., Frisby, D.L., Gaskin, J., Duke, A., Asermely, K., Huddleston, D., Eiden, L.E., and Rand, J.B. (1999). The cat-1 Gene of *Caenorhabditis elegans* Encodes a Vesicular Monoamine Transporter Required for Specific Monoamine-Dependent Behaviors. The Journal of Neuroscience *19*.

Edgley, M. (2002). Improved detection of small deletions in complex pools of DNA. Nucleic Acids Research *30*.

Eiden, E.L. (2000). The vesicular neurotransmitter transporters: current perspectives and future prospects. The FASEB Journal *14*, 2396–2400.

Eiden, L.E., and Weihe, E. (2011). VMAT2: A dynamic regulator of brain monoaminergic neuronal function interacting with drugs of abuse. Annals of the New York Academy of Sciences *1216*, 86–98.

Elmore, S. (2007). Apoptosis: A Review of Programmed Cell Death. Toxicologic Pathology *35*.

Feng, J., Zhang, C., Lischinsky, J.E., Jing, M., Zhou, J., Wang, H., Zhang, Y., Dong, A., Wu, Z., Wu, H., *et al*. (2019). A Genetically Encoded Fluorescent Sensor for Rapid and Specific In Vivo Detection of Norepinephrine. Neuron *102*, 745-761.e8.

Frooninckx, L., van Rompay, L., Temmerman, L., van Sinay, E., Beets, I., Janssen, T., Husson, S.J., and Schoofs, L. (2012). Neuropeptide GPCRs in *C. elegans*. Frontiers in Endocrinology *3*.

Frostne, L., Sundström, L., and Huggins, C. (2011). Measuring GPCR Activity Using the Tango GPCR Assay on the FLIPR Tetra Fluorimetric Imaging Plate Reader System. (Molecular Devices).

Gainetdinov, R.R., Hoener, M.C., and Berry, M.D. (2018). Trace amines and their receptors. Pharmacological Reviews *70*, 549–620.

Ghosh, D.D., Sanders, T., Hong, S., McCurdy, L.Y., Chase, D.L., Cohen, N., Koelle, M.R., and Nitabach, M.N. (2016). Neural Architecture of Hunger-Dependent Multisensory Decision Making in *C. elegans*. Neuron *92*, 1049–1062.

di Giovanni, G., Svob Strac, D., Sole, M., Unzeta, M., Tipton, K.F., Mück-Šeler, D., Bolea, I., della Corte, L., Nikolac Perkovic, M., Pivac, N., *et al*. (2016). Monoaminergic and Histaminergic Strategies and Treatments in Brain Diseases. Frontiers in Neuroscience *10*.

Goldstein, D.S. (2010). Adrenal Responses to Stress. Cellular and Molecular Neurobiology *30*.

Gore, B.B., Soden, M.E., and Zweifel, L.S. (2014). Visualization of plasticity in fear-evoked calcium signals in midbrain dopamine neurons. Learning & Memory *21*.

Hapiak, V., Summers, P., Ortega, A., Law, W.J., Stein, A., and Komuniecki, R. (2013). Neuropeptides amplify and focus the monoaminergic inhibition of nociception in *Caenorhabditis elegans*. Journal of Neuroscience *33*, 14107–14116.

Hilger, D., Masureel, M., and Kobilka, B.K. (2018). Structure and dynamics of GPCR signaling complexes. Nature Structural & Molecular Biology *25*.

Hochman, S. (2015). Metabolic recruitment of spinal locomotion: intracellular neuromodulation by trace amines and their receptors. Neural Regeneration Research *10*.

Husson, S.J., Liewald, J.F., Schultheis, C., Stirman, J.N., Lu, H., and Gottschalk, A. (2012). Microbial Light-Activatable Proton Pumps as Neuronal Inhibitors to Functionally Dissect Neuronal Networks in *C. elegans*. PLoS ONE *7*.

Inagaki, H.K., Ben-Tabou de-Leon, S., Wong, A.M., Jagadish, S., Ishimoto, H., Barnea, G., Kitamoto, T., Axel, R., and Anderson, D.J. (2012). Visualizing Neuromodulation In Vivo: TANGO-Mapping of Dopamine Signaling Reveals Appetite Control of Sugar Sensing. Cell *148*.

Jaquins-Gerstl, A., and Michael, A.C. (2015). A review of the effects of FSCV and microdialysis measurements on dopamine release in the surrounding tissue. The Analyst *140*.

Jarrell, T.A., Wang, Y., Bloniarz, A.E., Brittin, C.A., Xu, M., Thomson, J.N., Albertson, D.G., Hall, D.H., and Emmons, S.W. (2012). The Connectome of a Decision-Making Neural Network. Science *337*.

Javer, A., Currie, M., Lee, C.W., Hokanson, J., Li, K., Martineau, C.N., Yemini, E., Grundy, L.J., Li, C., Ch'ng, Q., *et al*. (2018). An open-source platform for analyzing and sharing worm-behavior data. Nature Methods *15*.

Jin, X., Pokala, N., and Bargmann, C.I. (2016). Distinct Circuits for the Formation and Retrieval of an Imprinted Olfactory Memory. Cell *164*, 632–643.

Jing, M., Zhang, P., Wang, G., Feng, J., Mesik, L., Zeng, J., Jiang, H., Wang, S., Looby, J.C., Guagliardo, N.A., *et al*. (2018). A genetically encoded fluorescent acetylcholine indicator for in vitro and in vivo studies. Nature Biotechnology *36*.

Jing, M., Zhang, Y., Wang, H., and Li, Y. (2019). G-protein-coupled receptor-based sensors for imaging neurochemicals with high sensitivity and specificity. Journal of Neurochemistry *151*, 279–288.

Jing, M., Li, Y., Zeng, J., Huang, P., Skirzewski, M., Kljakic, O., Peng, W., Qian, T., Tan, K., Zou, J., *et al*. (2020). An optimized acetylcholine sensor for monitoring in vivo cholinergic activity. Nature Methods *17*.

Kagawa-Nagamura, Y., Gengyo-Ando, K., Ohkura, M., and Nakai, J. (2018). Role of tyramine in calcium dynamics of GABAergic neurons and escape behavior in *Caenorhabditis elegans*. Zoological Letters *4*.

Katz, P.S., and Lillvis, J.L. (2014). Reconciling the deep homology of neuromodulation with the evolution of behavior. Current Opinion in Neurobiology *29*, 39–47.

Kim, N., Shin, S., and Bae, S.W. (2021). cAMP Biosensors Based on Genetically Encoded Fluorescent/Luminescent Proteins. Biosensors *11*.

Kim, M. W., Wang, W., Sanchez, M. I., Coukos, R., von Zastrow, M., & Ting, A. Y. (2017). Time-gated detection of protein-protein interactions with transcriptional readout. eLife, 6, e30233.

Kindt, K.S., Quast, K.B., Giles, A.C., De, S., Hendrey, D., Nicastro, I., Rankin, C.H., and Schafer, W.R. (2007). Dopamine Mediates Context-Dependent Modulation of Sensory Plasticity in *C. elegans*. Neuron *55*.

Komar, A.A. (2016). The Yin and Yang of codon usage. Human Molecular Genetics *25*.

Korz, V., and Frey, J.U. (2007). Hormonal and monoamine signaling during reinforcement of hippocampal long-term potentiation and memory retrieval. Learning and Memory *14*, 160–166.

Kostyuk, A.I., Demidovich, A.D., Kotova, D.A., Belousov, V. v., and Bilan, D.S. (2019). Circularly permuted fluorescent protein-based indicators: History, principles, and classification. International Journal of Molecular Sciences *20*.

Kroeze, W.K., Sassano, M.F., Huang, X.-P., Lansu, K., McCorvy, J.D., Giguère, P.M., Sciaky, N., and Roth, B.L. (2015). PRESTO-Tango as an open-source resource for interrogation of the druggable human GPCRome. Nature Structural & Molecular Biology *22*.

Kubiak, T.M., Larsen, M.J., Nulf, S.C., Zantello, M.R., Burton, K.J., Bowman, J.W., Modric, T., and Lowery, D.E. (2003). Differential Activation of “Social” and “Solitary” Variants of the *Caenorhabditis elegans* G Protein-coupled Receptor NPR-1 by Its Cognate Ligand AF9. Journal of Biological Chemistry *278*.

Latorraca, N.R., Venkatakrishnan, A.J., and Dror, R.O. (2017). GPCR Dynamics: Structures in Motion. Chemical Reviews *117*.

Leavesley, S.J., and Rich, T.C. (2016). Overcoming limitations of FRET measurements. Cytometry Part A *89*.

Lee, D., Creed, M., Jung, K., Stefanelli, T., Wendler, D.J., Oh, W.C., Mignocchi, N.L., Lüscher, C., and Kwon, H.B. (2017). Temporally precise labeling and control of neuromodulatory circuits in the mammalian brain. Nature Methods *14*, 495–503.

Li, C., and Kim, K. (2008). Neuropeptides. WormBook : The Online Review of *C. elegans* Biology 1–36.

Li, Y., Almassalha, L.M., Chandler, J.E., Zhou, X., Stypula-Cyrus, Y.E., Hujsak, K.A., Roth, E.W., Bleher, R., Subramanian, H., Szleifer, I., *et al*. (2017). The effects of chemical fixation on the cellular nanostructure. Experimental Cell Research *358*.

Lindemann, L., Ebeling, M., Kratochwil, N.A., Bunzow, J.R., Grandy, D.K., and Hoener, M.C. (2005). Trace amine-associated receptors form structurally and functionally distinct subfamilies of novel G protein-coupled receptors. Genomics *85*, 372–385.

Lindenburg, L., and Merkx, M. (2014). Engineering Genetically Encoded FRET Sensors. Sensors *14*.

Liu, Y., and Sun, J. (2021). Detection of Pathogens and Regulation of Immunity by the *Caenorhabditis elegans* Nervous System. MBio *12*.

Liu, H., Qin, L.W., Li, R., Zhang, C., Al-Sheikh, U., and Wu, Z.X. (2019). Reciprocal modulation of 5-HT and octopamine regulates pumping via feedforward and feedback circuits in *C. elegans*. Proceedings of the National Academy of Sciences of the United States of America *116*, 7107–7112.

Luttrell, L.M., and Lefkowitz, R.J. (2002). The role of β-arrestins in the termination and transduction of G-protein-coupled receptor signals. Journal of Cell Science *115*, 455.

Ma, L., Jongbloets, B.C., Xiong, W.-H., Melander, J.B., Qin, M., Lameyer, T.J., Harrison, M.F., Zemelman, B. v., Mao, T., and Zhong, H. (2018). A Highly Sensitive A-Kinase Activity Reporter for Imaging Neuromodulatory Events in Awake Mice. Neuron *99*.

Mills, H., Wragg, R., Hapiak, V., Castelletto, M., Zahratka, J., Harris, G., Summers, P., Korchnak, A., Law, W., Bamber, B., *et al*. (2012). Monoamines and neuropeptides interact to inhibit aversive behaviour in *Caenorhabditis elegans*. EMBO Journal *31*, 667–678.

Mirabeau, O., and Joly, J.S. (2013). Molecular evolution of peptidergic signaling systems in bilaterians. Proceedings of the National Academy of Sciences of the United States of America *110*.

Monici, M. (2005). Cell and tissue autofluorescence research and diagnostic applications. In Biotechnology Annual Review, pp. 227–256.

Moyle, M.W., Barnes, K.M., Kuchroo, M., Gonopolskiy, A., Duncan, L.H., Sengupta, T., Shao, L., Guo, M., Santella, A., Christensen, R., *et al*. (2021). Structural and developmental principles of neuropil assembly in *C. elegans*. Nature *591*.

Muller, A., Joseph, V., Slesinger, P.A., and Kleinfeld, D. (2014). Cell-based reporters reveal in vivo dynamics of dopamine and norepinephrine release in murine cortex. Nature Methods *11*.

Murphy, D.L., Belmaker, R., and Wyatt, R.J. (1974). Monoamine oxidase in schizophrenia and other behavioral disorders. Journal of Psychiatric Research *11*, 221–247.

Mustard, J.A., Beggs, K.T., and Mercer, A.R. (2005). Molecular biology of the invertebrate dopamine receptors. Archives of Insect Biochemistry and Physiology *59*.

Nadim, F., and Bucher, D. (2014). Neuromodulation of neurons and synapses. Current Opinion in Neurobiology *29*, 48–56.

Nagai, T., Sawano, A., Park, E.S., and Miyawaki, A. (2001). Circularly permuted green fluorescent proteins engineered to sense $Ca^{2+}$. Proceedings of the National Academy of Sciences *98*.

Nakai, J., Ohkura, M., and Imoto, K. (2001). A high signal-to-noise $Ca^{2+}$ probe composed of a single green fluorescent protein. Nature Biotechnology *19*.

Nakamoto, C., Goto, Y., Tomizawa, Y., Fukata, Y., Fukata, M., Harpsøe, K., Gloriam, D.E., Aoki, K., and Takeuchi, T. (2020). A genetically encoded red fluorescence dopamine biosensor enables dual imaging of dopamine and norepinephrine. BioRxiv.

Nasu, Y., Shen, Y., Kramer, L., and Campbell, R.E. (2021). Structure- and mechanism-guided design of single fluorescent protein-based biosensors. Nature Chemical Biology *17*, 509–518.

Nguyen, Q.-T., Schroeder, L.F., Mank, M., Muller, A., Taylor, P., Griesbeck, O., and Kleinfeld, D. (2010). An in vivo biosensor for neurotransmitter release and in situ receptor activity. Nature Neuroscience *13*.

Nichols, D.E., and Nichols, C.D. (2008). Serotonin Receptors. Chemical Reviews *108*.

Niu, L., Li, Y., Zong, P., Liu, P., Shui, Y., Chen, B., and Wang, Z.-W. (2020). Melatonin promotes sleep by activating the BK channel in *C. elegans*. Proceedings of the National Academy of Sciences *117*.

Oe, Y., Wang, X., Patriarchi, T., Konno, A., Ozawa, K., Yahagi, K., Hirai, H., Tsuboi, T., Kitaguchi, T., Tian, L., *et al*. (2020). Distinct temporal integration of noradrenaline signaling by astrocytic second messengers during vigilance. Nature Communications *11*.

Özbey, N.P., Imanikia, S., Krueger, C., Hardege, I., Morud, J., Sheng, M., Schafer, W.R., Casanueva, M.O., and Taylor, R.C. (2020). Tyramine Acts Downstream of Neuronal XBP-1s to Coordinate Inter-tissue $UPR_{ER}$ Activation and Behavior in *C. elegans*. Developmental Cell *55*, 754-770.e6.

Palmer, A.E., Qin, Y., Park, J.G., and McCombs, J.E. (2011). Design and application of genetically encoded biosensors. Trends in Biotechnology *29*.

Patriarchi, T., Cho, J.R., Merten, K., Howe, M.W., Marley, A., Xiong, W.H., Folk, R.W., Broussard, G.J., Liang, R., Jang, M.J., *et al*. (2018). Ultrafast neuronal imaging of dopamine dynamics with designed genetically encoded sensors. Science *360*.

Patriarchi, T., Cho, J.R., Merten, K., Marley, A., Broussard, G.J., Liang, R., Williams, J., Nimmerjahn, A., von Zastrow, M., Gradinaru, V., *et al*. (2019). Imaging neuromodulators with high spatiotemporal resolution using genetically encoded indicators. Nature Protocols *14*, 3471–3505.

Patriarchi, T., Mohebi, A., Sun, J., Marley, A., Liang, R., Dong, C., Puhger, K., Mizuno, G.O., Davis, C.M., Wiltgen, B., et al. (2020). An expanded palette of dopamine sensors for multiplex imaging in vivo. Nature Methods *17*, 1147–1155.

Petrascheck, M., Ye, X., and Buck, L.B. (2007). An antidepressant that extends lifespan in adult *Caenorhabditis elegans*. Nature *450*, 553–556.

Pirri, J.K., and Alkema, M.J. (2012). The neuroethology of *C. elegans* escape. Current Opinion in Neurobiology *22*, 187–193.

Pirri, J.K., McPherson, A.D., Donnelly, J.L., Francis, M.M., and Alkema, M.J. (2009). A Tyramine-Gated Chloride Channel Coordinates Distinct Motor Programs of a *Caenorhabditis elegans* Escape Response. Neuron *62*.

Piston, D.W., and Kremers, G.J. (2007). Fluorescent protein FRET: the good, the bad and the ugly. Trends in Biochemical Sciences *32*, 407–414.

Rasmussen, S.G.F., DeVree, B.T., Zou, Y., Kruse, A.C., Chung, K.Y., Kobilka, T.S., Thian, F.S., Chae, P.S., Pardon, E., Calinski, D., *et al*. (2011). Crystal structure of the β2 adrenergic receptor–Gs protein complex. Nature *477*.

Ravotto, L., Duffet, L., Zhou, X., Weber, B., and Patriarchi, T. (2020). A Bright and Colorful Future for G-Protein Coupled Receptor Sensors. Frontiers in Cellular Neuroscience *14*.

Rengarajan, S., Yankura, K.A., Guillermin, M.L., Fung, W., and Hallem, E.A. (2019). Feeding state sculpts a circuit for sensory valence in *Caenorhabditis elegans*. Proceedings of the National Academy of Sciences of the United States of America *116*, 1776–1781.

Ressler, K.J. and Nemeroff, C.B. (2000). Role of serotonergic and noradrenergic systems in the pathophysiology of depression and anxiety disorders. Depress. Anxiety, 12: 2-19.

Rex, E., and Komuniecki, R.W. (2002). Characterization of a tyramine receptor from *Caenorhabditis elegans*. Journal of Neurochemistry *82*.

Rex, E., Molitor, S.C., Hapiak, V., Xiao, H., Henderson, M., and Komuniecki, R. (2004). Tyramine receptor (SER-2) isoforms are involved in the regulation of pharyngeal pumping and foraging behavior in *Caenorhabditis elegans*. Journal of Neurochemistry *91*, 1104–1115.

Rex, E., Hapiak, V., Hobson, R., Smith, K., Xiao, H., and Komuniecki, R. (2005). TYRA-2 (F01E11.5): A *Caenorhabditis elegans* tyramine receptor expressed in the MC and NSM pharyngeal neurons. Journal of Neurochemistry *94*, 181–191.

Roeder, T. (2016). Chapter 1 - Trace Amines: An Overview. In Trace Amines and Neurological Disorders, T. Farooqui, and A.A. Farooqui, eds. (San Diego: Academic Press), pp. 3–9

Roeder, T. (2020). The control of metabolic traits by octopamine and tyramine in invertebrates. Journal of Experimental Biology *223*.

Romoser, V.A., Hinkle, P.M., and Persechini, A. (1997). Detection in Living Cells of $Ca^{2+}$-dependent Changes in the Fluorescence Emission of an Indicator Composed of Two Green Fluorescent Protein Variants Linked by a Calmodulin-binding Sequence. Journal of Biological Chemistry *272*.

Ruhé, H.G., Mason, N.S., and Schene, A.H. (2007). Mood is indirectly related to serotonin, norepinephrine and dopamine levels in humans: A meta-analysis of monoamine depletion studies. Molecular Psychiatry *12*, 331–359.

Sawin, E.R., Ranganathan, R., and Horvitz, H.R. (2000). *C. elegans* Locomotory Rate Is Modulated by the Environment through a Dopaminergic Pathway and by Experience through a Serotonergic Pathway. Neuron *26*.

Schroeder, K.S., and Neagle, B.D. (1996). FLIPR: A New Instrument for Accurate, High Throughput Optical Screening. Journal of Biomolecular Screening *1*.

Sellegounder, D., Yuan, C.H., Wibisono, P., Liu, Y., and Sun, J. (2018). Octopaminergic signaling mediates neural regulation of innate immunity in *Caenorhabditis elegans*. MBio *9*.

Shimada, I., Ueda, T., Kofuku, Y., Eddy, M.T., and Wüthrich, K. (2019). GPCR drug discovery: integrating solution NMR data with crystal and cryo-EM structures. Nature Reviews Drug Discovery *18*.

Sotnikova, T.D., and Gainetdinov, R.R. (2009). Octopamine and Other Monoamines in Invertebrates. In Encyclopedia of Neuroscience, L.R. Squire, ed. (Oxford: Academic Press), pp. 9–15.

Specht, E.A., Braselmann, E., and Palmer, A.E. (2017). A Critical and Comparative Review of Fluorescent Tools for Live-Cell Imaging. Annual Review of Physiology *79*.

Spielman, S.J., Kumar, K., and Wilke, C.O. (2015). Comprehensive, structurally-informed alignment and phylogeny of vertebrate biogenic amine receptors. PeerJ *3*.

Srinivasan, S., Sadegh, L., Elle, I.C., Christensen, A.G.L., Faergeman, N.J., and Ashrafi, K. (2008). Serotonin Regulates *C. elegans* Fat and Feeding through Independent Molecular Mechanisms. Cell Metabolism *7*.

Srinivasan, V., Pandi-Perumal, S.R., Trahkt, I., Spence, D.W., Poeggeler, B., Hardeland, R., and Cardinali, D.P. (2009). Melatonin and melatonergic drugs on sleep: Possible mechanisms of action. International Journal of Neuroscience *119*, 821–846.

Stiernagle, T. (2006). Maintenance of *C. elegans.* WormBook : The Online Review of *C. elegans* Biology 1-11.

Sullivan E., Tucker E.M., Dale I.L. (1999) Measurement of [Ca2+] Using the Fluorometric Imaging Plate Reader (FLIPR). In: Lambert D.G. (eds) Calcium Signaling Protocols. Methods in Molecular Biology™, vol 114. Humana Press.

Sun, F., Zeng, J., Jing, M., Zhou, J., Feng, J., Owen, S.F., Luo, Y., Li, F., Wang, H., Yamaguchi, T., *et al*. (2018). A Genetically Encoded Fluorescent Sensor Enables

Rapid and Specific Detection of Dopamine in Flies, Fish, and Mice. Cell *174*, 481-496.e19.

Sun, F., Zhou, J., Dai, B., Qian, T., Zeng, J., Li, X., Zhuo, Y., Zhang, Y., Wang, Y., Qian, C., *et al*. (2020). Next-generation GRAB sensors for monitoring dopaminergic activity *in vivo*. Nature Methods *17*.

Sun, J., Singh, V., Kajino-Sakamoto, R., and Aballay, A. (2011). Neuronal GPCR Controls Innate Immunity by Regulating Noncanonical Unfolded Protein Response Genes. Science *332*.

Sun, J., Liu, Y., and Aballay, A. (2012). Organismal regulation of XBP-1-mediated unfolded protein response during development and immune activation. EMBO Reports *13*.

Takano, H. (2018). Cognitive function and monoamine neurotransmission in schizophrenia: Evidence from positron emission tomography studies. Frontiers in Psychiatry *9*.

Thomas, P., and Smart, T.G. (2005). HEK293 cell line: A vehicle for the expression of recombinant proteins. Journal of Pharmacological and Toxicological Methods *51*.

Torrealba, F., and Carrasco, M.A. (2004). A review on electron microscopy and neurotransmitter systems. Brain Research Reviews *47*.

Torres, G.E., Gainetdinov, R.R., and Caron, M.G. (2003). Plasma membrane monoamine transporters: Structure, regulation and function. Nature Reviews Neuroscience *4*, 13–25.

Vedvik, K.L., Doucette, C.J., Koepnick, E.J., Beck, M.T., Honer, J.R., Turek-Etienne, T.C., and Hanson, B.J. SelectScreen™ Cell-based GPCR Profiling Service: Rapid Profiling of Compounds with Functional Assays in Agonist and Antagonist Mode. (Invitrogen Discovery Sciences).

Virkki, L. v., Franke, C., Somieski, P., and Boron, W.F. (2002). Cloning and Functional Characterization of a Novel Aquaporin from *Xenopus laevis* Oocytes. Journal of Biological Chemistry *277*.

Wan, J., Peng, W., Li, X., Qian, T., Song, K., Zeng, J., Deng, F., Hao, S., Feng, J., Zhang, P., *et al*. (2021). A genetically encoded sensor for measuring serotonin dynamics. Nature Neuroscience *24*.

Wang, T., Yang, N., Liang, C., Xu, H., An, Y., Xiao, S., Zheng, M., Liu, L., Wang, G., and Nie, L. (2020). Detecting Protein-Protein Interaction Based on Protein Fragment Complementation Assay. Current Protein & Peptide Science *21*.

Watanabe, Y., Tsujimura, A., Aoki, M., Taguchi, K., and Tanaka, M. (2016). Development of the 5-HT2CR-Tango System Combined with an EGFP Reporter Gene. Journal of Molecular Neuroscience *58*.

Weis, W.I., and Kobilka, B.K. (2018). The Molecular Basis of G Protein–Coupled Receptor Activation. Annual Review of Biochemistry *87*, 897–919.

Whitaker, M. (2010). Genetically encoded probes for measurement of intracellular calcium. Methods in Cell Biology *99*, 153–182.

White, J.G., Southgate, E., Thomson, J.N., and Brenner, S. (1986). The structure of the nervous system of the nematode *Caenorhabditis elegans*. Philosophical Transactions of the Royal Society of London. B, Biological Sciences *314*.

Witvliet, D., Mulcahy, B., Mitchell, J.K., Meirovitch, Y., Berger, D.R., Wu, Y., Liu, Y., Koh, W.X., Parvathala, R., Holmyard, D., et al. (2021). Connectomes across development reveal principles of brain maturation. BioRxiv 2020.04.30.066209.

Wragg, R.T., Hapiak, V., Miller, S.B., Harris, G.P., Gray, J., Komuniecki, P.R., and Komuniecki, R.W. (2007). Tyramine and Octopamine Independently Inhibit Serotonin-Stimulated Aversive Behaviors in *Caenorhabditis elegans* through Two Novel Amine Receptors. Journal of Neuroscience *27*.

Yamamoto, K., and Vernier, P. (2011). The Evolution of Dopamine Systems in Chordates. Frontiers in Neuroanatomy *5*.

Yamamoto, K., Mirabeau, O., Bureau, C., Blin, M., Michon-Coudouel, S., Demarque, M., and Vernier, P. (2013). Evolution of Dopamine Receptor Genes of the D1 Class in Vertebrates. Molecular Biology and Evolution *30*.

Youdim, M.B.H., Edmondson, D., and Tipton, K.F. (2006). The therapeutic potential of monoamine oxidase inhibitors. Nature Reviews Neuroscience *7*, 295–309.

Zeng, J., Sun, F., Wan, J., Feng, J., and Li, Y. (2019). New optical methods for detecting monoamine neuromodulators. Current Opinion in Biomedical Engineering *12*.

**Department of Biology**
Naamsestraat 59
3000 LEUVEN, BELGIUM
tel. +32 16 37 73 98
www.kuleuven.be